Numéro d'ordre : 067 Année 2007

Université de Technologie de Belfort-Montbéliard - Université de Besançon
Université Technique de Cluj-Napoca (Roumanie)

Ecole Doctorale Sciences pour l'Ingénieur et Microtechniques

THESE EN CO-TUTELLE

Présentée pour obtenir le grade de

DOCTEUR DE L'UNIVERSITE DE TECHNOLOGIE DE BELFORT-MONTBELIARD ET DE L'UNIVERSITE DE BESANÇON

Spécialité: **SCIENCES POUR L'INGENIEUR**

Analyse et contrôle du couple des moteurs synchrones à aimants permanents pour la propulsion des véhicules électriques

Par

Adina Mariana MUNTEAN

Soutenue le 12 Juillet 2007 devant le jury composé de **:**

Président

Radu CIUPA	Professeur à l'Université Technique de Cluj-Napoca, Roumanie

Rapporteurs :

Ion BOLDEA	Professeur à l'Université Polithenica deTimisoara, Roumanie
Mohamed GABSI	Professeur à l'Ecole Nationale Supérieure de Cachan

Examinateurs :

Abdellatif MIRAOUI	Professeur à l'Université de Technologie de Belfort-Montbéliard, Directeur de thèse
Mircea M. RADULESCU	Professeur à l'Université Technique de Cluj-Napoca, Roumanie, Directeur de thèse
Radu MUNTEANU	Professeur à l'Université Technique de Cluj-Napoca, Roumanie

To my family,

Résumé

L'intérêt croissant pour la conservation de l'énergie et la protection de l'environnement a accéléré le développement récent de la technologie des véhicules électriques. Le système de propulsion, qui constitue la composante majeure d'un véhicule électrique, joue le rôle d'interface électromécanique entre la source d'énergie embarquée et les roues motrices. Du point de vue fonctionnel, il réside en deux parties: électrique et mécanique, la première comportant le moteur électrique, son alimentation électronique de puissance et sa commande.

En compétition avec les moteurs asynchrones et réluctants autocommutés, les moteurs synchrones à aimants permanents et à alimentation par onduleurs de tension offrent pour la propulsion des véhicules électriques, les avantages d'un rapport couple/ poids, d'une puissance volumique et d'un rendement supérieures.

Le travail présenté dans les six chapitres structurant cette thèse de doctorat s'insère dans la problématique actuelle des actionneurs pour véhicules électriques, ayant pour objectif l'analyse et le contrôle du couple développé par un moteur synchrone avec excitation par aimants permanents enterrés dans le rotor et enroulement induit triphasé au stator à alimentation par onduleur de tension, en vue des applications de propulsion des véhicules électriques.

Le premier chapitre décrit les caractéristiques essentielles d'un système de propulsion des véhicules électriques. Après l'argumentation détaillée des avantages des moteurs synchrones à aimants permanents dans une telle application, les topologies appropriées du rotor et stator de ces moteurs pour la propulsion des véhicules électriques sont examinées de près.

La modélisation dynamique non linéaire du moteur synchrone à aimants permanents enterrés, en modes d'opération à couple constant jusqu'à la vitesse de base et à puissance constante avec défluxage à hautes vitesses, est développée dans le deuxième chapitre. On présente d'abord le modèle de circuit à variables de phase considérant la saturation magnétique. Ensuite, des modèles non linéaires *dq* diphasés équivalents, concernant les modes d'opération à couple constant (avec rapport couple/courant induit maximal) et à puissance constante (avec défluxage à maximisation du couple disponible), sont développés en considérant la saturation et les pertes en fer.

Dans le troisième chapitre, une analyse numérique du champ magnétique et des composants - mutuel, réluctant, de détente et pulsatoire - du couple caractérisant un moteur synchrone à aimants permanents enterrés est présentée. Une ample étude électromagnétique comparative, par simulation à l'aide de la méthode des éléments finis du logiciel FLUX 2D, est effectuée sur les moteurs synchrones à aimants permanents enterrés en mono- et double-couche.

Le quatrième chapitre s'occupe des stratégies de contrôle du couple pour les moteurs synchrones à aimants permanents enterrés. Les contrôles indirect et direct (DTFC) du couple en modes d'opération à couple constant et à puissance constante sont présentés.

Les problèmes issus de l'implémentation du contrôle direct du couple (DTFC) pour les moteurs synchrones à aimants permanents enterrés sont identifiés et leurs solutions possibles sont envisagées.
Un schéma de contrôle DTFC pour moteurs synchrones à aimants permanents enterrés en modes d'opération à couple constant (avec rapport couple/courant induit maximal) jusqu'à la vitesse de base et à puissance constante (avec défluxage à maximisation du couple disponible) à hautes vitesses est proposé et validé par des résultats de simulation dynamique.

Dans le cinquième chapitre, le banc d'essais réalisé et les résultats expérimentaux correspondants sont présentés. Les réponses dynamiques en couple des moteurs synchrones à aimants permanents enterrés, sous contrôle direct (DTFC) et indirect du couple en vue des applications de propulsion des véhicules électriques, sont précisément et comparativement analysées.

Le dernier chapitre résume les contributions originales de l'auteur de cette thèse et suggère les perspectives de développement des recherches dans le même domaine.

Abstract

Electric traction is one of the most promising technologies that can lead to significant improvements in vehicle performance, energy utilization efficiency and reduction of polluting emissions. The propulsion system is the major part of electric vehicles, which role is to interface the on-board electric source with vehicle wheels, transferring energy in either direction as required. From the functional point of view, the electric vehicle propulsion system can be divided into two parts: electrical and mechanical, first comprises the electric motor, the power electronic converter and the controller.

In competition with induction motors and switched reluctance motors, inverter-fed permanent magnet synchronous motors are ideally suited for electric vehicles propulsion applications, since they have a high ratio torque/weight, low mass and volume and high efficiency.

The research presented in this thesis, structured in six chapters, is in line with the actual problems of electric vehicles. The purpose of the thesis is to analyze and control the torque developed by an inverter-feed three phase permanent magnet synchronous motor for applications of electric vehicle propulsion.

First chapter outlines the main features of an electric-vehicle propulsion system. After proving that the general class of permanent magnet synchronous motors is well suited to such drive applications, appropriate rotor and stator topologies of these motors for electric vehicles propulsion are examined.

The dynamic modeling of the interior permanent magnet synchronous motors operating in constant-torque and constant-power flux-weakening modes is developed in the second chapter. The two-phase equivalent *dq* model, taking into account the magnetic saturation, is presented. Then the nonlinear equivalent *dq* model, for the constant-torque operation mode (with maximum torque-to-armature current ratio) and constant-power operation mode (with maximum-torque flux-weakening) taking into account the iron saturation and losses are developed.

In the third chapter**,** an equivalent magnetic circuit-based analysis and PM alignment (mutual), reluctance, cogging and pulsating torque components of interior permanent magnet synchronous motor are presented. Then a comparative torque analysis using 2D finite-element field simulations of interior permanent magnet synchronous motors single- and double-layer is performed.

The fourth chapter deals with torque control strategies for interior permanent magnet synchronous motors. The indirect and direct torque control (DTFC) in constant torque operation mode and constant power operation mode are presented.
The major problems associated with DTFC schemes for interior permanent magnet synchronous motors and their remedies are discussed.
The hysteresis-based DTFC scheme of interior permanent magnet synchronous motor in constant-torque region bellow the base speed (with maximum torque-to-stator current ratio) and constant-power flux-weakening operation mode (with highest available torque) in the region above base speed is proposed and validated by simulation results.

In chapter five, the experimental study and the corresponding experimental results are presented. The dynamic torque response of interior permanent magnet synchronous motor under DTFC and indirect torque control for applications of electric vehicles propulsion is comparatively analyzed.

In the last chapter, general contributions are drawn by the author of the thesis and some suggestions are given for future work in the same area.

Contents

Chapter 1

INTRODUCTION

1.1. Electric-vehicle propulsion system features

Electric traction is one of the most promising technologies that can lead to significant improvements in vehicle performance, energy utilization efficiency and reduction of polluting emissions.

In the present term acceptation, an *electric vehicle* (EV) designates a battery-powered electrically-propelled road vehicle [1, 2]. With ever increasing concerns on energy conservation and environmental protection throughout the world, the development of EV technology has taken on an accelerated pace. EVs offer high energy efficiency, enable load equalization of power systems, show zero local exhaust emissions, and operate quietly and almost vibration-free.

The *propulsion system* is the major part of EVs, which role is to interface the on-board electric source with vehicle wheels, transferring energy in either direction as required, with high efficiency, under control of the driver. From the functional point of view, the EV propulsion system can be divided into two parts: electrical and mechanical. The electrical part mainly comprises the electric motor, the power electronic converter and the controller. The mechanical part consists of the transmission device (optional) and wheels.

Electric propulsion system (EPS) requirements for EVs with economic power supply can be summarized as follows [1, 2]:

- high power and torque density;
- high torque capability from zero speed up to a base speed, with voltage rising up to its maximum value at base speed and limited to that value at higher speeds;
- constant power capability over a speed range of typically 3:l above base speed, with limited values of voltage and current;
- fast torque response;
- minimum weight, good controllability, and low torque ripple;
- high efficiency, reliability and robustness over a wide range of EV operating conditions;
- reasonable cost.

The selection of an appropriate EPS for EV is a challenging task, which should be carried out at the system level, depending not only on vehicle constraints, but also on driver expectation, defined by a driving profile, which includes the initial acceleration, cruising at vehicle rated and maximum speeds.

To proceed in designing an EPS for EV, it is essential (i) to determine *acceleration, climbing and cruising power requirements* to be imposed upon the motor drive system by the EV, and (ii) to get a large charge range while achieving low drive weight, volume and cost. Hence, the main performance constraints on the EPS for EV are defined by vehicle type and mass, maximum velocity, rated speed for the specified road grade, and acceleration.

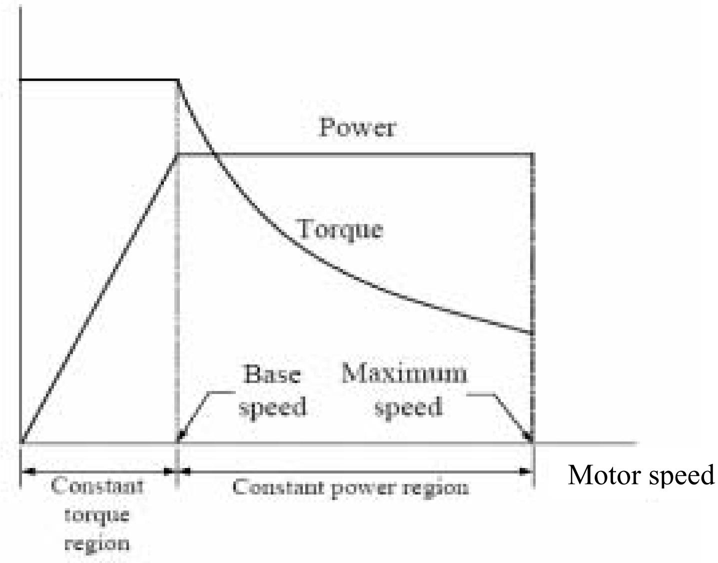

Fig. 1.1. Typical characteristics of an electric motor for the EV propulsion system.

The EV performance is completely determined by the profile of traction effort vs. vehicle speed on the driven wheels. This profile is derived from the characteristics of the on-board energy source and mechanical transmission, i.e. the EPS of EV must be able to deliver maximum torque to achieve gradeability, torque for fastest acceleration and torque at maximum speed, within the volt-ampere constraints of the EPS drive. The electric motor of the EPS for EV yields a torque vs. speed characteristic (Fig.1.1) very close to the ideal traction effort vs. vehicle speed profile. The torque vs. speed characteristic of an electric motor for the EV propulsion system is identified by the *base speed*, below which, the motor provides a high constant-torque operation mode, and above which, it operates at constant power. In a more general way, the motor speed can be identified by a speed ratio, ɔ, which is defined as the ratio of maximum speed of the motor to its base speed. The operation beyond the base speed up to the maximum speed, for which the motor torque decreases hyperbolically with increasing speed, results in a constant (rated) power output. The range of the constant power operation depends primarily on the particular electric motor type and its control strategy.

When running on the road, the EV is pushed forward by the traction force, which balances the rolling, aerodynamic, hill climbing and accelerating resistances. In order to calculate the power required from EPS of the EV during acceleration, the traction power on the EV driven wheel can be expressed as

$$P_t = V\left(M_v g f_r + \frac{1}{2}\rho_a C_D A V^2 + M_v \frac{dV}{dt}\right) \tag{1.1}$$

where V is the vehicle speed, M_v, the vehicle mass, g, the gravity acceleration, f_r, the rolling resistance coefficient, ρ_a, the air mass density, C_D, the aerodynamic resistance coefficient, A, the vehicle front area, and dV/dt, the vehicle acceleration. From Eq.(1.1), the time to accelerate the vehicle from zero speed to the final speed of acceleration period, V_f, results:

$$t_a = \int_0^{V_f} \frac{M_v}{P_t / V - (M_v g f_r + 0.5\,\psi_a C_D A V^2)} dV \quad . \tag{1.2}$$

The profile of EV traction effort and power vs. vehicle speed is illustrated in Fig.1.2, in which, V_b is the vehicle speed corresponding to the base speed of the electric motor of the EV propulsion system. For the acceleration time, t_a, the traction power P_t can be calculated as

$$P_t = \frac{M_v}{2t_a}(V_b^{\,2} + V_f^{\,2}) + \frac{2}{3} M_v g f_r V_f + \frac{1}{5}\,\psi_a C_D A V_f^{\,3} \tag{1.3}$$

Eq.(1.3) points out that the required traction power to reach velocity V_f in time t_a is dependent on the ratio of the constant-torque and constant-power speed ranges of the EV propulsion-system electric motor. Moreover, it was proven in [3] that with a large speed ratio ɔ (i.e. low base speed), the traction power required, for the same acceleration time, decreases. However, when ɔ is larger than 4, the benefit of getting to use a lower power motor becomes less significant.

When identifying the traction power of the EPS for EV, the uphill ability of the vehicle should be also considered. However, it is of common evidence, that the EV traction effort inherently meets the road gradeability requirement, when the designed traction power meets the acceleration performance, as in Eq.(1.3).

The EPS designed to accelerate the vehicle from zero to rated velocity will always have sufficient power to cruise the vehicle at rated speed, provided that the roadway slope specified for initial acceleration has not been raised for rated velocity cruising conditions. Moreover, for the EV designed with fast acceleration characteristic, P_t, derived to meet the initial acceleration requirement, is likely to be greater than the traction power required to cruise the vehicle at maximum speed.

The design rated power of the EPS should embrace the majority of operating points covering the powers derived from driving cycles, the average acceleration, and the average operating grade. The development of EPS for EV was based on the growth of various technologies, i.e. electric motors, power electronic converters and control strategies.

With regard to *EPS motor technology*, brushed DC motors were prominent for EV because their torque–speed characteristics suit the traction requirement well, and their speed controls are simple. However, brushed DC motor drives have a bulky construction, low efficiency, low reliability, and higher need of maintenance, mainly due to the presence of mechanical commutator and brushes. Conversely, brushless motors, like cage induction motors, permanent-magnet synchronous motors and switched reluctance motors have become more attractive for recent EVs, as high reliability and maintenance-free operation are prime considerations for vehicle propulsion.

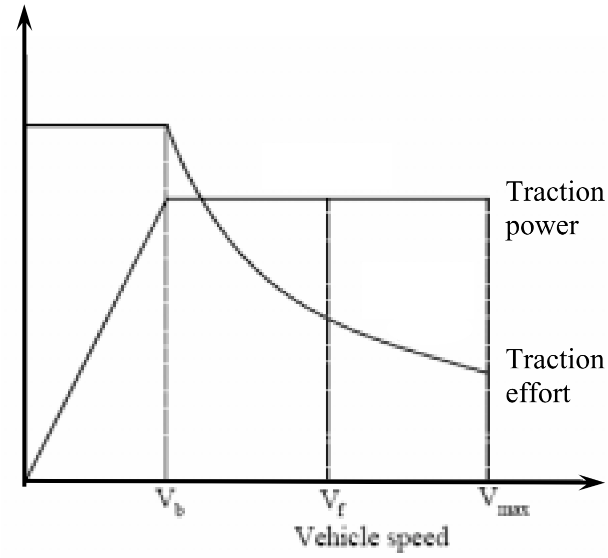

Fig. 1.2. EV traction effort and power vs. vehicle speed.

Cage induction motors (IMs) have been widely accepted for the EPS of EVs, owing to their mature technology, reliable performance, ruggedness, low maintenance and manufacturing costs, as well as ability to operate in hostile environments. However, IM drives are facing a number of drawbacks in EV propulsion applications: high losses, low efficiency (especially, at light-load high-speed range), low power factor and low inverter-usage factor. Moreover, the presence of a breakdown torque limits the IM extended constant-power operation. Any attempt to operate the motor at the maximum current beyond a critical speed, at which the breakdown torque is reached, will stall the motor.

Inverter-fed permanent-magnet synchronous motors (PMSMs) are ideally suited for EV propulsion applications, since they are energy efficient and have a high specific torque and a high peak-to-continuous torque capability. Further, they can operate at constant power over an extended speed range without compromising the VA rating of the drive. Brushless PMSMs emphasize lower mass and volume than other competing motor technologies for a given rating specification, which are essential constraints in EV applications. However, typical PMSMs have a limited constant-power region due to their rather poor field weakening capability.

Switched reluctance motors (SRMs) are now recognized to have considerable potential for EV propulsion. They possess definite advantages, such as simple and rugged construction, fault-tolerant operation, high power density, simple control and outstanding torque–speed characteristics. SRMs can operate with an extended constant-power range due to their inherent low rotor inertia. There are, however, SRM disadvantages, like acoustic noise generation, torque ripple, special converter topology, excessive bus current ripple, electromagnetic interference (EMI) problems, which can be quite critical for EV applications.

The evaluation of EPS motors for EVs is shown in Table 1.1, where a point grading system was adopted. It consists of five major features, and each of them is graded from 1 to 5 points (5 for the best performance).

Table 1.1. Evaluation of EV propulsion motors [3, 4].

	Brushed DC motor	Cage induction motor	Permanent-magnet synchronous motor	Switched reluctance motor
Torque density	2.5	3.5	5	3.5
Efficiency	2.5	3.5	5	3.5
Controllability	5	4	4	3
Reliability	3	5	4	5
Cost	4	5	3.5	4
Total	17	21	21.5	19

Since the torque density is the most important criterion of electric motors for vehicle propulsion systems, the relation between motor torque and its volume can be obtained from the following equation:

$$\frac{T}{V_r} \propto G(k_f k_w pf) \cdot B_{av} \cdot J_s \qquad (1.4)$$

where V_r is the rotor volume in [m^3], B_{av}, the average flux density in [T], J_s, the ampere per meter of airgap circumference, $k_f k_w pf$, the product of form factor, winding factor and internal power factor, respectively, and G, the 'electrical gear ratio' applicable to SRMs. The right hand side of Eq. (1.4) is also referred to as 'torque per unit rotor volume', and depends on motor type and its cooling system. Table 1.2 lists typical torque density values for different EV propulsion brushless motors.

Table 1.2. Typical torque density values for EV propulsion brushless motors [3, 4].

	Cage induction motor	Permanent-magnet synchronous motor	Switched reluctance motor
Torque/ Unit rotor volume [Nm/m^3]	$4 \cdot 10^3$	$3 \cdot 10^4$	$7 \cdot 10^3$
Torque/ Unit copper mass [Nm/kg$_{Cu}$]	6-7	30-50	6

It results from Table 1.1, that the brushless PMSM is the major contender in today's EV electric propulsion. Moreover, Table 1.2 shows that PMSMs enjoy the highest torque density, and, therefore, will have the lowest weight for a specific torque and power rating compared to other type of EV propulsion brushless motors.

1.2. Permanent-magnet synchronous motors for propulsion of electric vehicles

In competition with other brushless motors for EV propulsion, as cage IMs and SRMs, some commonly used arguments in favor of inverter-fed permanent-magnet synchronous motors (PMSM) are:

- higher torque/weight and torque/inertia ratios;

- higher efficiency;
- excellent controllability with minimum torque ripple.

Compared with conventional electrically-excited synchronous motors, the use of rotor magnets for excitation has the following advantages:

- no copper losses in the rotor (and also reduced iron losses);
- low-volume and low-weight design;
- higher efficiency.

However, the PM use has also some drawbacks:

- high cost of the magnets, especially for high-power motors;
- PM demagnetization at high temperature;
- complex and expensive manufacturing process to fix the PMs on the rotor surface or inside the rotor magnetic core;
- additional effort for field-weakening control.

PMSMs have a sinusoidal back-emf and require sinusoidal currents to produce smooth torque. Due to the sine-wave current and airgap flux density requirement of the PMSM, the rotor magnets must be appropriately shaped, and the stator winding must be sinusoidally distributed to reduce the harmonic content.

PMSM is a replica of the wound-rotor synchronous motor, with magnets on the rotor that create the excitation flux, and armature winding in the stator that is energized to create magnetic poles. The rotor is attracted by the energized stator phases, generating a rotation. By using appropriate sequence to supply the stator phases, an armature rotating field on the stator is created and maintained. This action of the rotor chasing after the electromagnet poles on the stator is the fundamental action used in PMSMs. The lead between the rotor and the armature rotating field must be controlled to produce torque. This synchronization is achieved by mounting high-resolution rotor position sensors, like encoders or resolvers, on the rotating shaft. In addition, current sensors are necessary to impose the shape of stator-phase currents.

Once a PMSM is built, the strength and number of PMs in the rotor and the number of poles and turns in the stator-armature coils remain constant; thus, the amount of PM-generated magnetic flux linked by the coils of the stator remains fixed. As a result, the back-emf voltage induced by the PMs increases linearly with the speed of the rotor, thus yielding a rapid reduction in the available voltage (i.e. the difference between the inverter-supply voltage and the back-emf). When there is no longer any voltage available to drive current into the stator, the maximum speed has been reached.

Two distinct reference axes exist in PMSMs, the direct axis (*d*-axis) and the quadrature axis (*q*-axis), which are orthogonal in terms of electric degrees; they correspond to those rotor positions that yield the maximum and minimum amounts of magnetic flux linked by the stator coils, respectively, i.e. the *d*-axis corresponds to the center of a rotor-PM, while the *q*-axis corresponds to the midpoint in the space separating a PM from its closest PM of different polarity. These axes are identified in Fig.1.3 of this section.

By analogy to conventional DC machines, the term ‘flux weakening’ is used to describe a process by which speed rise with falling torque may be obtained above base speed in inverter-fed PMSMs for EV propulsion applications. The technique uses phase advance of stator currents such that a demagnetizing component of armature mmf opposes the rotor PM flux, thus reducing the net effective flux and back-emf. Hence, when i_d is negative, the armature reaction field has a *d*-axis component opposing that of the PM, thereby weakening the flux. The magnitude of the *d*-axis current, needed to completely cancel the PM flux ς_{pm} linked by the stator coils, is referred to as the armature 'characteristic current':

$$i_{ch} = | - i_d | = \varsigma_{pm} / L_d . \tag{1.5}$$

Depending on the position of the magnets on the rotor, PMSMs can be broadly classified into three categories (Fig.1.3): (a) *surface-mounted* (or *projecting*) *PMSMs*, where PMs are glued to the cylindrical rotor outer surface, and magnetized in the radial direction, (b) *inset PMSMs*, where PMs are placed in radial slots or grooves cut at the rotor surface, and (c) *interior* (*internal, buried or embedded*) PMSMs, where PMs are located within the rotor core laminations [5, 6].

Surface-mounted PMSMs provide excellent performance at base speed, but has severe limits in achieving wide-speed range of constant-power operation. Due to the small stator-winding inductance, flux weakening can be obtained only by a great demagnetizing current and a low load. In fact, these PMSMs, operated with an amount i_{ch} of *d*-axis current in the negative direction, would have no speed limit, since the back-emf induced by the PM would be zero. Unfortunately, the inductance L_d is small, hence the magnitude of the 'characteristic current' is large, showing that large armature currents cause only small amounts of flux weakening. Moreover, problems arise from the rotor-PM risks of fly-off due to the centrifugal force at high speeds and of irreversible demagnetization by the armature reaction (even being rather weak), which crosses the magnets. It is then necessary to limit the no-load emf by using a stator winding with small number of turns, and to oversize the current rating of the inverter to deliver the rated torque at low speed and the required torque values in the high-speed range. Since airgap reluctance variation with rotor position is negligible, the stator inductance is independent of rotor position. Thus, motor torque is entirely produced by the interaction between the rotor-PM excitation field and the stator-armature reaction field, i.e. the so-called *PM alignment* or *mutual torque*.
Because rotor magnets should be located on curved surfaces, their shaping causes extra problems and additional manufacturing costs.

The **inset PMSM** is similar to the surface-mounted PMSM, except that the magnets are inserted in the rotor-silicon steel making their surface flush with the rotor periphery, and the magnets are separated by a width of silicon steel. This topology emphasizes rotor saliency, with quadrature (*q*-axis) inductance slightly greater than the direct (*d*-axis) inductance ($L_q > L_d$); however, the available reluctance torque component is rather small.
There is a reduced tendency for armature reaction to demagnetize the rotor magnets at large torque angles compared to the surface-mounted PMSM design. Hence, operation above base speed is more feasible.

Interior PMSMs (IPMSMs) differ from other PMSMs in that they have the PMs buried into punched or cut cavities in the laminated rotor iron. This provides a smooth rotor surface, a robust rotor construction suitable for high speeds (with quiet operation and better dynamic performance) as well as a mechanical support for the magnets, protecting them from physical damage and from demagnetization.
Moreover, in IPMSMs the space occupied by the magnet in the *d*-axis would be occupied by steel in the *q*-axis, resulting in large variation in reluctance around the rotor periphery. Hence, the *q*-axis inductance can be much larger than the *d*-axis inductance. The difference in L_q and L_d leads to the total motor torque of the IPMSM being the sum of the mutual and reluctance

torque components, which is a substantial advantage. IPMSMs thus define *reluctance-assisted PMSMs* of higher torque per unit volume.

Under flux-weakening conditions, IPMSMs are superior to surface-mounted and inset PMSMs, since they provide extended speed range with extra mechanical power output due to their rotor saliency.

It can be easily proven that, for IPMSM constant power, the PM flux ς_{pm} linked by the stator coils diminishes exponentially with the magnetic saliency ratio ($\bullet = L_q / L_d$), and with the *d*-axis stator current to 'characteristic current' ratio (i_d / i_{ch}). Therefore, decreasing the value of i_{ch} and increasing the magnetic saliency are clear goals for improving IPMSM performance.

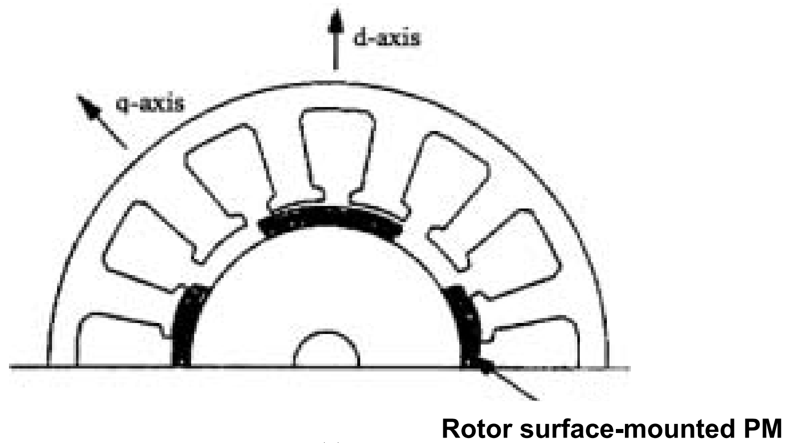

(a)

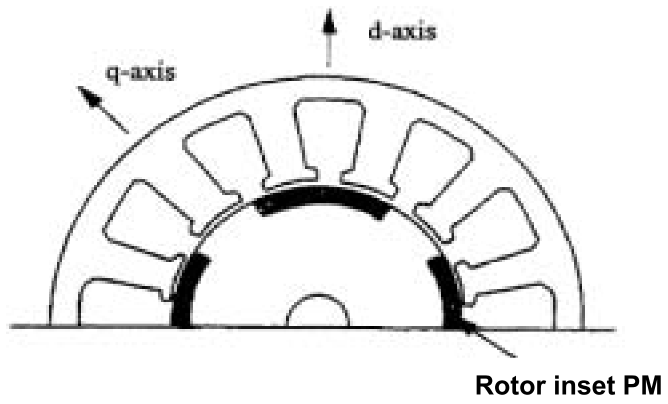

(b)

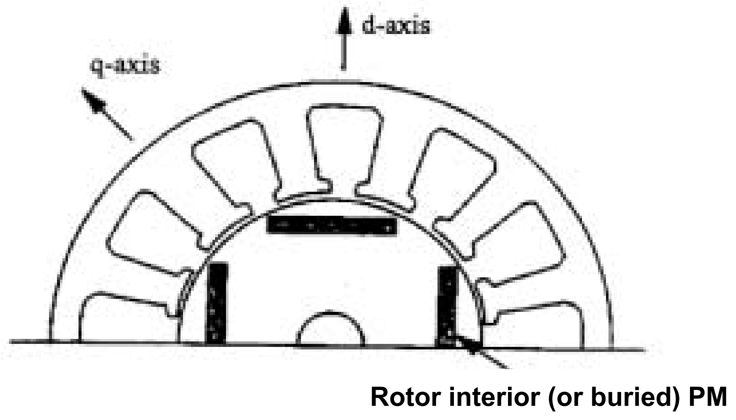

(c)

Fig. 1.3. Half cross-section sketches of surface-mounted (a), inset (b) and interior (c) PMSMs.

Interior permanent-magnet synchronous motors with different rotor and stator topologies

As pointed out in the preceding paragraphs, the rotor design of an IPMSM for EV propulsion has to maximize the magnetic saliency ratio, while matching the reluctance torque it produces with the developed mutual (or PM alignment) torque.

For an inverter-fed IPMSM, the rotor-PM excitation flux being constant, and a rotor winding being not required, there are almost negligible rotor eddy-current and hysteresis losses as well as zero rotor copper losses. Moreover, a PM rotor needs no magnetization from the stator currents, and thus a power factor close to unity can be obtained; a reduction of the inverter rating is also possible without performance loss due to this high power factor.

With the development and cost declining of rare-earth magnet materials, a sufficiently airgap flux density for a high-performance IPMSM can now be achieved; hence, a flux-concentration design of the rotor is no longer needed. Besides, IPMSM's cogging torque is slightly lower than with SMPM design.

The magnets embedded into the PMSM laminated rotor ensure (i) high-speed rotation without vibration or fear of rotor and/or bearing failure, (ii) smaller rotor diameter and lower inertia (by several times compared to a SMPM rotor design), (iii) the arc of the rotor yoke to be optimized, so that the airgap magnetic flux distribution is as sinusoidal as possible, and (iv) a low magnetic saturation due to the armature reaction.

In EV propulsion applications, the torque- and power-speed characteristics of the IPMSM must have the two distinctive regions shown in Fig.1.1. In the first region, the torque remains constant up to the base speed, at which the magnitude of the terminal voltage equals the available inverter voltage, whereas the current is at its limit. In the adjoining second region, the output power remains constant; hence the airgap flux must be weakened so that the terminal voltage may be kept at its rated value. This flux-weakening in an IPMSM can only be accomplished by a negative stator-current component in the *d*-axis, which opposes the PM flux. Due to the current constraint, the developed torque must then be reduced. However, during flux-weakening operation, the reluctance torque component of the IPMSM plays a crucial role by providing useful shaft torque.

It was established [6] that, for achieving wide-speed range of constant power by optimal flux weakening, *the 'characteristic current' has to be equal with the rated stator-armature current of the IPMSM.*

The negative effect of the back-emf constraint on an IPMSM is the inability of its design to satisfy the optimum flux-weakening condition. Actually, to have the back-emf lower than rated voltage of the IPMSM at the maximum speed, requires weak rotor magnets with low remanence and, consequently, low magnet-flux linkage. In such a case, only designs with extremely high saliency ratio can satisfy both the optimum flux weakening condition and the back-emf constraint. Therefore, practical IPMSM designs will have the 'characteristic current' less than the rated stator current, which results in a lower power output in the field-weakening regime than attainable at the base speed.

The most common ***rotor topology*** of commercially-available IPMSMs (Fig.1.4, *a*) has radial lamination with one layer of alternately-magnetized, rectangular-shaped PMs (**single-layer**

IPMSM). Although this simple rotor construction is preferred because it is less expensive and easy to built, *conventional single-layer IPMSMs* have rather small magnetic saliency ratio and flux-weakening range limited to a maximum speed at which the output power ultimately becomes zero.

Via the iron bridges surrounding the PM cavities, part of the flux created by the rotor-PMs escapes as a magnetic leakage flux around PMs, thereby reducing the PM contribution to the overall airgap flux. It has been pointed out [7, 8] that the leakage flux decreases and, consequently, the developed torque increases, when the PMs are shallowly buried in the rotor.

The amount of the rotor leakage flux can also be reduced with interpolar flux barriers (non-magnetic spacers) properly designed along the *q*-axis flux lines. Moreover, since the torque ripple is relatively large, mainly due to the harmonic reluctance torque components, position and width of the flux barriers can be optimized for torque ripple mitigation [8]. However, the *V-shaped single-layer IPMSM* (Fig. 1.4, *b*) has been recently proposed [9] for better ratio between torque ripple and average developed torque. Its main rotor design parameters are the angle (*A*) between the two adjacent PMs of each rotor pole, the PM thickness (*B*) and the distance (*C*) from rotor shaft.

A slightly different rotor design of single-layer IPMSMs suitable for higher flux weakening has been proposed in [9-10]. The rotor-pole PM is segmented, and between two adjacent PM segments there exists a small iron bridge, lying in the path of *d*-axis flux (Fig.1.5).

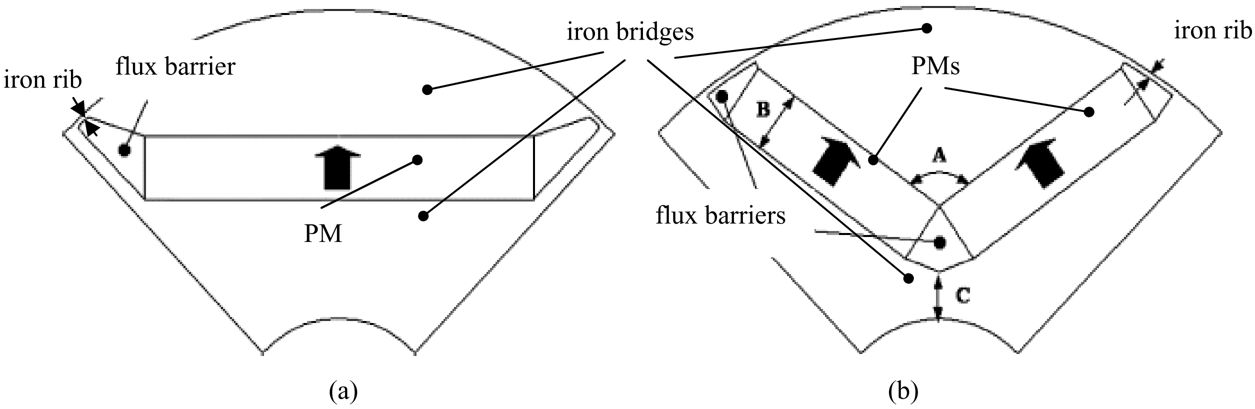

Fig. 1.4. Rotor design sketches for conventional (a) and V-shaped (b) single-layer IPMSMs.

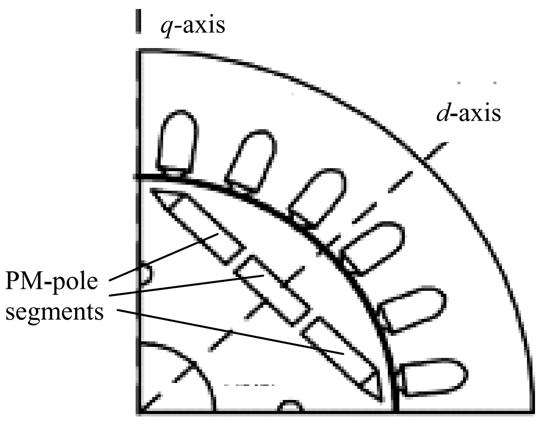

Fig. 1.5. Design sketch for a single-layer segmented IPMSM.

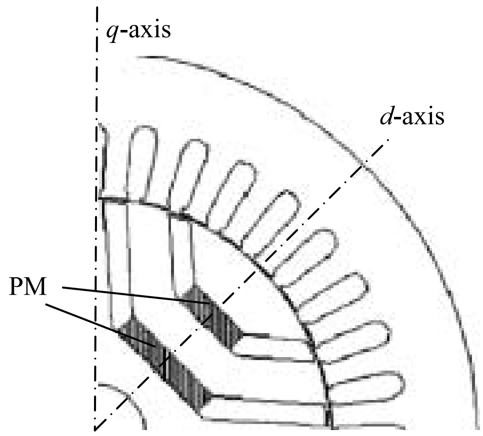

Fig. 1.6. Design sketch for an U-shaped double-layer IPMSM.

In this *single-layer segmented IPMSM* design, the rotor-pole magnet volume is reduced to some extent; besides, the PM flux density is slightly lower due to the extra flux leakage in the iron bridges between PM segments.The negative *d*-axis current performs two tasks: first, it offsets the airgap PM flux by the armature reaction and secondly, it provides additional path to PM flux for canalization in iron bridges between PM segments and thus reducing airgap flux furthermore. Consequently, higher effective flux-weakening in a single-layer segmented IPMSM for same amount of negative *d*-axis current than in a conventional IPMSM. One added advantage of this new single-layer IPMSM is the less danger of permanent demagnetization of the rotor-PMs.

Recent studies [11, 12] have made it clear that to gain high torque generation at a constant current and wide-speed operating range of an IPMSM, it should be constructed so that *q*-axis inductance is high. This can be obtained, for a constant magnet volume, thanks to the **double/multi-layer IPMSM** topology, by splitting up each rotor pole in two or more PM cavity layers with iron separation in the radial direction of the rotor core (Fig. 1.6); hence, multiple flux barriers are introduced increasing the anisotropy in the magnetic path, and thereby enhancing saliency. Comparisons between single- and double/multi-layer IPMSMs have shown that

- the construction of multi-layer IPMSM is far more complex than that of conventional single-layer IPMSMs;
- the *d*-axis stator self-inductance L_d is low and roughly the same for both PM-rotor configurations;
- the *q*-axis stator self-inductance L_q and, correspondingly, the inductance difference L_q - L_d for the double/multi-layer IPM rotor is greater than for the single-layer IPM rotor, mainly due to the additional *q*-axis flux path provided between the rotor-PM layers; however, the *q*-axis inductance was proven not to increase further with more than three PM cavity layers;
- the *q*-axis stator self-inductance L_q for the rotor topology with only one PM per pole decreases greatly with the stator-current increase, because of the magnetic saturation, whereas for the double/multi-layer PM-rotor topology this effect is less significant;
- the stator flux-linkage due to the double/multi-layer of rotor PMs is slightly greater than in the case of single-layer IPM rotor;
- the torque performances using flux-weakening at high speeds for both IPM rotor topologies are quite similar.

The ***stator topology*** of all IPMSMs is similar to that of other AC machines, and comprises (i) the laminated iron core, formed from punched soft magnetic steel stampings, and having as main parts: the teeth, the slots containing the armature winding, and the stator magnetic yoke; (ii) the armature winding, which is usually a three-phase, star-connected, short-pitch, sine-distributed overlapping winding (Fig. 1.7, *a*).

There is a growing interest for IPMSMs with *concentrated stator winding* (Fig.1.7, *b*) in EV propulsion applications, since it enables motor down-sizing and easy winding automation, and has shorter end-windings and smaller copper loss in comparison to a distributed winding. However, recent studies [13, 14] have shown that for identical overall dimensions, airgap length and rotor structure, the IPMSM with concentrated winding is inferior to the IPMSM with distributed winding in terms of the developed torque (i.e. the PM alignment torque is reduced due to lower winding factor and back-emf, and the reluctance torque is reduced mainly because of *d*-axis inductance increase) and of the constant-power region size (caused

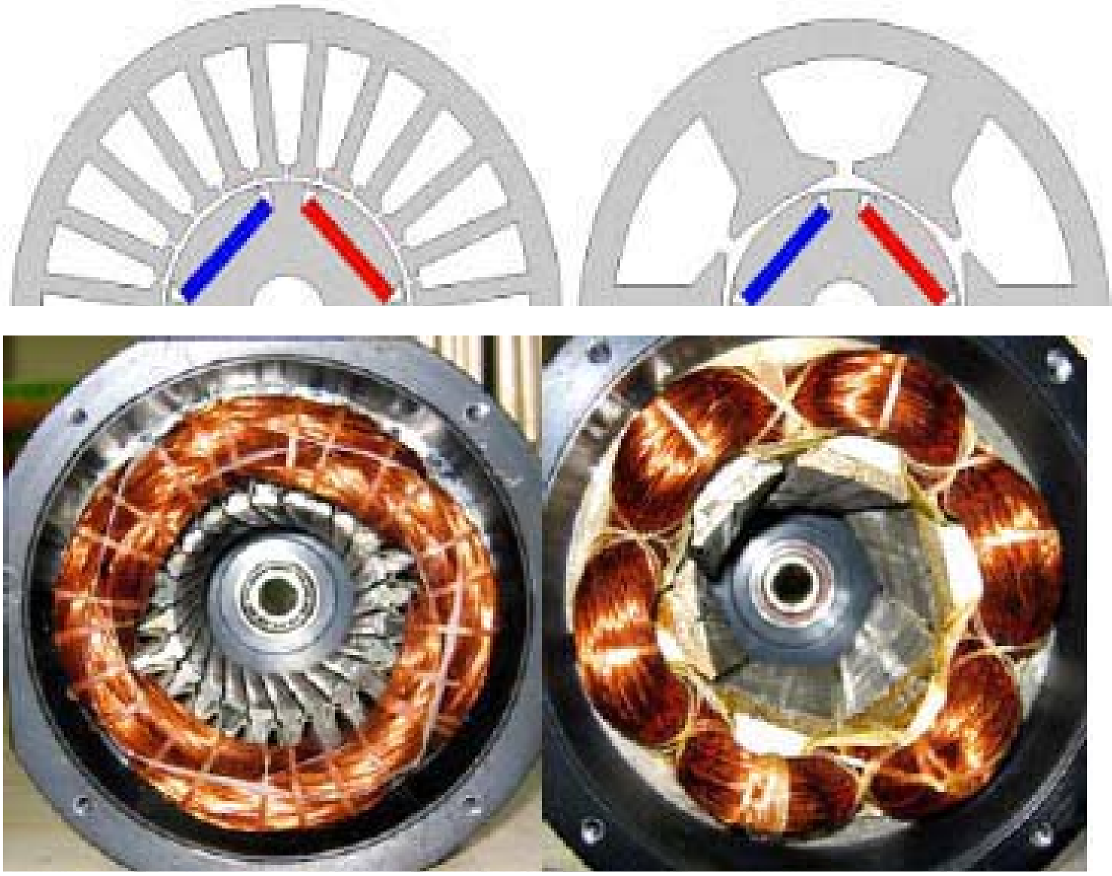

(a) (b)
Fig. 1.7. Half cross-section sketches and built prototypes of IPMSM with distributed (a) and concentrated (b) stator winding [14].

by the distorted sinusoidal waveform and the inability to effectively use reluctance torque; i.e. if maximum developed torque for a concentrated winding is designed to be tantamount to that of a distributed winding, the speed is still not as high as that obtained with a distributed winding even under field weakening control; as a result, the motor will have a narrow constant output region). Moreover, IPMSM with concentrated winding has larger cogging torque and radial stress as well as higher iron losses than IPMSM with distributed winding.

1.3. Outline of the thesis

The aim of this thesis is to analyse and control the developed electromagnetic torque of an IPMSM for EV propulsion applications.
The thesis content is structured on six chapters. A short description of each chapter is given herewith.

Chapter 1 outlines the main features of an electric-vehicle propulsion system. After proving that the general class of PMSMs is well suited to such drive applications, some specific IPMSM subclass designs for EV propulsion are examined.

Chapter 2 develops the mathematical model of IPMSMs suitable for EV propulsion applications. First, a three-phase-variable circuit model of the IPMSM, accounting for parameter variations due to iron saturation, is derived. Then, two-phase equivalent *dq* models for both constant-torque and flux-weakening constant-power operation modes of the IPMSM are developed. These nonlinear dynamic models take into account the iron saturation and losses, respectively, thus being further useful for accurate IPMSM torque analysis and control.

In the first part of **Chapter 3,** an equivalent magnetic circuit-based analysis of a double-layer IPMSM is developed allowing the estimation of the rotor-PM sizes as well as the rated values of PM-rotor and armature-stator fluxes, back-emfs and unsaturated *dq* inductances. Then, a finite-element field analysis of the flux distribution in both single- and double-layer IPMSMs, at no-load and rated-load conditions, is performed, accounting for magnetic saturation in stator and rotor iron parts.
In the second part of the chapter, the electromagnetic torque of both single- and double-layer IPMSMs under rated-load condition is analyzed using 2D finite-element field simulations. Then, pulsating torque components are evaluated, and methods to mitigate them for improving the electromagnetic torque quality are studied.

Chapter 4 deals with electromagnetic torque control strategies for IPMSMs. In the first part of this chapter, the indirect torque control of IPMSM via stator-current regulation in the rotor reference frame is outlined.
The second part of the chapter is dedicated to the direct torque and stator-flux control (DTFC) of IPMSM for EV propulsion. The major problems associated with DTFC schemes for IPMSM and their remedies are first presented.
The hysteresis-based DTFC scheme of IPMSM for EV propulsion is then detailed and an a novel approach for generating the reference stator flux-linkage vector magnitude is proposed to insure IPMSM extended torque-speed envelope with maximum torque-to-stator current ratio operation in the constant-torque region below the base speed as well as constant-power flux-weakening operation with highest available torque in the region above the base speed.
Extensive simulation results to show the effectiveness of the proposed hysteresis-based DTFC scheme of IPMSM over wide-speed operation range are provided.

In the first part of **Chapter 5,** the experimental study on the indirect (via stator-current regulation) torque control of a double-layer IPMSM prototype in the constant-torque operation range is carried out.
The second part of the chapter deals with experiments on IPMSM under DTFC. Similar steady-state and dynamic performances are obtained for both IPMSM torque control strategies in constant-torque operation range.
Experimental results for steady-state characteristics and dynamic torque response of the IPMSM under DTFC in flux-weakening constant-power region above the base speed are also provided and discussed.

In the **last chapter,** general conclusions of the thesis research are drawn, and some suggestions are given for future work in the same area.

Selected references

1. Chan, C.C. and Chau, K.T., *Modern electric vehicle technology*. Oxford University Press, Oxford, UK, 2001, ch. 5.

2. Husain, I., *Electric and hybrid vehicles. Design fundamentals*. CRC Press, Boca Raton, USA, 2003, ch. 9.

3. Brusaglino, G. *et al.*, Advanced drives for electrically-propelled vehicles. *Proc. 1999 IEE Colloq. Electr. Mach. Design Electr. Veh.*, pp. 4/1-4/12.

4. Rahman, Z. *et al.*, An investigation of electric motor drive characteristics for EV and HEV propulsion systems. *SAE Techn. Paper Ser.,* Paper No. 2000-01-3062.

5. Chau, K.T., Chan, C.C. and Wong, Y.S., Advanced power electronic drives for electric vehicles. *Electromotion*, Vol. 5 (1998), No.2, pp. 42-53.

6. Soong, W.L. and Miller, T.J.E., Field-weakening performance of interior permanent-magnet motors. *IEEE Trans. Ind. Applicat.,* Vol. 38 (2002), No. 5, pp. 1251-1258.

7. Matsumoto, N. *et al.*, Torque performance and permanent-magnet arrangement for interior permanent-magnet synchronous motor. *IEEJ Trans. Ind. Applic.* (Japan), Vol. 126 (2006), No. 7, pp. 954-960.

8. Kiyoumarsi, A., Moallem, M. and Fahimi, B., Mitigation of torque ripple in interior permanent-magnet motors by optimal shape design. *IEEE Trans. Magn.,* Vol. 42 (2006), No. 11, pp. 3706-3711.

9. Stumberger, A. *et al.*, Analysis of interior permanent-magnet synchronous motor designed for flux-weakening operation. *IEEE Trans. Magn.,* Vol. 37 (2001), No. 5, pp. 3644-3647.

10. Dutta, Rukmi and Rahman, M.F., Design and analysis of an interior permanent-magnet machine with very wide constant-power operation range. *Proc. IEEE Ind. Electron. Soc. Annu. Conf. – IECON 2006*, pp. 1375-1380.

11. Honda, Y. *et al*, Motor design considerations and test results of an interior permanent-magnet synchronous motor for electric vehicles. *Conf. Rec. IEEE Ind. Applic. Soc. Annu. Meet. 1997*, pp. 75-82.

12. Honda, Y. *et al*, Rotor design optimization of a multi-layer interior permanent-magnet synchronous motor. *IEE Proc. - Electr. Power Applic.,* Vol 145 (1998), No. 2, pp. 119-124.

13. Kim, S.-I. *et al.*, Optimization technique for improving torque performance of concentrated-winding interior PM synchronous motor with wide speed range. *Conf. Rec. IEEE Ind. Applic. Soc. Annu. Meet. 2006*, pp. 1933-1940.

14. Kwon, S.-O. *et al.*, Performance comparison of IPMSM with distributed and concentrated windings. *Conf. Rec. IEEE Ind. Applic. Soc. Annu. Meet. 2006*, pp. 1984-1988.

Chapter 2

DYNAMIC MODELLING OF INTERIOR PERMANENT-MAGNET SYNCHRONOUS MOTORS FOR CONSTANT-TORQUE AND CONSTANT-POWER OPERATION MODES

As argued in the previous chapter, the IPMSM is a strong contender for EV propulsion applications. Accordingly, the PMSM design considered throughout this thesis comprises: a stator with a three-phase sine-distributed armature winding fed from a bridge-type voltage-source inverter, and a rotor with radially-magnetized PMs, buried inside a steel laminated core. The applied voltage, which is balanced by the stator winding resistance drop and the induced voltage in the winding, imposes symmetrical sinusoidal currents in the three-phase stator winding, which yield the rotating armature mmf in the airgap. Stator currents are shaped and regulated using high-resolution rotor-position feedback and current sensors, so that the applied current frequency is always in synchronism with the rotor. In its turn, the PM-excited rotor creates a sinusoidal rotor flux linkage.

As pointed out earlier, the large difference in the *q*- and *d*-axis inductances make the IPMSM suitable for flux-weakening operation, thus enabling a wide constant-power speed range with reduced inverter volt-ampere rating.

2.1. Three-phase-variable dynamic model accounting for iron saturation

The torque analysis and control of the IPMSM require an accurate modelling for its dynamic behaviour, which can be accomplished in the stationary reference frame or in the synchronous reference frame, as shown in Fig. 2.1 with regard to a conceptual cross-sectional view of a three-phase two-pole IPMSM. The *abc* and $\alpha\beta$ reference frames are fixed in the stator, the α-axis being chosen collinear with the *a*-axis. The stator reference *a*-axis is chosen to the direction of maximum mmf, when a positive *a*-phase current is supplied at its maximum level. Reference axes for *b*- and *c*- stator-phases are chosen 120^o and 240^o (electrical angle) ahead of the *a*-axis, respectively. The β-axis lags the α-axis by 90^o of space angle. The *abc* to $\alpha\beta$ reference frame transformation essentially converts the three-phase stationary variables to a set of two-phase stationary variables.

The *dq* reference frame is locked to the rotor. Following the convention of choosing the rotor reference frame, the *d*-axis is aligned with the PM-flux direction, while the *q*-axis lags the *d*-axis by 90^o of space angle. The electrical angle of the rotor *q*-axis with respect to the stator *a*-axis is defined as θ; note that as the IPMSM turns, the *dq* reference frame is rotating at the electrical angular speed, $\omega = d\theta/dt$, of the rotor, while the stator *abc* and $\alpha\beta$ reference axes remain fixed in space and stationary in time.

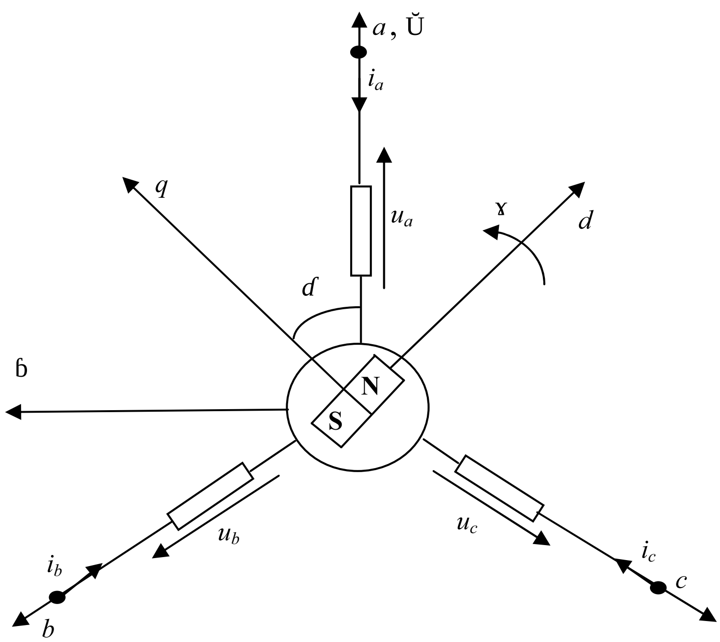

Fig. 2.1. Stationary and synchronous reference frames in IPMSM.

The nonlinear dynamic model of the IPMSM is primarily derived as a three-phase-variable circuit model in which, although magnetic saturation is considered, eddy current and hysteresis effects are disregarded.

The IPMSM stator-phase voltage equation in the stationary frame *abc* and in terms of phase variables can be written as

$$
\begin{aligned}
u_a &= Ri_a + \frac{d\psi_a}{dt} \\
u_b &= Ri_b + \frac{d\psi_b}{dt} \\
u_c &= Ri_c + \frac{d\psi_c}{dt}
\end{aligned}
\tag{2.1}
$$

where u_i, i_i and ψ_i ($i=a, b, c$) represent the instantaneous values of the stator-phase voltage, current and flux-linkage, respectively.

The flux linkage of each stator-phase winding depends on the rotor angular position θ and consists of the contribution of the flux created by the respective stator-phase current and the flux linked by the PM-rotor:

$$
\begin{aligned}
\psi_a(\theta) &= \psi_a^i(\theta) + \psi_a^m(\theta) \\
\psi_b(\theta) &= \psi_b^i(\theta) + \psi_b^m(\theta) \\
\psi_c(\theta) &= \psi_c^i(\theta) + \psi_c^m(\theta)
\end{aligned}
\tag{2.2}
$$

where

$$\psi_a^m(\theta) = \hat{\psi}_{PM}\sin(\theta)$$
$$\psi_b^m(\theta) = \hat{\psi}_{PM}\sin(\theta - \frac{2\pi}{3}) \qquad (2.3)$$
$$\psi_c^m(\theta) = \hat{\psi}_{PM}\sin(\theta + \frac{2\pi}{3})$$

with $\hat{\psi}_{PM}$, the amplitude of the flux-linkage established by the PM-rotor, as viewed from each stator-phase winding, and

$$\psi_a^i(\theta) = L_{aa}(\theta)i_a + L_{ab}(\theta)i_b + L_{ac}(\theta)i_c$$
$$\psi_b^i(\theta) = L_{ba}(\theta)i_a + L_{bb}(\theta)i_b + L_{bc}(\theta)i_c \qquad (2.4)$$
$$\psi_c^i(\theta) = L_{ca}(\theta)i_a + L_{cb}(\theta)i_b + L_{cc}(\theta)i_c$$

Using matrix notation, the stator-phase voltage equation of the IPMSM model can be rewritten as

$$u_{abc} = R_{abc}i_{abc} + \frac{d}{dt}\psi_{abc}^i(\theta) + \frac{d}{dt}\psi_{abc}^m(\theta) \qquad (2.5)$$

where

$$u_{abc} = \begin{bmatrix} u_a & u_b & u_c \end{bmatrix}^T \qquad (2.6)$$

$$i_{abc} = \begin{bmatrix} i_a & i_b & i_c \end{bmatrix}^T \qquad (2.7)$$

$$\psi_{abc}^i(\theta) = \begin{bmatrix} \psi_a^i(\theta) & \psi_b^i(\theta) & \psi_c^i(\theta) \end{bmatrix}^T \qquad (2.8)$$

$$\psi_{abc}^m(\theta) = \begin{bmatrix} \psi_a^m(\theta) & \psi_b^m(\theta) & \psi_c^m(\theta) \end{bmatrix}^T \qquad (2.9)$$

$$R_{abc} = \begin{bmatrix} R & 0 & 0 \\ 0 & R & 0 \\ 0 & 0 & R \end{bmatrix} \qquad (2.10)$$

By developing the expression of the stator winding flux-linkage contributed by the stator-phase currents one obtains:

$$\frac{d\psi^{i}_{abc}(\theta)}{dt} = L_{abc}(\theta)\frac{di_{abc}}{dt} + \omega\frac{dL_{abc}(\theta)}{d\theta}i_{abc} \tag{2.11}$$

with

$$L_{abc}(\theta) = \begin{bmatrix} L_{aa}(\theta) & L_{ab}(\theta) & L_{ac}(\theta) \\ L_{ba}(\theta) & L_{bb}(\theta) & L_{bc}(\theta) \\ L_{ca}(\theta) & L_{cb}(\theta) & L_{cc}(\theta) \end{bmatrix} \tag{2.12}$$

Hence, the matrix-form Eq. (2-5) becomes

$$u_{abc} = R_{abc}i_{abc} + L_{abc}(\theta)\frac{di_{abc}}{dt} + \omega\frac{dL_{abc}(\theta)}{d\theta}i_{abc} + \frac{d\psi^{m}_{abc}(\theta)}{dt}. \tag{2.13}$$

It is to be noted that in the inductance matrix given by Eq.(2.12), each stator-phase self inductance is maximum when the rotor *q*-axis is aligned with the respective phase, while mutual inductance is maximum when the rotor *q*-axis is in the midway between the two concerned stator-phases. Due to the iron saturation, the three-phase winding inductance is a function of both current and rotor position. However, IPMSM phase-winding magnetic fluxes are dominated by the rotor-PM linkages, so that the inductance $L_{abc}(\theta)$ has been considered as rotor position dependent only in Eqs.(2.12) and (2.13).

The developed electromagnetic torque may be calculated from the IPMSM co-energy derivative with respect to rotor position, thus yielding

$$T_e = p\cdot\left[\frac{1}{2}i^{T}_{abc}\frac{dL_{abc}(\theta)}{d\theta}i_{abc} + i^{T}_{abc}\frac{d\psi^{m}_{abc}(\theta)}{d\theta}\right] \tag{2.14}$$

where the first term represents the reluctance torque and the second term is the PM-alignment (or mutual) torque.

The motion equation considering the dynamics of the IPMSM drive has to be added

$$\frac{J}{p}\frac{d\omega}{dt} = T_e + T_{cog}(\theta) - T_{fr} - T_l, \tag{2.15}$$

where J represents the total inertia of motor and load reduced to rotor shaft, $T_{cog}(\theta)$ defines the cogging torque (i.e. a zero-current torque component proceeding from the rotor-PM airgap flux density variation due to stator slot openings, and having null average value per revolution) and T_{fr}, T_l are the total friction and load torque, respectively.

The *three-phase-variable dynamic model* (2.13)–(2.15) *of the IPMSM* - in which $L_{abc}(\theta)$, $\psi^{m}_{abc}(\theta)$ and $T_{cog}(\theta)$ profiles incorporating also the magnetic saturation effects can be obtained from a nonlinear finite-element field analysis of the motor, and stored in three lookup-tables - is suitable for IPMSM drive simulation.

2.2. Equivalent two-phase dynamic models accounting for iron saturation and losses

In this section, equivalent two-phase dynamic models of the three-phase IPMSM are derived, and the transformation and relation between three-phase quantities and their equivalent two-phase ones are clarified. Although such dynamic models are quite classical, discussions on obtaining parameters of the two-phase equivalent circuit for a given IPMSM are rarely found; hence, establishing a method to obtain two-phase circuit parameters from physically measured data looks of topical interest.

The three-phase stator coordinates *abc* can be transformed into the orthogonal two-phase stationary coordinates $\alpha\beta$ fixed to the stator by using the non-unitary transformation of a generic variable f (representing voltage, current or flux-linkage):

$$\begin{pmatrix} f_\alpha \\ f_\beta \end{pmatrix} = \frac{2}{3}\begin{pmatrix} 1 & \cos\left(\frac{2\pi}{3}\right) & \cos\left(\frac{2\pi}{3}\right) \\ 0 & -\sin\left(\frac{2\pi}{3}\right) & -\sin\left(\frac{2\pi}{3}\right) \end{pmatrix}\begin{pmatrix} f_a \\ f_b \\ f_c \end{pmatrix}, \tag{2.16}$$

where the zero-sequence component f_0 , under the condition of balanced three-phase variables (i.e. the three-phase armature winding star-connected without a neutral connection) is always null, and has been omitted. Eq.(2.16) allows expressing the generic variable f (representing voltage, current or flux-linkage, defined in the $\alpha\beta$ stationary reference frame) in the complex-vector (or space-phasor) form as

$$\underline{f}_{\alpha\beta} = f_\alpha + jf_\beta = \frac{2}{3}(f_a + af_b + a^2 f_c), \quad a = e^{j2\pi/3}. \tag{2.17}$$

By applying the transformation (2.16) and the definition (2.17), the IPMSM dynamic model (2.13)–(2.14) can be transformed from the *abc* stationary reference frame into the $\alpha\beta$ stationary frame, leading to the *complex-vector form of the IPMSM dynamic model in $\alpha\beta$ stator coordinates*:

$$\underline{u}_{\alpha\beta} = R\underline{i}_{\alpha\beta} + \frac{d\underline{\psi}_{\alpha\beta}(\theta)}{dt} = R\underline{i}_{\alpha\beta} + \frac{d(L_{\alpha\beta}(\theta)\underline{i}_{\alpha\beta})}{dt} + j\omega\psi^{m}_{\alpha\beta}(\theta)e^{j\theta} \tag{2.18}$$

$$T_e = \frac{3}{2}p(\psi_\alpha(\theta)i_\beta - \psi_\beta(\theta)i_\alpha). \tag{2.19}$$

A second non-unitary transformation of the generic variable f (representing voltage, current or flux-linkage) simply converts from stationary $\alpha\beta$ frame to the rotating *dq* reference frame locked to the rotor:

$$\begin{pmatrix} f_d \\ f_q \end{pmatrix} = \begin{pmatrix} \cos\theta & \sin\theta \\ -\sin\theta & \cos\theta \end{pmatrix}\begin{pmatrix} f_\alpha \\ f_\beta \end{pmatrix}, \tag{2.20}$$

leading to the *complex-vector form of the IPMSM dynamic model in dq rotor coordinates*:

$$\underline{u}_{dq} = R\underline{i}_{dq} + \frac{d\underline{\psi}_{dq}}{dt} = R\underline{i}_{dq} + \frac{d(L_{dq}\underline{i}_{dq})}{dt} + j\omega(L_{dq}\underline{i}_{dq} + \psi_{PM}) \tag{2.21}$$

$$T_e = \frac{3}{2}p(\psi_d i_q - \psi_q i_d). \tag{2.22}$$

It is to be noticed that since the transformations of Eqs.(2.16) and (2.20) are non- unitary, the power and torque of the two-phase equivalent systems $\alpha\beta$ and *dq* are different from those of the original three-phase system. Therefore, in order to calculate the power and torque from the two-phase equivalent IPMSM models, (3/2) factor has to be included in Eqs.(2.19) and (2.22), respectively. The reason that the non-unitary transformations of Eqs.(2.16) and (2.20) and, accordingly, the non-power-invariant defining form (2.17) of space-phasors, are commonly used is because the magnitude of voltages, currents and flux-linkages are the same in both three-phase and equivalent two-phase frames.

By separating the real and imaginary parts from the above voltage equation (2.21), one obtains:

$$\begin{aligned} u_d &= Ri_d + \frac{d\psi_d}{dt} - \omega\psi_q \\ u_q &= Ri_q + \frac{d\psi_q}{dt} + \omega\psi_d. \end{aligned} \tag{2.23}$$

As the two-step transformation of Eqs.(2.16) and (2.20) is merely mathematic, the *dq* equivalent circuit model (2.22)-(2.23) also holds for a saturated IPMSM. In such case, integration of Eq.(2.23) requires that the *dq* currents are updated at each time-step from the new *dq* flux-linkages, using the magnetization curves in *d*- and *q*-axes. For properly designed IPMSMs, saturation of *d*-axis path, magnetic cross-coupling between the *d*- and *q*-axes, as well as any variation with rotor position can be assumed negligible in Eq.(2.23), thus leading to a *simplified nonlinear dq model of saturated IPMSMs* through the magnetization curves

$$\begin{aligned} \psi_d &= L_d i_d + \psi_{PM} \\ \psi_q &= L_q(i_q) \cdot i_q. \end{aligned} \tag{2.24}$$

where

$$\begin{aligned} \frac{d\psi_d}{dt} &= \left(L_d + \frac{\partial L_d}{\partial i_d} i_d\right)\frac{di_d}{dt} = L_{dt}(i_d)\frac{di_d}{dt}, \quad L_{dt} = \frac{d\psi_d}{di_d} \\ \frac{d\psi_q}{dt} &= \left(L_q + \frac{\partial L_q}{\partial i_q} i_q\right)\frac{di_q}{dt} = L_{dt}(i_q)\frac{di_q}{dt}, \quad L_{qt} = \frac{d\psi_q}{di_q} \end{aligned} \tag{2.25}$$

In the above equations, L_{dt} and L_{qt} represent the transitory saturated inductance of *d*-, respectively *q*-axis.

In Eq.(2.24), the rotor-PM flux linkage ψ_{PM} is supposed constant for all values of d- and q-axis stator current, so that ψ_d (i_d) merely represents a straight-line, while the nonlinear function $L_q(i_q)$ has numerical expression, best obtained from finite-element field analysis of the IPMSM.

The two-phase equivalent circuits corresponding to the saturated IPMSM dynamic model (2.23)-(2.24) in dq rotor coordinates are shown in Fig. 2.2.

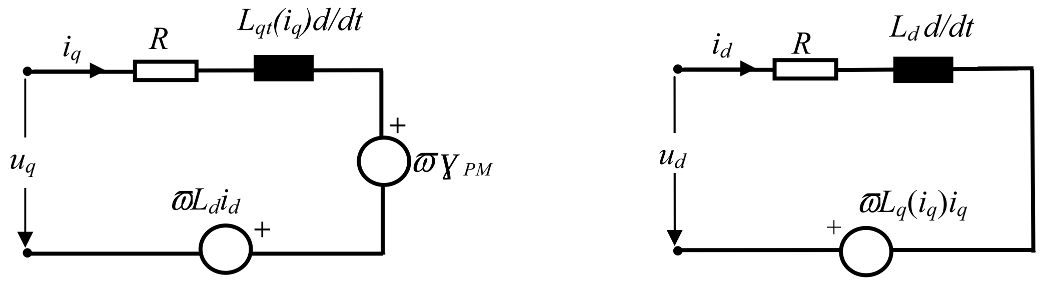

q-axis equivalent circuit $\qquad$ d-axis equivalent circuit

Fig. 2.2 Equivalent circuits of the saturated IPMSM dynamic model in dq rotor coordinates.

The above equations (2.23)-(2.24) allow expressing the developed electromagnetic torque of Eq.(2.22) as

$$T_e = \frac{3}{2}p\left[\psi_{PM} i_q + (L_d - L_q(i_q))i_d i_q\right] \tag{2.26}$$

The first term of Eq.(2.26) corresponds to the PM-alignment (or mutual) torque component produced by the interaction between the rotor-PM flux linkage and q-axis stator current, while the second term defines the reluctance torque due to magnetic saliency. Eq.(2.26) shows that, since $L_q > L_d$, i_d must be negative in order to ensure additive contribution of the reluctance torque. By assuming that the armature current space-phasor $\underline{i}_{dq}$ is oriented β electrical degrees ahead of the q-axis (i.e. β is defined positive in the counter-clockwise direction with respect to the positive q-axis), the torque expression (2.26) can be rewritten as

$$T_e = \frac{3}{2}p\left(\psi_{PM}\left|\underline{i}_{dq}\right|\cos\beta + \frac{1}{2}(L_q(i_q) - L_d)\left|\underline{i}_{dq}\right|^2 \sin 2\beta\right). \tag{2.27}$$

Fig. 2.3 shows, for a prototype double-layer IPMSM, the dependence of the electromagnetic torque and its components on the current angle β, for rated value of the armature-stator current. It can be observed, that the maximum of the reluctance torque is at $\beta=45^o$, and the maximum of the PM-alignment torque is at $\beta=0^o$. The total electromagnetic torque reaches its maximum for a current angle $0^o < \beta < 45^o$.

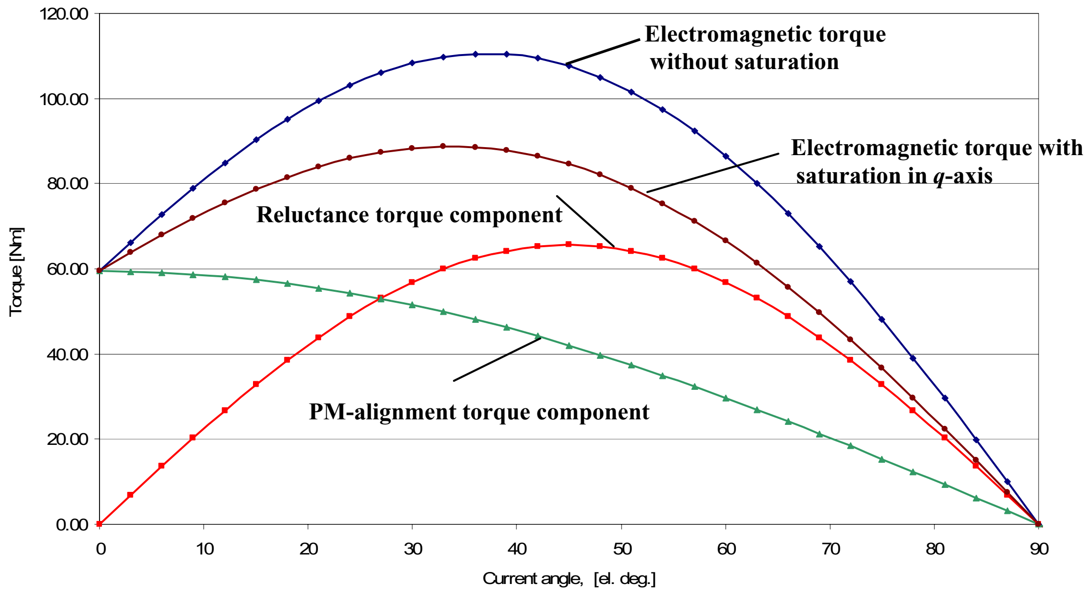

Fig. 2.3. IPMSM electromagnetic torque and its components vs. current angle $\vartheta = atan(-i_d/i_q)$
ψ_{PM}=0.0782 [Wb], I=169[A], L_{q0}=1.208 [mH], $L_q(i_q)=L_{q0}-a^2 i_q^2$= 0.84 [mH].

Constant-torque operation mode

Inverter-fed IPMSMs are compelled to operate in constant-torque and constant-power modes under terminal-voltage and armature-current constraints. Thus, the maximum available voltage U_M that the inverter can supply to the IPMSM is limited by the DC-link voltage, while the maximum stator-armature current I_M is determined by the thermal ratings of both the feeding voltage-source inverter and the stator-armature winding; IPMSM has therefore the following operating limits:

$$\sqrt{i_d^2 + i_q^2} = \left|\underline{i}_{dq}\right| \le I_M , \tag{2.28}$$

$$\sqrt{u_d^2 + u_q^2} \le U_M . \tag{2.29}$$

The IPMSM base speed, ω_b, defines the electrical angular speed, at which the magnitude of the terminal voltage expressed by Eq.(2.23) equals the available voltage U_M in Eq. (2.29), while the current is at its limit I_M. From standstill up to ω_b, the IPMSM is in the *constant-torque operation mode*, in which only the current limitation (2.28) is effective, whereas the voltage constraint (2.29) is simply fulfilled (since the back-emf is rather low). Moreover, the IPMSM can be operated in the constant-torque speed range from 0 to ω_b with maximum torque-to-armature current ratio, i.e. producing maximum torque with the permissible maximum stator-current amplitude. Such a condition is obtained by differentiating the electromagnetic torque expression (2.27) with respect to the stator-current space-phasor angle ϑ and equating to zero:

$$dT_e / d\vartheta = -\psi_{PM} \left|\underline{i}_{dq}\right| \sin\vartheta + (L_q(i_q) - L_d)\left|\underline{i}_{dq}\right|^2 \cos 2\vartheta = 0 \tag{2.30}$$

which leads to

$$\gamma^* = \sin^{-1}\frac{-\psi_{PM} + \sqrt{\psi_{PM}^2 + 8(L_q(i_q) - L_d)\left|\underline{i}_{dq}\right|^2}}{4(L_q(i_q) - L_d)\left|\underline{i}_{dq}\right|}. \tag{2.31}$$

Further investigation of Eq.(2.31) reveals that, under consideration of q-axis magnetic path saturation, the stator-current space-phasor angle γ^* exceeds 45 electrical degrees.

At the equality limit in the stator-current constraint (2.28), it results from Eqs.(2.27) and (2.31) the maximum torque that can be developed with the maximum armature current I_{max} during the constant-torque operation of the IPMSM:

$$T_{eM} = T_e(I_M, \gamma^*) = \frac{3}{2}p\left(\psi_{PM} I_M \cos\gamma^* + \frac{1}{2}(L_q(I_M \cos\gamma^*) - L_d) I_M^2 \sin 2\gamma^*\right). \tag{2.32}$$

So, until the terminal voltage reaches its limited value U_M at $\omega = \omega_b$, the motor can be accelerated with the constant torque value T_{eM} of Eq.(2.32), while the armature current space-phasor $\underline{i}_{dq}$ is kept fixed by its imposed polar coordinates (I_M, γ^*) under saturated conditions.

Constant-power operation mode

At rotor speeds higher than the base speed ω_b, IPMSM is running in *flux-weakening constant-power operation mode*, in which the motor torque capability is limited by both armature current and terminal voltage constraints of Eqs.(2.28) and (2.29), and is also strongly affected by the increasing iron losses. Hence, an equivalent iron-loss resistance R_c is introduced in the d- and q-axis equivalent circuits of the IPMSM, as shown in Fig.2.4. The IPMSM dynamic model of Eqs.(2.23)-(2.25) in dq rotor coordinates changes accordingly:

$$\begin{aligned} u_d &= Ri_d + \frac{d\psi_d}{dt} - \omega\psi_q = Ri_d + L_d\frac{di_{od}}{dt} - \omega L_q i_{oq} \\ u_q &= Ri_q + \frac{d\psi_q}{dt} + \omega\psi_d = Ri_q + L_q(i_{oq})\frac{di_{oq}}{dt} + \omega L_d i_{od} + \omega\psi_{PM} \end{aligned} \tag{2.33}$$

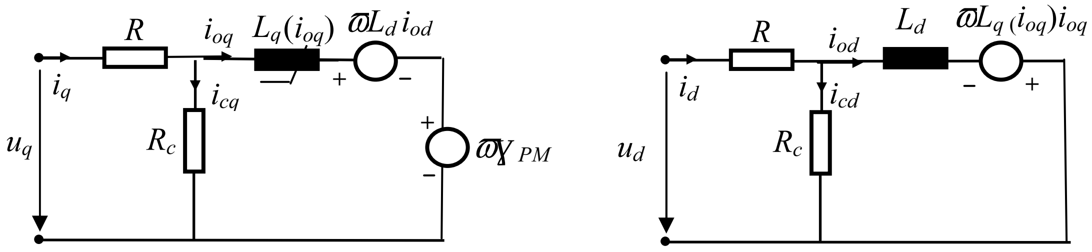

q-axis equivalent circuit including the iron losses

d-axis equivalent circuit including the iron losses

Fig. 2.4. Equivalent circuits of the IPMSM dynamic model in dq rotor coordinates including iron saturation and losses.

with the magnetizing currents i_{od}, i_{oq} and the iron-loss equivalent currents i_{cd}, i_{cq} defined by

$$
\begin{aligned}
i_{od} &= i_d - i_{cd} = i_d + \left(\varpi L_q(i_{oq}) i_{oq} - L_d \frac{di_{od}}{dt}\right) / R_c \\
i_{oq} &= i_q - i_{cq} = i_q - \left(\varpi(\psi_{PM} + L_d i_{od}) + L_q(i_{oq}) \frac{di_{oq}}{dt}\right) / R_c
\end{aligned}
\tag{2.34}
$$

and

$$
T_e = \frac{3}{2} p \left[\psi_{PM} i_{oq} + (L_d - L_q(i_{oq})) i_{od} i_{oq}\right] \tag{2.35}
$$

From Eqs.(2.33)-(2.35), the highest available electromagnetic torque of the IPMSM, subject to both current and voltage limits of Eqs.(2.28) and (2.29) in the flux-weakening constant-power speed range $\omega_b \leq \omega \leq \omega_{max}$, yields

$$
T_e = \frac{3}{2} p \left[\psi_{PM} i_{oq}^{*} + (L_d - L_q(i_{oq}^{*})) i_{od}^{*} i_{oq}^{*}\right] \tag{2.36}
$$

where

$$
\sqrt{i_{od}^{*2} + i_{oq}^{*2}} = I_M, \tag{2.37}
$$

$$
i_{od}^{*} = \frac{\psi_{PM} L_d - \sqrt{(\psi_{PM} L_d)^2 + (L_q^2(i_{oq}^{*}) - L_d^2)\left(\psi_{PM}^2 + L_q^2(i_{oq}^{*}) I_M^2 - \left(\frac{U_{oM}}{\varpi}\right)^2\right)}}{(L_q^2(i_{oq}^{*}) - L_d^2)} \tag{2.38}
$$

with the voltage limit

$$
U_{oM} = U_M - (R + R_c) I_M, \tag{2.39}
$$

which incorporates the voltage drop associated with iron losses as well as the stator-resistance voltage drop. Eqs.(2.36)-(2.39) clearly show that iron losses become the ultimate limiting factor of IPMSM output torque capability at high speeds.

2.3. Conclusions

The dynamic modeling of the IPMSM operating in constant-torque and constant-power flux-weakening modes has been presented. First, a nonlinear dynamic model of the IPMSM has been derived as a three-phase-variable circuit model accounting for parameter variations due to iron saturation.

Then, two-phase equivalent *dq* models for both constant-torque (with maximum torque-to-armature current ratio) and constant-power (with maximum-torque flux-weakening) operation modes of the IPMSM have been developed. These nonlinear dynamic models take into account the iron saturation and losses, respectively, thus being further useful for accurate IPMSM torque analysis and control.

Selected references

1. N. Bianchi, S. Bolognani, Magnetic models of saturated interior permanent-magnet motors based on finite element analysis. *Rec. IEEE Ind. Appl. Soc. Annu. Meet. Conf.*, 1998, Vol. 1, pp. 27-34.

2. N. Urasaki, T. Senjyu and K. Uezato, An accurate modeling for permanent-magnet synchronous motor drives. *Proc. IEEE-APEC 2000*, pp. 387–392.

3. E. C. Lovelace, T. M. Jahns, and J. H. Lang, A saturating lumped parameter model for an interior PM synchronous machine. *IEEE Trans. Ind. Applicat.*, Vol. 38 (2002), No. 3, pp. 645-650.

4. E. Levi, Saturation modelling in *d-q* axis models of salient pole synchronous machines. *IEEE Trans. Energy Convers*., Vol. 14 (1999), No. 1, pp. 44-50.

5. F. Fernandez-Bernal, A. G. Cerrada and R. Faure, Model-based loss minimization for DC and AC vector-controlled motors including core saturation. *IEEE Trans. Ind. Applicat.*, Vol. 36 (2000), No. 3, pp. 755–763.

6. G. Kang, J. Hong, G. Kim and J. Park, Improved parameter modeling of interior permanent magnet synchronous motor based on finite element analysis. *IEEE Trans. Magn.*, Vol. 36 (2000), No. 4, pp. 1867–1870.

7. J.-Y. Lee *et al*., Determination of parameters considering magnetic nonlinearity in an interior permanent magnet synchronous motor. *IEEE Trans. Magn.*., Vol. 42 (2006), No. 4, pp. 1303–1306.

8. B. Stumberger *et al*., Evaluation of saturation and cross-magnetization effects in interior permanent- magnet synchronous motor. *IEEE Trans. Ind. Applicat.*, Vol. 39 (2003), No. 5, pp. 1264–1271.

9. Y. Yan, J.G. Zhu and H.W. Lu, Study of a PMSM model incorporating structural and saturation saliencies. *Proc. 6th IEEE Int. Conf. Power Electron. Drive Syst.*, Kuala Lumpur, Malaysia, Nov.28-Dec.1, 2005, pp. 575-580.

10. Z.Q. Zhu, Y.S. Chen, and D. Howe, Iron loss in permanent-magnet brushless AC machines under maximum torque per ampere and flux weakening control. *IEEE Trans. Magn.*, Vol. 38 (2002), No. 5, pp. 3285-3287.

11. S. Morimoto *et al*., Loss minimization control of permanent-magnet synchronous motor drives. *IEEE Trans. Ind. Electron.*, Vol. 41 (1994), No. 5, pp. 511–517.

Chapter 3

FLUX DISTRIBUTION AND TORQUE ANALYSIS OF INTERIOR PERMANENT-MAGNET SYNCHRONOUS MOTORS

3.1. Magnetic-flux distribution analysis and parameter estimation

Knowledge of the spatial flux distribution in an IPMSM is essential for determining motor quantities like back-emfs, inductances, electromagnetic torque components, iron losses etc. As long as two-dimensional analysis is concerned, the approaches can be divided into: *analytical methods*, usually based on equivalent magnetic circuits [1-3], and *numerical methods*, using finite-element field computations [4-7].

This section firstly presents an equivalent magnetic circuit-based analysis of a double-layer IPMSM allowing the estimation of the rotor-PM sizes as well as the rated values of PM-rotor and armature-stator fluxes, back-emfs and unsaturated *dq* inductances. Then, a finite-element field analysis of the flux distribution in both single- and double-layer IPMSMs, at no-load and rated-load conditions, is performed, accounting for magnetic saturation in stator and rotor iron parts. The nonlinear dependence of *dq* inductances on the stator-armature current is then obtained.

Equivalent magnetic circuit-based analysis

The given stator-armature geometry and other specifications of the considered double-layer IPMSM are the following:

- Outer stator diameter: 240 mm;
- Inner stator diameter: 165 mm;
- Active axial length of the motor: 123 mm;
- Shaft diameter: 85 mm;
- Stator slots number : 54;
- Stator phase number: 3;
- Pole-pair number: 3;
- Rated output torque of 80 Nm at the rated speed of 2000 rpm;
- Field-weakening operation from rated speed up to a maximum speed of 6000 rpm;
- Airgap flux-density-fundamental amplitude between 0.5 and 1 T;
- Maximum flux density in the rotor yoke: 1.7 T;
- Maximum flux density in the stator yoke: 1.7 T;
- Maximum flux density in the stator teeth: 1.65 T;

- Remanent flux density and relative recoil permeability of the rotor-PM:Nd-Fe-B material: 1.15 T and 1.05, respectively.

The IPMSM cross-section corresponding to a single-pole PM-rotor region is shown in Fig.3.1. The number of slots per pole and phase is

$$q = \frac{N_{ss}}{2mp} \tag{3.1}$$

where N_{ss} is the number of stator slots, m, the number of phases, and p, the pole-pair number.

The stator-slot pitch is

$$\tau_s = \frac{D_{si} \cdot \pi}{N_{ss}} \tag{3.2}$$

with D_{si} denoting the inner diameter of the stator core.

A full-pitched one-layer star-connected three-phase stator-armature winding is considered with a winding factor k_{we} expressed as [2, 3]

$$k_{we} = \frac{\sin\left(q \frac{\gamma_s}{2}\right) \sin\left(\frac{\pi}{6 \cdot q}\right)}{q \sin\left(\frac{\gamma_s}{2}\right) \frac{\pi}{6 \cdot q}} \tag{3.3}$$

where γ_s represents the electrical angle between two slots, i.e.

$$\gamma_s = \frac{\pi}{3q} \tag{3.4}$$

The equivalent smooth air-gap g', which takes into account the stator-slot openings, is written according to [2, 3]:

$$g' = g \frac{w_{so} + w_{st}}{w_{so} + w_{stg} - k_C \cdot g} \tag{3.5}$$

where the stator-slot Carter coefficient k_C is [2, 3]

$$k_C = \frac{w_{so}}{2 \cdot g} \tan^{-1}\left(\frac{w_{so}}{2 \cdot g}\right) - \log\left(\frac{\sqrt{w_{so}^2 + (2 \cdot g)^2}}{2 \cdot g}\right) \tag{3.6}$$

with g', the corrected airgap; w_{so}, the width of stator-slot opening; w_{st}, the stator-teeth width; w_{stg}, the width of the stator teeth at the airgap.

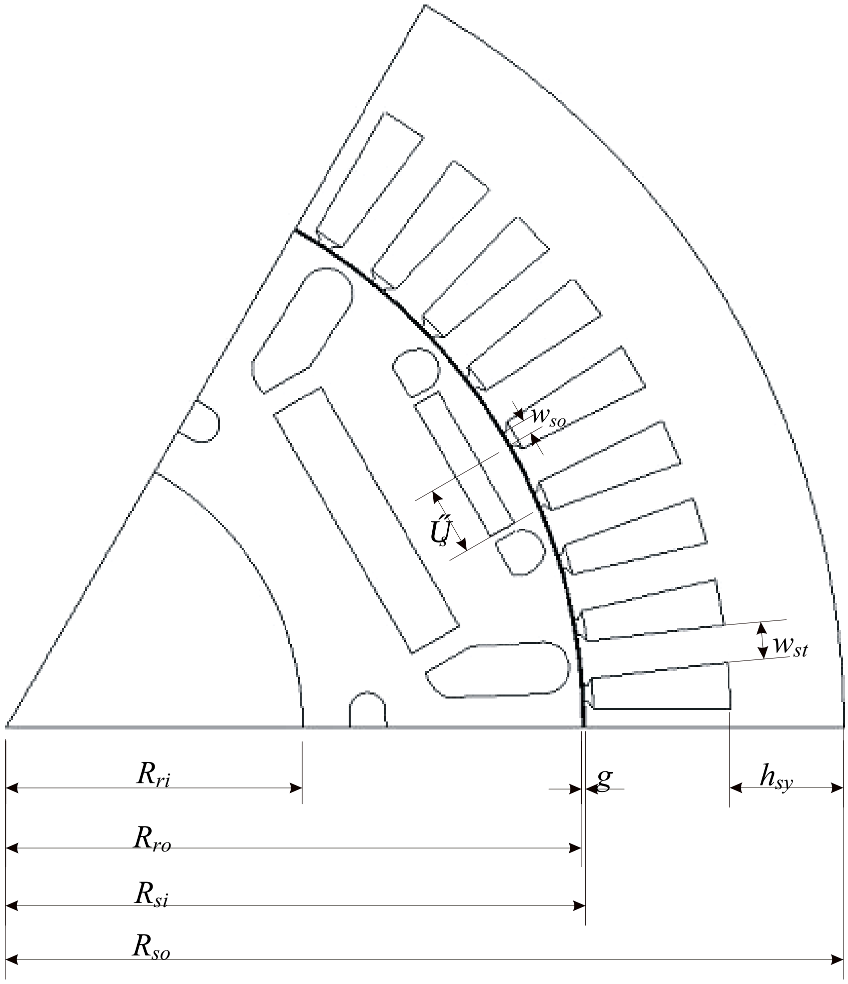

Fig.3.1. Single-pole cross-section of the double-layer IPMSM.

The rotor configuration of the double-layer IPMSM is shown in Fig.3.2. It consists of PMs, flux barriers, and iron bridges. Two layers of cavities are shaped to accommodate rectangular-parallelepiped Nd-Fe-B magnets, which are cheap to manufacture. The internal bridges are used to keep the magnets in place, while the external bridge is necessary to provide a smooth flux path at the airgap. The width of the flux barriers is equal to the magnet height.

The *d*-axis inductance equivalent magnetic circuit for the double-layer IPMSM for rotor-PM height determination is shown in Fig.3.3. It assumes constant magnetic potential (i.e. infinite permeability) in the iron parts, fixed magnetic remanence and fully saturated external bridges, which provide constant flux density at the rotor periphery. Despite the magnetically-salient rotor geometry, the stator teeth are all uniform, and can therefore yield their average flux carrying capability.

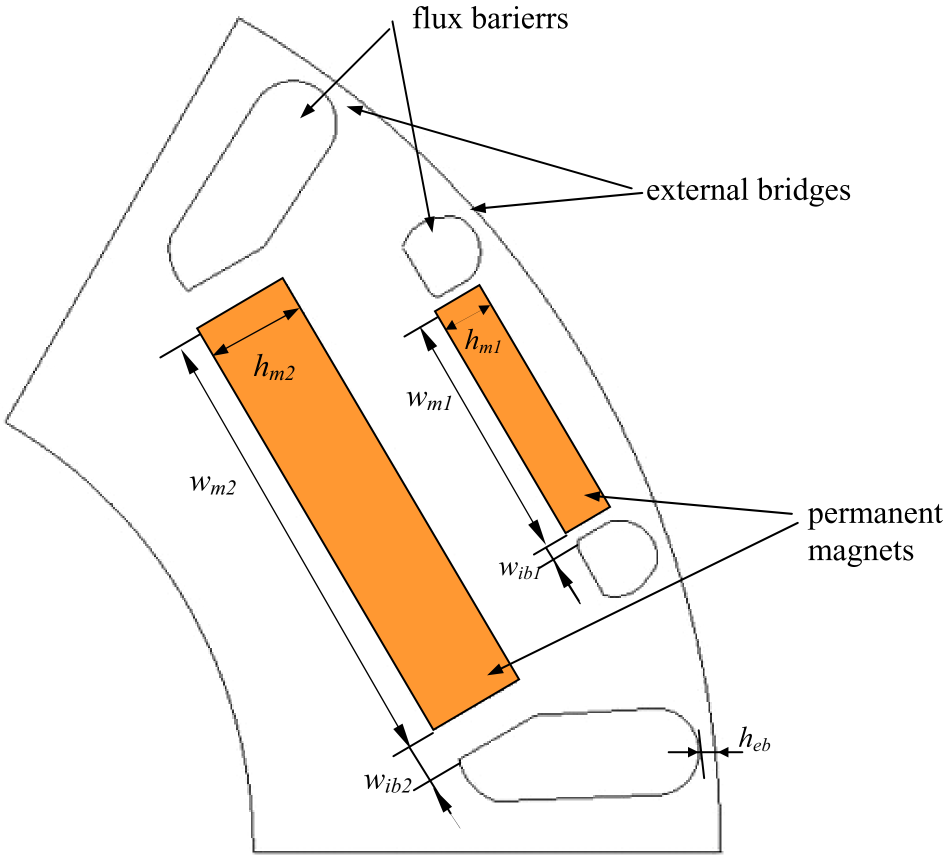

Fig.3.2 Single-pole rotor configuration of the double-layer IPMSM.

The stator is represented by the maximum flux available in the airgap, Φ_{max}. This can be defined as a function of stator packing constraints, armature winding and maximum flux density in the airgap:

$$\Phi_{\max} = \frac{D_{si} L k_{sk} N_{tph} B_{\delta \max}}{p} \tag{3.7}$$

where L is the axial length of the motor, k_{sk}, the stacking factor ($k_{sk} = 0.95$), N_{tph}, the number of turns per phase, and $B_{\delta max}$, the maximum airgap flux density.

The maximum airgap flux density is estimated by taking into account the stator geometry and the saturated flux density of the iron:

$$B_{\delta \max} = \frac{w_{st} \cdot B_{sat\_Fe}}{\vartheta_s} \tag{3.8}$$

where $B_{sat\text{-}Fe}$ was set as 1.7 T.

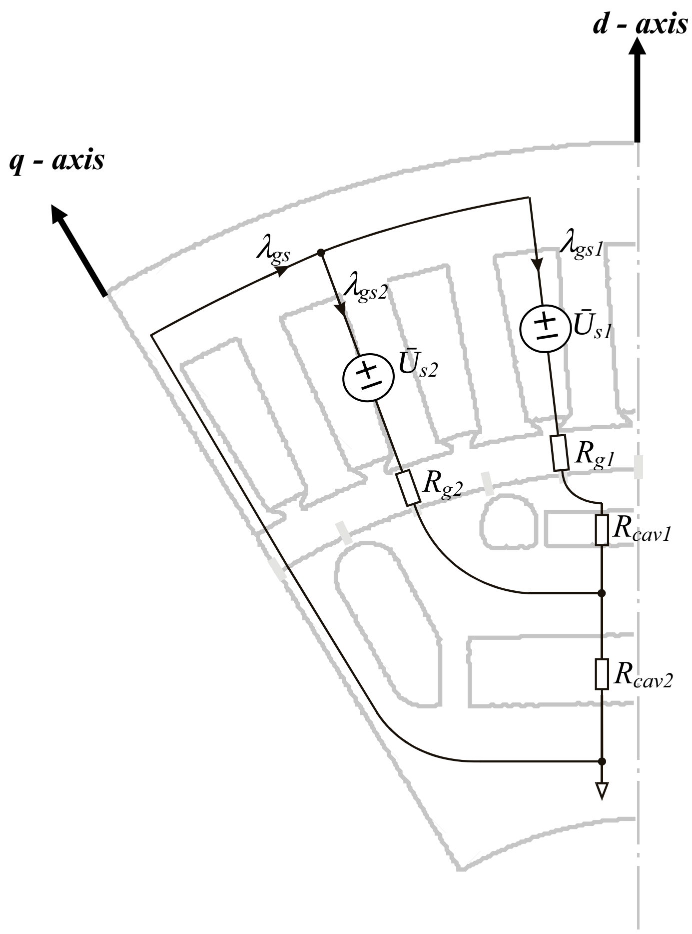

Fig.3.3 Equivalent *d*-axis inductance magnetic circuit for the double-layer IPMSM.

Depending on the number of rotor-PM layers, the rotor surface per pole is divided in n_{rd} equidistant segments:

$$n_{rd} = 4 \cdot n_{ml} - 2 \cdot n_d \tag{3.9}$$

where n_{ml} defines the number of magnet layers, and n_d is the number of *d*-axes.

Initially, only cavities (flux barriers) are considered in the rotor geometry; they are designed parallel to the *q*-axis. The cross-sectional area for the cavity A_{cav} is

$$A_{cav} = w_{cav} \cdot L \tag{3.10}$$

where w_{cav} represents the average length of the cavity, referred to the width of the magnets and the height of the flux barrier on the radial direction.

The area for one element of the airgap A_{gk} is calculated as

$$A_{gk} = \frac{D_{si} \cdot \phi \cdot n_{rd}}{p} \cdot L \tag{3.11}$$

The expressions for the reluctance R_{gk} of the k^{th} airgap segment and for k^{th} cavity reluctance R_{cavk}, considered in the equivalent magnetic circuit of Fig.3.3, are written as follows:

$$R_{gk} = \frac{g'}{\sigma_0 \cdot A_{gk}} \tag{3.12}$$

$$R_{cavk} = \frac{h_{cavk}}{\sigma_0 \cdot A_{cav}} \tag{3.13}$$

The airgap mmf is only produced through the stator-armature energization. Fig.3.4 shows a sketch of a typical distribution of the airgap mmf, in which the value $\bar{U}_{gs}$ is expressed as a function of the number of turns per phase N_{tph}, and the phase current I_{ph}:

$$N_{gs} = \frac{3}{2} N_{tph} \cdot I_{ph} \tag{3.14}$$

For the k^{th} section of the air-gap (Fig.3.4), the mmf is calculated as

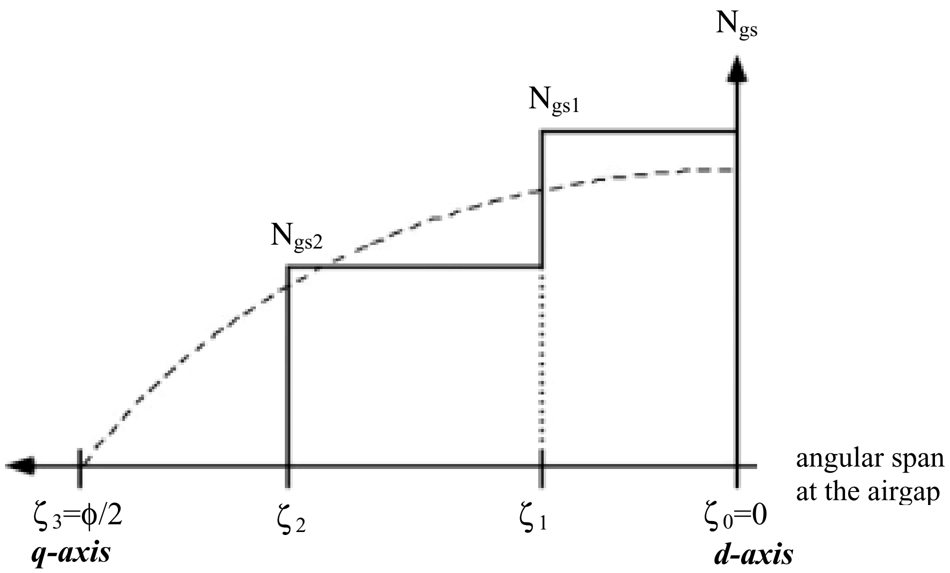

Fig.3.4. Schematic *d*-axis stator-armature mmf function (dashed line showing its fundamental).

$$N_{gsk} = \frac{N_{gs}}{2} \cos\left(\frac{(2k-1) \cdot \phi}{n_{rd}}\right) \tag{3.15}$$

The k^{th} component of flux in the air-gap, λ_{gsk} is modelled by the function

$$\lambda_{gsk} = \frac{\lambda_{\max}}{2} \frac{\phi}{p \cdot n_{rd}} \cos\left(\frac{(2k-1) \cdot \phi}{n_{rd}}\right) \tag{3.16}$$

With

$$\lambda_{\max} = \frac{\psi_{\max}}{N_{tph}} \tag{3.17}$$

Based on the circuit of Fig.3.3, the following equations can be written:

$$N_{gs2} = \lambda_{gs2} \cdot R_{g2} - (\lambda_{gs1} - \lambda_{gs2}) \cdot R_{cav2} \tag{3.18}$$

$$N_{gs1} = \lambda_{gs1} R_{g1} - \lambda_{gs1} \cdot R_{cav1} - (\lambda_{gs1} - \lambda_{gs2}) \cdot R_{cav2} \tag{3.19}$$

Solving Eqs. (3.18) and (3.19), the following expressions for the cavity heights h_{cav1}, h_{cav2} are obtained:

$$h_{cav1} = \sigma_0 \cdot w_{cav1} \cdot L \cdot \frac{N_{gs2} + \lambda_{gs2} \cdot R_{g2}}{\lambda_{gs1} - \lambda_{gs2}} \tag{3.20}$$

$$h_{cav2} = \sigma_0 \cdot w_{cav2} \cdot L \frac{N_{gs1} + \lambda_{gs1} \cdot R_{g1} + (\lambda_{gs1} - \lambda_{gs2}) \cdot R_{cav2}}{\lambda_{gs1}} \tag{3.21}$$

Part of the cavities are filled with PM material, and thus the height of the k^{th} cavity is equal to that of the k^{th} magnet: $h_{cavk} = h_{mk}$.

A similar equivalent *d*-axis PM circuit (Fig. 3.5) is used to calculate the rotor-PM width w_{mk} for the double-layer IPMSM. The same assumptions of constant magnetic potentials in the iron core (i.e. infinite permeability), fixed magnet remanence and saturated iron bridges, at the rotor periphery and at the end of the magnets are adopted. Since the rotor-PM flux is oriented along the *d*-axis, the same basic circuit is analyzed with the stator mmf source removed, and the flux sources added. The rotor-PM is represented by a flux source λ_{mk} proportional to its remanent flux density B_r and its magnetic reluctance R_{mk}. The internal and external bridges are modelled as flux sources λ_{bik}, λ_{bek} which oppose the PM flux λ_{mk}. The following quantities are needed to solve the equivalent magnetic circuit:

- the reluctance of the magnet

$$R_{mk} = \frac{h_{mk}}{\sigma_0 \cdot \sigma_r \cdot L w_{mk}} \tag{3.22}$$

- the area of the k^{th} internal bridge used to fix the k^{th} magnet

$$A_{bik} = w_{bik} \cdot L \tag{3.23}$$

with w_{bik}, the width of the the k^{th} internal bridge;

- the area of the external bridges A_{bek}

$$A_{bek} = h_{bek} \cdot L \tag{3.24}$$

with h_{bek}, the height of the k^{th} external bridge; the value of h_{bek} is set as 1.4 mm.

The magnets should provide in the airgap a flux λ_{gm} equal to k_u part of the maximum flux λ_{max} that the motor can produce:

$$\lambda_{gm} = k_u \cdot \lambda_{\max} \tag{3.25}$$

with k_u=0.65 representing the utilization factor.

The flux produced by the rotor-PM in the airgap is expressed as

$$\lambda_{gmk} = \frac{\lambda_{gm}}{2}\frac{\phi}{p \cdot n_{rd}}\cos\left(\frac{(2k-1)\cdot\phi}{n_{rd}}\right) \tag{3.26}$$

where symmetry was considered.

From the equivalent magnetic circuit of Fig.3.5, the PM-flux expressions can be written as

$$\lambda_{m1} = \lambda_{gm1} + \lambda_{bi1} + \lambda_{be1} \tag{3.27}$$

$$\lambda_{m2} = \lambda_{gm1} + \lambda_{gm2} + \lambda_{bi2} + \lambda_{be2} \tag{3.28}$$

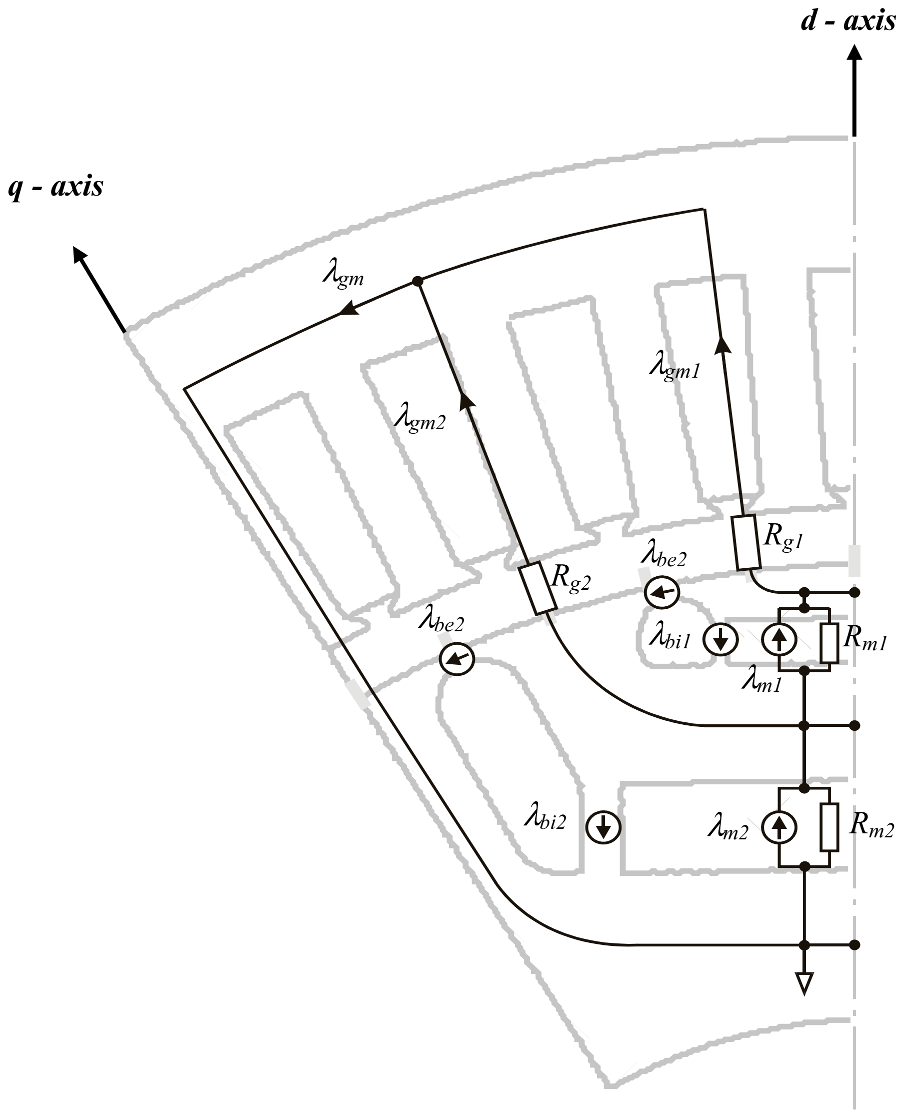

Fig.3.5. Equivalent *d*-axis PM circuit for the double-layer IPMSM.

where the fluxes in the internal and external bridges are calculated according to

$$\lambda_{bik} = B_{sat} \cdot A_{bik} \tag{3.29}$$

$$\lambda_{bek} = B_{sat} \cdot A_{bek} \tag{3.30}$$

$$B_m = B_r + \mu_0 \cdot \mu_r \cdot H_m \tag{3.31}$$

with B_m, H_m, the magnet flux density and magnetic field strength, respectively, for a given operating point. Eq. (3.31) defines the PM characteristic. The expressions for PM widths w_{m1}, w_{m2} are obtained after solving Eqs (3.27) and (3.28) by means of Eqs. (3.29)-(3.31):

$$w_{m1} = \frac{2(\lambda_{gm1} + \lambda_{bi1} + \lambda_{be1})}{B_m \cdot L} \tag{3.32}$$

$$w_{m2} = \frac{2(\lambda_{gm1} + \lambda_{gm2} + \lambda_{bi2} + \lambda_{be2})}{B_m \cdot L} \tag{3.33}$$

The geometric parameters of the double-layer IPMSM, resulting from the previous equivalent magnetic circuit-based analysis, are presented in Table 3.1 together with those of a single-layer IPMSM of similar design.

Table 3.1. Geometric parameters of the single- and double-layer IPMSMs

Geometric parameter	Single-layer IPMSM	Double-layer IPMSM
Phase number	3	3
Number of stator slots	54	54
Number of rotor poles	6	6
Stator outer diameter [mm]	240	240
Stator inner diameter [mm]	165	165
Airgap length [mm]	0.4	0.4
Rotor inner diameter [mm]	85	85
Stack length [mm]	123	123
Width of PM-layer 1 [mm]	38	21
Width of PM-layer 2 [mm]	-	39
Height of PM-layer 1 [mm]	9	4
Height of PM-layer 2 [mm]	-	7.8
Radius of PM-layer 1 [mm]	63.8	73
Radius of PM-layer 2 [mm]	-	59
Rotor-bridge thickness [mm]	1.4	1.4
Stator-yoke height [mm]	16.2	16.2
Stator-tooth width [mm]	5.4	5.4
Stator-slot depth [mm]	20.9	20.9
Stator-slot opening [mm]	2.2	2.2
Tooth-tip height [mm]	0.5	0.5
Number of slots/pole/phase	3	3
Number of turns/ slot	7	7
Number of parallel branches	1	1
Slot-filling factor	0.44	0.44

Estimation of unsaturated *q*- and *d*-axis inductances

It is assumed that the *q*-axis flux enters along the periphery of the rotor except those regions already saturated by the magnets (external bridges). The condition for the *q*-flux can be written as

$$\lambda_{qsk} = \lambda_{qrk} \tag{3.34}$$

where λ_{qsk} represents the flux produced by the stator-armature in k^{th} segment, whereas λ_{qrk} is the flux flowing through k^{th} rotor-yoke section. The flux produced in the airgap by the stator is

$$\lambda_{qsk} = \frac{B_{sat} \cdot (1 - k_{ps}) \cdot D_{si} \cdot L k_{sk}}{p} \cdot \frac{\pi}{n_{rd}} \sin\left(\frac{(2k-1) \cdot \pi}{n_{rd}}\right) \tag{3.35}$$

with k_{ps}, the ratio of stator-slot width to stator-slot pitch [9], i.e.

$$k_{ps} = \frac{\vartheta_s - w_{st}}{\vartheta_s}, \tag{3.36}$$

and the flux in the rotor yoke can be expressed as

$$\lambda_{hqk} = B_{sat} \cdot A_{hqk}, \tag{3.37}$$

where

$$A_{hqk} = L k_{sk} \cdot h_{qk}. \tag{3.38}$$

The total height of the *q*-flux path results from

$$h_{qs} = \sum h_{qk} = \sum D_{is} (1 - k_{ps}) \cdot \frac{\pi}{p \cdot n_{rd}} \cdot \sin\left(\frac{(2k-1) \cdot \pi}{n_{rd}}\right). \tag{3.39}$$

Hence, the (mean) flux-path length l_f over one pole can be determined by

$$l_f = 2 \cdot (h_{ss} - R_{ro} - R_{ri} - h_{qs}) + 2 \cdot h_{sy} + \pi \cdot \frac{R_{ro} - R_{ri} - h_{qs}}{2p} + \pi \cdot \frac{D_{so} - h_{sy}}{2p}, \tag{3.40}$$

where h_{ss} denotes the stator-slot height, and h_{sy}, the height of stator yoke. Finally, an estimation of the *q*-axis inductance can be derived as

$$L_q = \frac{3}{2} k_{we} \cdot N_{tph}^2 \cdot L k_{sk} \cdot D_{si} \cdot \mu_0 \frac{1}{\left(2 \cdot g + \frac{l_f}{\mu_{rr}}\right) p^2}, \tag{3.41}$$

while the d-axis inductance is obtained using Eq.(3.41) and magnetic saliency ratio ξ:

$$L_d = L_q / \xi . \tag{3.42}$$

The main electromagnetic parameters (and some other useful data) of the double-layer IPMSM, obtained from the previous equivalent magnetic circuit-based analysis at the rated operating point, are given in Table 3.2, together with those of a single-layer IPMSM of similar design.

Table 3.2. Rated values of main electromagnetic parameters for the single- and double-layer IPMSMs

Physical quantity	Single-layer IPMSM	Double-layer IPMSM
Rotor-PM flux [Vs]	0.0782	0.0782
Maximum stator-armature flux [Vs]	0.1202	0.1202
Back-emf [V]	75.55	75.55
PM-induced back-emf [V]	49.1	49.1
L_{dm} d-axis magnetizing inductance [mH]	0.179	0.201
L_{qm} q-axis magnetizing inductance (unsaturated) [mH]	1.216	1.208
Armature-winding phase resistance [mΩ]	15.55	15.55
Armature-winding losses [W]	201.32	201.32
Rotor-PM mass [kg]	1.867	2.156
Total active mass [kg]	37.63	38.65
Rotor inertia [kg m^2]	40.66e-3	43.89e-3

Additionally, in Table 3.2, the total mass of the IPMSM active materials has been calculated as

$$w_{mot} = w_{sy} + w_{st} + w_{ry} + w_{Co} + w_m \tag{3.43}$$

with the mass of the stator yoke, w_{sy} , stator teeth, w_{st} , rotor yoke, w_{ry} , stator-armature winding, w_{Co} and rotor-PMs, w_m , respectively, given by

$$w_{sy} = \rho_{Fe} \cdot k_{st} \cdot L \cdot \pi (R_{so}^2 - R_{si}^2) \tag{3.44}$$

$$w_{st} = \rho_{Fe} \cdot k_{st} \cdot L \cdot N_{ss} (h_{ss} \cdot w_{st} + 2 \cdot h_{stg} \cdot w_{stg}) \tag{3.45}$$

$$w_{ry} = \rho_{Fe} \cdot k_{st} \cdot L \cdot (\pi (R_{ro}^2 - R_{ri}^2) - 2 \cdot p \cdot w_m h_m - A_{fb}) \tag{3.46}$$

$$w_{Co} = m \cdot \rho_{Co} \cdot L_{Co} \cdot N_{tph} \cdot S_{cond} \cdot p \tag{3.47}$$

$$w_m = \rho_m \cdot L \cdot 2 \cdot p \cdot w_m \cdot h_m \tag{3.48}$$

and the rotor inertia has been determined as

$$J = \left(R_{ro}^2 - R_{ri}^2\right)(w_{ry} + w_m) \tag{3.49}$$

Finite-element field analysis

The finite element (FE) method allows a nonlinear analysis of the magnetic flux distribution and an accurate estimation of the saturated *dq* inductances as well as the torque components of the IPMSM.

For the two-dimensional (2D) FE field analysis of both single- and double-layer IPMSM, the commercial software package Flux-2D™ from Cedrat, France [8] has been used. The following Flux-2D™ modules, which come with powerful and interactive graphical user interface, have been applied in the IPMSM numerical field analysis:

- **Geometry -** defining the configuration and the FE-mesh of a specific field region;
- **Material database** - describing the physical proprieties of materials used during the simulation process (e.g. magnetization curves);
- **Solving process** - making possible the FE calculations using the magnetic vector potential method;
- **Post-processing results** - allowing an exhaustive calculation of the local and global electromagnetic quantities (e.g. flux linkage, back-emf, torque etc).

Flux-2D can exploit symmetries of the IPMSM cross-section. Thus, it is possible to represent only one-pole region of the motor, i.e. a sector of 60 mechanical degrees. An example of the triangular FE mesh for the two-layer IPMSM sextant cross-section is presented in Fig.3.6. The quality of the created FE-mesh has been estimated by (i) number of excellent-quality elements: 97.44 %; (ii) number of good-quality elements: 1.92 %; (iii) number of average-quality elements: 0.53 %; (iv) number of poor-quality elements: 0.11 %; (v) number of abnormal elements: 0 %.

The definition of the star-connected three-phase one-layer distributed stator-armature winding is given in Fig.3.7. It is the same for both single- and double-layer IPMSMs.

To obtain the magnetic flux distribution in the IPMSM relevant cross-section, a series of magnetostatic field calculations at different rotor positions in a complete electrical cycle has been computed by 2D-FE method solving the governing field differential equation:

$$\frac{\partial}{\partial x}\left(\nu \frac{\partial A_z}{\partial x}\right) + \frac{\partial}{\partial y}\left(\nu \frac{\partial A_z}{\partial y}\right) = -J_z - \nu_0\left(\frac{\partial M_y}{\partial x} - \frac{\partial M_x}{\partial y}\right) \tag{3.50}$$

where ν, ν_0 denote the reluctivity and the reluctivity of air, respectively, A_z, J_z are the magnetic vector potential and armature-winding current density *z*-components, respectively, and M_x, M_y, represent the rotor-PM magnetization *xy*-components. The nonlinearity of the stator and rotor iron-core material is accounted for by a cubic spline-approximated single-valued *B–H* curve.

Figs. 3.8 and 3.9 display the flux distributions in the single- and double-layer IPMSM, respectively, under *open-circuit condition* and for a given rotor position. The aim of these FE magnetostatic simulations was to establish the PM-excitation flux-density values in relevant field regions of the motor cross-section (rotor yoke, stator teeth and stator yoke). Hence, there is no current in the armature-stator winding. It is obvious from Figs. 3.8 and 3.9

that, for both IPMSMs, (i) the rotor internal and external iron bridges reveal the highest flux-density values, while the stator teeth are not affected by magnetic saturation; (ii) the rotor leakage flux mainly passes around the PM edges.

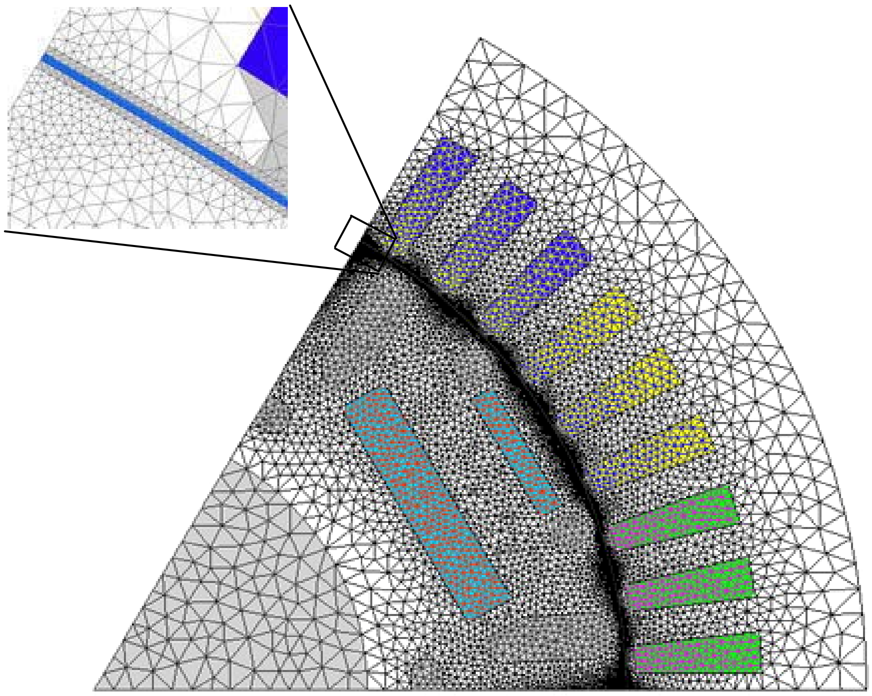

Fig.3.6. FE triangular mesh for the sextant cross-section of the double-layer IPMSM.

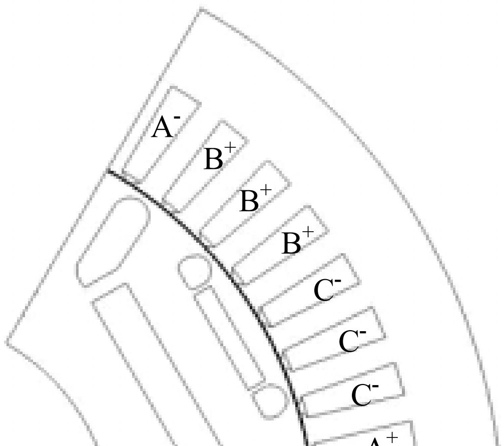

Fig.3.7. Armature-winding distribution in the IPMSM sextant cross-section.

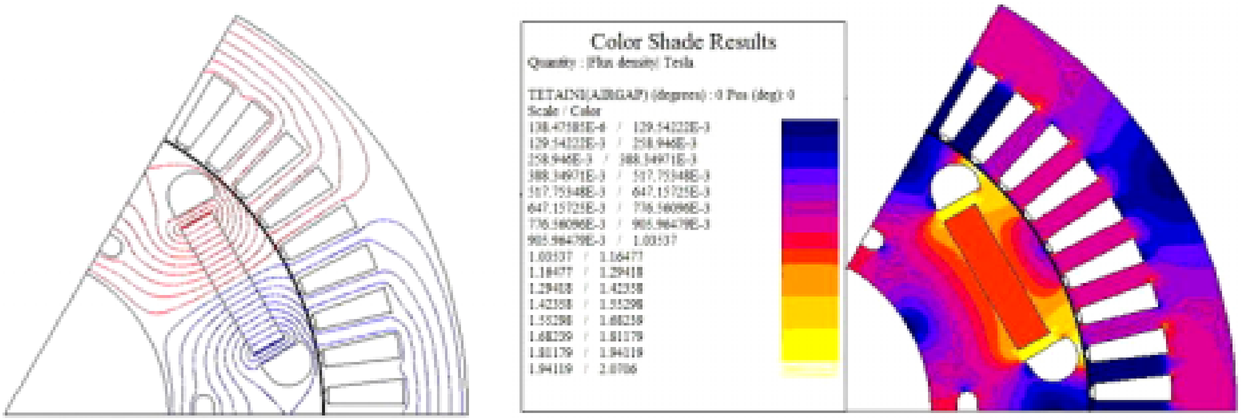

Fig.3.8. Magnetic flux distribution in the sextant cross-section of the single-layer IPMSM under open-circuit condition.

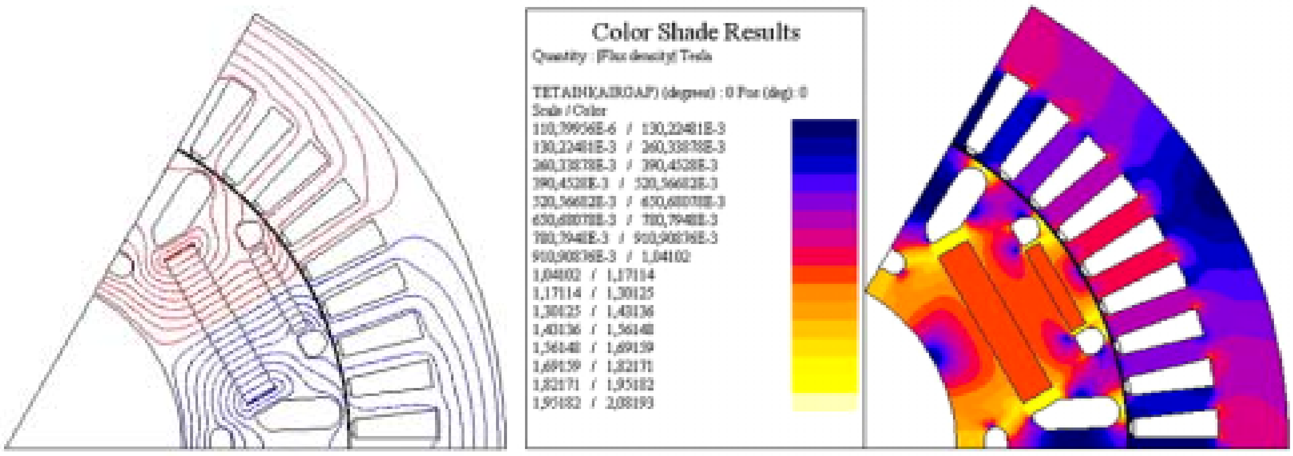

Fig.3.9. Magnetic flux distribution in the sextant cross-section of the double-layer IPMSM under open-circuit condition.

The flux-density normal and tangential components in the middle of the airgap as a function of rotor position (for an angular span covering two poles) are shown in Figs.3.10 and 3.11 for the single- and double-layer IPMSM, respectively. It is to be seen that the waveform of the normal component of the airgap flux density is much closer to a sinusoid for the double-layer IPMSM.

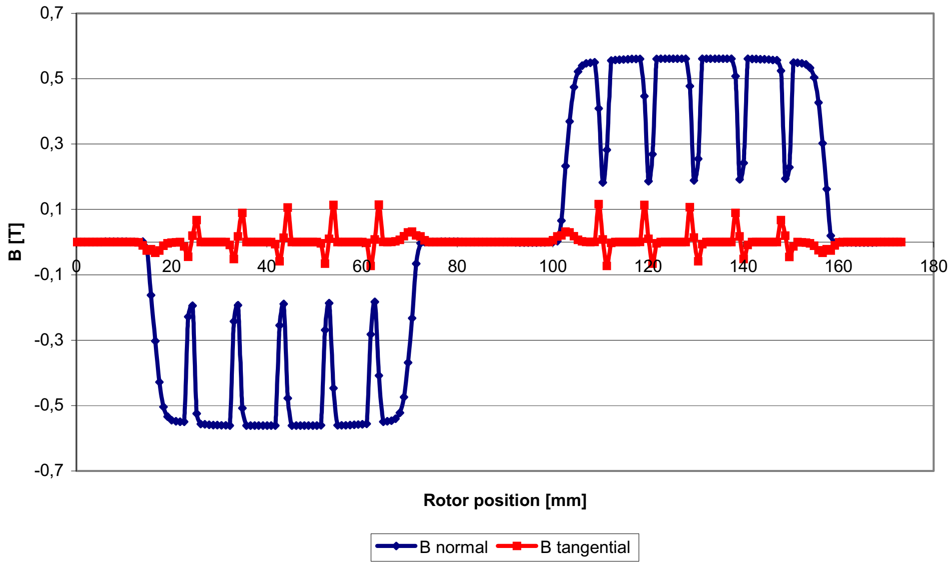

Fig.3.10. Airgap flux-density components for the single-layer IPMSM under open-circuit condition.

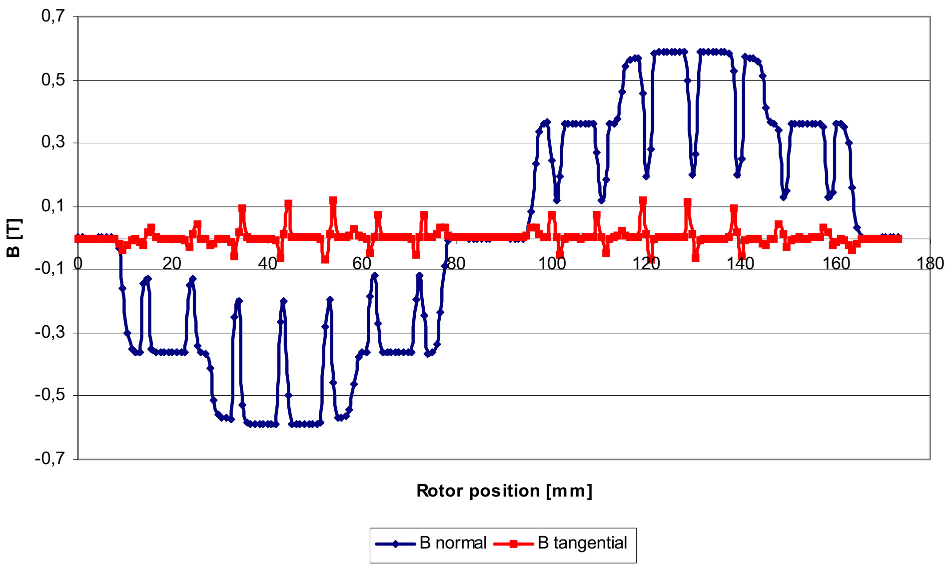

Fig.3.11. Airgap flux-density components for the double-layer IPMSM under open-circuit condition.

The magnetic flux distribution in the whole cross-section of both single- and double-layer IPMSMs is further computed under *rated-load condition*, i.e. at the rated (base) speed, at which the output torque is developed for the maximum (sinusoidal) current flowing in the stator-armature winding, without exceeding the maximum temperature allowed by the class of insulation, as well as the maximum terminal voltage available from the inverter. Beside the magnitude I_R of the rated armature-current vector, its position with respect to the *q*-axis (angle ɔ) for achieving maximum developed torque has been considered. For 2D-FE simulations, the parameters which are given or calculated are the number of ampere-turns per slot, the armature current density, the slot-fill factor and the area of slot cross-section, the latter being determined from the slot dimensions, which result from the stator outer and inner diameters, as well as the yoke and tooth thicknesses. Figs. 3.12 and 3.13 show the flux distributions in the single- and double-layer IPMSM, respectively, under rated-load condition and for a certain rotor position. Considerable magnetic saturation can be observed not only in the rotor region of internal and external iron bridges, but also in stator-tooth areas as an armature-reaction effect.

The modified waveform of airgap flux-density components due to the armature reaction under rated-load condition, is displayed in Fig.3.14 for the double-layer IPMSM.

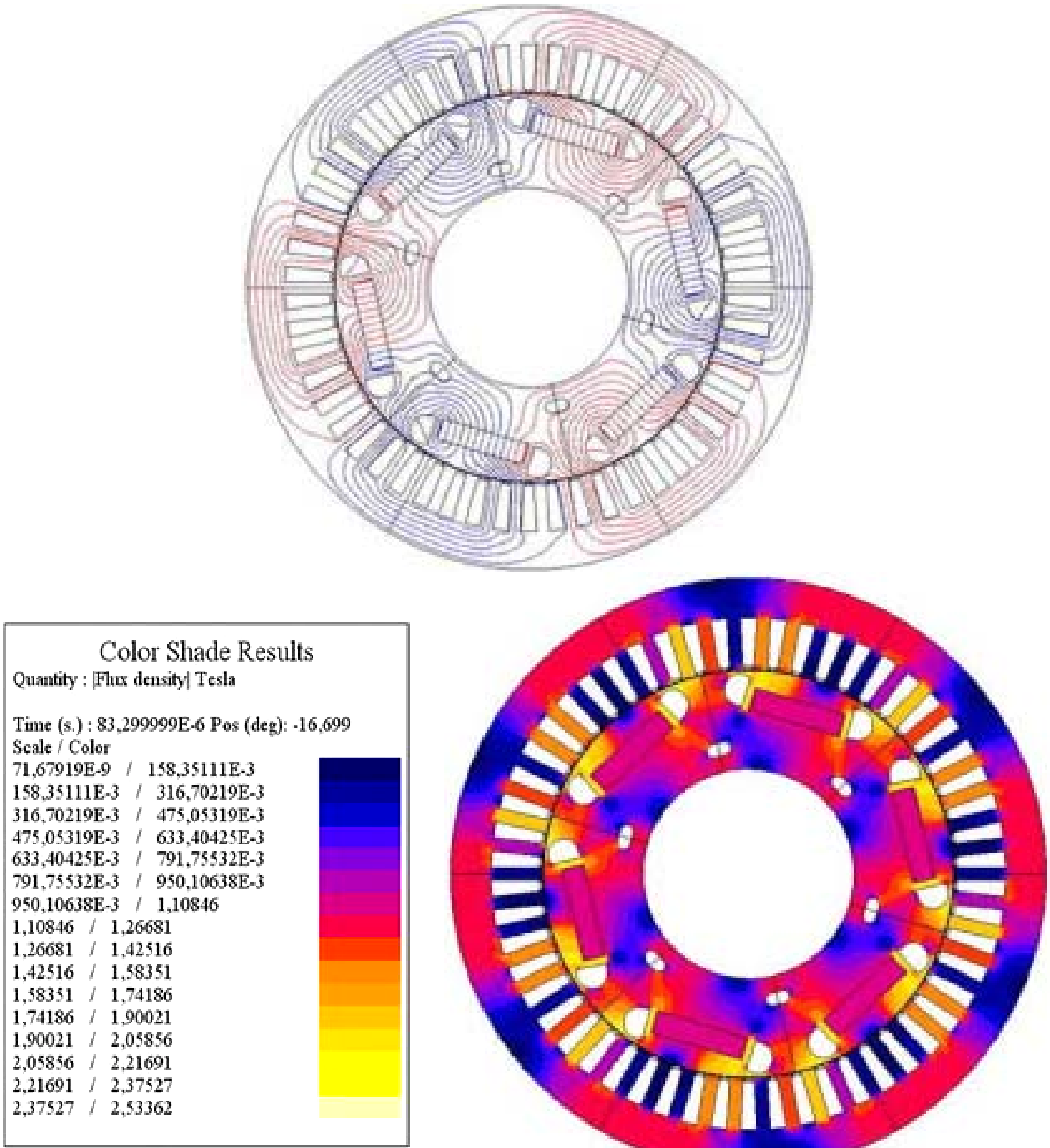

Fig.3.12. Magnetic flux distribution in the cross-section of the single-layer IPMSM under rated-load condition.

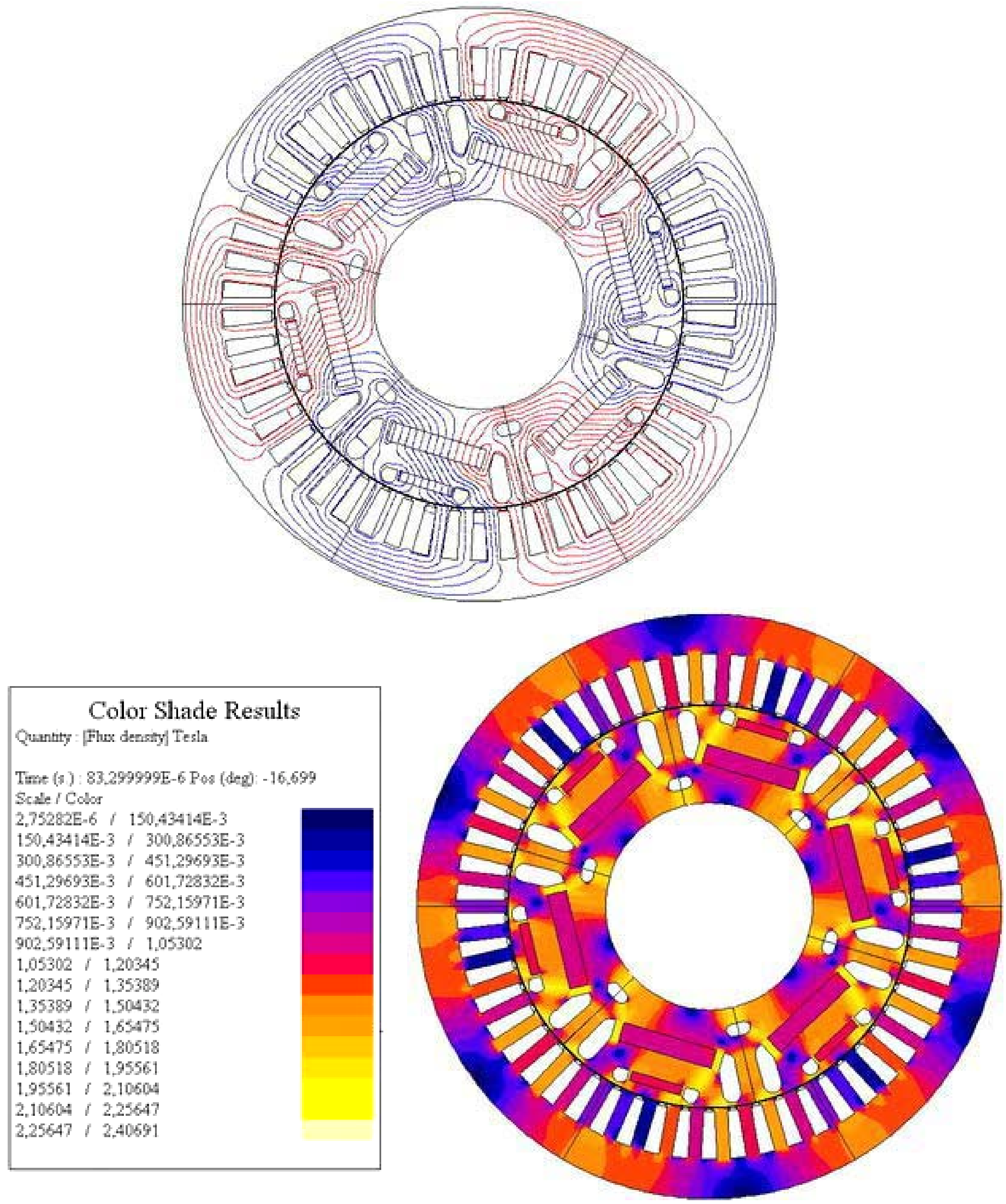

Fig.3.13. Magnetic flux distribution in the cross-section of the double-layer IPMSM under rated-load condition.

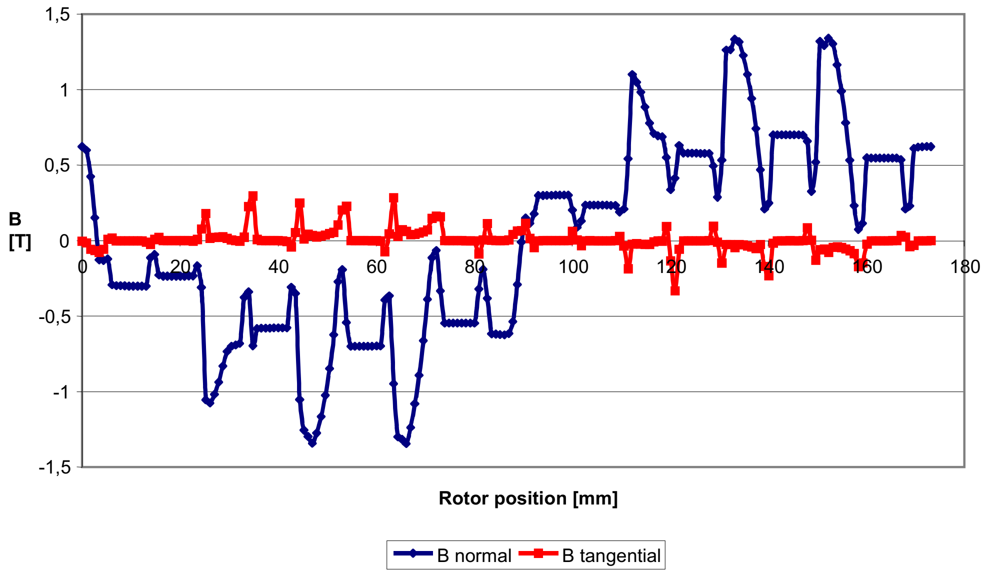

Fig.3.14. Airgap flux-density components for the double-layer IPMSM under rated-load condition.

Estimation of saturated *q*- and *d*-axis inductances

2D-FE field analysis allows accurate determination of IPMSM inductances through magnetic flux distribution solutions as it takes into account the actual distribution of armature-winding, details of cross-sectional geometry, and the nonlinearity of magnetic materials. The estimation of IPMSM *d,q* inductances is essential for predicting its torque and flux-weakening capabilities.

The most effective approach to calculate the saturated inductances L_d, L_q of single- and double-layer IPMSMs under rated-load condition and for a certain rotor position is to preserve the obtained 2D-FE nonlinear field solutions of Figs. 3.12 and 3.13, respectively, and to 'freeze' the resulting permeabilities in the nodes of the FE discretization mesh. Then, using these 'frozen permeabilities' and setting to zero the rotor-PM remanent flux density, one can determine the flux-linkage contribution due to the armature-phase currents from a linear field solution through 2D-FE simulation.

The first linear field solution by FE simulation is used to calculate the *d*-axis inductance L_d. Accordingly, the magnitude of the armature-current vector can be chosen as I_R, so that for aligning the current vector with the *d*-axis, the instantaneous stator-phase currents have to be

$$i_a = I_R, \quad i_b = i_c = -\frac{i_a}{2} = -\frac{I_R}{2} \tag{3.51}$$

thus leading to

$$i_d = I_R, \quad i_q = 0 \tag{3.52}$$

The saturated *d*-axis inductance can be first calculated as

$$L_{d0} = \frac{\psi_d}{i_d} \tag{3.53}$$

where the armature flux-linkage vector component ψ_d is determined from the flux linkages of stator phases *a*, *b* and *c* by Park-transformation. In its turn, the *a*-phase flux linkage, for instance, is calculated as a sum of the flux linkages of all *a*-phase coils. In a 2-D FE field solution, the flux linkage of each individual coil (being equal to the line integral of the magnetic vector potential along the contour of the coil) is proportional to the difference between the average potentials A_z in the FE-discretized field domains occupied by the coil sides located in two different pole regions. The *a*-phase flux linkage is then

$$\psi_a = p\sum_{k=1}^{Q}\psi_{coil,k} = p\sum_{k=1}^{Q}\frac{1}{S}\left(\int_{S_1} A_z dS - \int_{S_2} A_z dS\right)N_c l_a \tag{3.54}$$

where Q denotes the number of coil sides per phase in one pole region, p, the number of pole pairs, N_c , the number of turns of each coil, l_a, the axial length of the stator core and S, the cross-section of the coil region; subscripts 1 and 2 denote the coil sides located in the two different pole regions.

The inductance L_{do} defined by Eq.(3.53) only takes into account the flux linkage in the stator-core field region. The 2-D FE simulation cannot estimate the end-turn leakage inductance. Usually, it is calculated using the empirical formula [9]

$$L_{end} = \frac{2N_{ph}^2}{p}\left(\frac{l_{avg}}{2} - l_a\right)\psi_{end} \tag{3.55}$$

where N_{ph} represents the number of series turns per phase, l_{avg}, the average length of one turn of the armature winding and ψ_{end}, the end-turn flux-linkage. The saturated *d*-axis inductance is then obtained as

$$L_d = L_{d0} + L_{end} \tag{3.56}$$

The saturated *q*-axis inductance is calculated in a similar way, but the armature-current vector needs to be aligned with the *q*-axis, in this case. The stator-phase currents are then

$$i_a = 0,\ i_b = -i_c = \frac{\sqrt{3}I_R}{2} \tag{3.57}$$

which in turn gives

$$i_d = 0,\ i_q = I_R \tag{3.58}$$

The saturated *q*-axis inductance is primarily estimated as

$$L_{q0} = \frac{\psi_q}{i_q} \tag{3.59}$$

where the armature flux-linkage vector component γ_q is determined from the flux linkages of stator phases *a*, *b* and *c* by Park-transformation. The saturated *q*-axis inductance is finally calculated as

$$L_q \mid L_{q0} \; 2 \; L_{end} \tag{3.60}$$

The variation of saturated *d*- and *q*-axis inductances with the armature-stator current is shown in Fig.3.15 for both single- and double-layer IPMSMs under several load conditions. It can be observed, that the *d*-axis inductance is almost constant throughout the stator-current range, whereas the *q*-axis inductance changes notably with stator-current magnitude due to saturation of *q*-axis magnetic path.

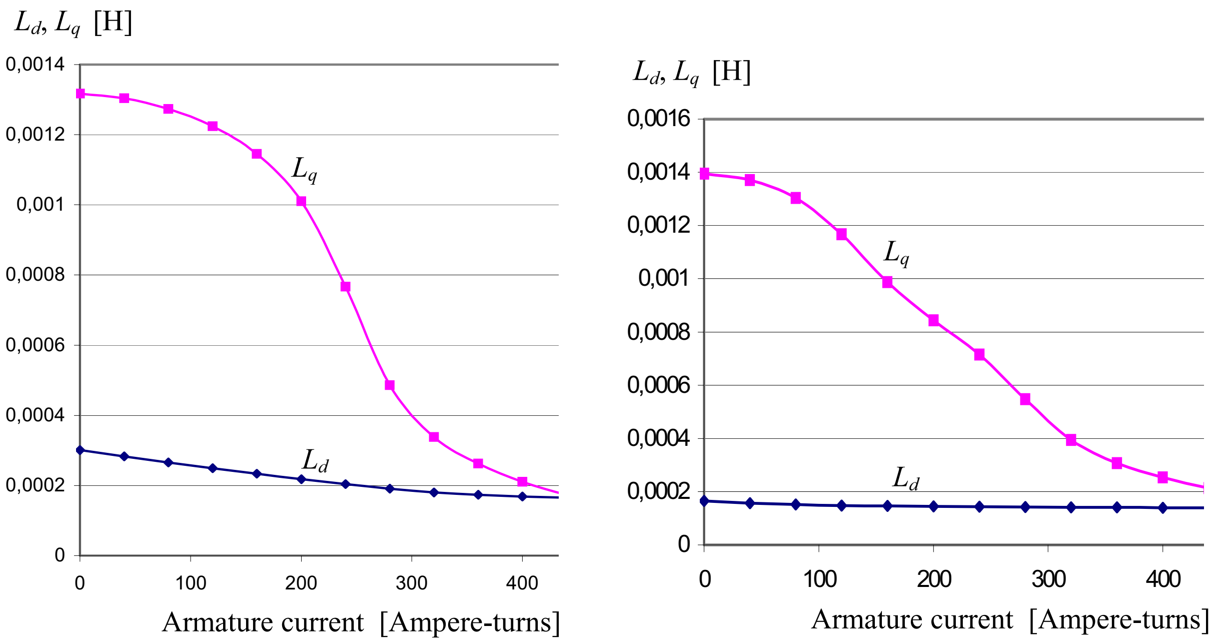

(a) **(b)**

Fig.3.15. Variation of *d*- and *q*-axis inductances with armature-stator current for (*a*) single-layer IPMSM and (*b*) double-layer IPMSM.

3.2. Analysis of the electromagnetic torque

The total instantaneous electromagnetic torque of an IPMSM emphasizes two components: a constant (or average) torque and a pulsating torque.

In an IPMSM, the resultant rotating field under load condition is determined by both the rotor permanent magnetization and the stator-armature currents, and has a space fundamental component, which travels at synchronous speed, and is responsible for the production of the *average electromagnetic torque*. The open-circuit flux-density high-order space harmonics produced by the rotor magnetization also travel at synchronous speed, but their contribution to the average electromagnetic torque is null, because their polarity is different to that of the fundamental space harmonic of the stator-armature mmf, which is the only one of the stator harmonics that rotates at synchronous speed. As regards its average electromagnetic torque, the IPMSM benefits from a hybrid torque-producing mechanism, thus combining the *PM* *alignment* (or *mutual*) *torque component*, resulting from the interaction between PM-rotor flux distribution and armature-stator mmf, with the *reluctance torque component*, which results from the interaction between the armature-stator mmf and rotor reluctance (saliency) variation.

If the IPMSM armature back-emf and current waveforms are both perfectly sinusoidal, a smooth electromagnetic torque is produced. Sinusoidal back-emf waveforms require that armature-stator winding be sinusoidally distributed around the airgap and/or the radial magnetic flux-density amplitude generated by the rotor magnets vary sinusoidally along the airgap. Sinusoidal armature-phase currents are developed using a current-regulated inverter that requires individual phase-current sensors and a high-resolution rotor-position sensor to maintain precise synchronization of the armature energization waveforms with the rotor angular position at every time instant. Any source of non-ideal properties, which causes either the phase currents or the back-emf waveforms to diverge from their purely sinusoidal shapes will give rise to undesired *pulsating torque component*. This harmonic torque component is the sum of

- *cogging* (or *detent*) *torque*, generated by the interaction of the PM-rotor magnetic flux and the angular variation in stator reluctance; armature energization is not involved in cogging torque production;
- *torque ripple*, generated by the interaction of stator-current mmf with either the angular variation in rotor reluctance or the non-sinusoidal waveform of the back-emf.

The analysis of the IPMSM electromagnetic torque is accomplished in this chapter by using the 2D FE field solution in the motor cross-section and integrating the Maxwell stress tensor on a circular path (of radius r) surrounding the rotor in the airgap:

$$T_e = \frac{l_a}{\sigma_0}\int_0^{2\phi} r^2 B_r B_\chi d\chi \tag{3.61}$$

where B_r, B_d are the radial and tangential components of the airgap flux density, respectively, and l_a denotes the active axial length of the motor. If in the FE simulation, first-order triangular elements are used, satisfactory accuracy is achieved for the magnetic vector potential A_z, but the flux-density solution is less accurate, since it is obtained by differentiating the trial functions of A_z. Hence, some errors can arise in the tangential components of flux density in elements adjacent to an interface between materials of different permeabilities. A method of improving the accuracy of the Maxwell stress-tensor integration for IPMSM electromagnetic torque computation [12, 13] consisting in the direct derivation of the flux-density components from an analytical solution of the airgap magnetic field equation, has been incorporated in the Flux-2D software package.

From the 2D-FE field solution in the cross-section of both single- and double-layer IPMSMs under rated-load condition (Figs.3.12 and 3.13), the electromagnetic torque has been calculated through Eq.(3.61) over one rotor-pole angular span (Fig. 3.16). The estimated rms value of the electromagnetic torque is 80.16 Nm for the single-layer IPMSM and 83.1 Nm for the double-layer IPMSM, respectively. As can be seen in Fig. 3.16, torque pulsations are slightly higher for the single-layer IPMSM.

The influence of the armature-current magnitude on the total electromagnetic torque has been also analyzed, and is shown in Fig.3.17. It is remarkable that for both single- and double-layer IPMSMs, increasing values of current in the stator-armature winding yield proportionally increasing torque pulsations.

The 2D-FE field solution of both single- and double-layer IPMSMs under rated-load condition, which allows the electromagnetic torque calculation, can also be used for computation of the equivalent ‘on-load’ cogging torque by ‘freezing’ the permeabilities in each element of the discretization mesh, setting the stator-armature currents to zero, and then applying Eq.(3.61). Hence, Fig.3.18 shows the cogging torque computed over one rotor-pole angular span for both single- and double-layer IPMSMs. It can be observed that the double-layer IPMSM yields a notably smaller ‘on-load’ cogging torque.

By reducing the stator slot-openings, the cogging torque will decrease, as shown in Fig.3.19 for single-layer IPMSM.

A practical method for IPMSM cogging torque mitigation is by skewing either the stator or the rotor [14-16].

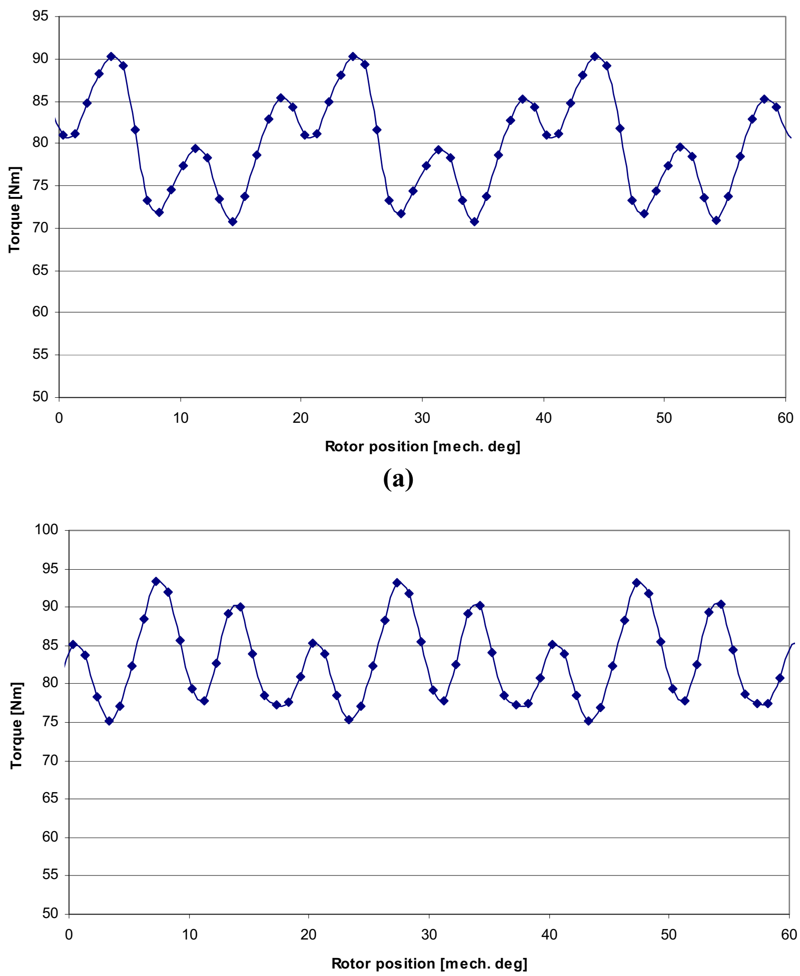

(b)

Fig.3.16. Computed electromagnetic torque vs. rotor position for (*a*) single-layer IPMSM and (*b*) double-layer IPMSM under rated-load condition: $I=169A$ and $ɔ=atan(-i_d/i_q)=62$ *el. deg*.

Skewing of the stator complicates its manufacturing process, especially the automatic insertion of the armature winding. Skewing the rotor magnets continually is difficult, and thus a stepping skew over one slot-pitch of the magnets is used. Rotor-PMs are thus segmented along the stack, and the segments are shifted to cancel certain harmonic components of the cogging torque. By applying the step skew, the cogging torque equation can be written as:

$$T_{cog} = \sum_{n=1}^{N_{step}} \sum_{k=1}^{\infty} T_{ck} \left\{ \cos k \cdot N_{ss} \left(\chi + (n - 1) \frac{2\phi}{N_{ss} \cdot N_{steps}} \right) \right\} \tag{3.62}$$

where N_{steps} is the number of steps in the magnet along the stack length. The shift angle between the various segments of the magnets is:

$$\chi_{step\_skew} = \frac{360}{N_{ss}} \tag{3.63}$$

Fig 3.17.shows an example of rotor skews in 4 steps. To obtain a skew corresponding to one slot pitch, each part must be twisted by the angular skew step:

$$\div\chi_{step\_skew} = \frac{\chi_{step\_skew}}{N_{steps}} \tag{3.64}$$

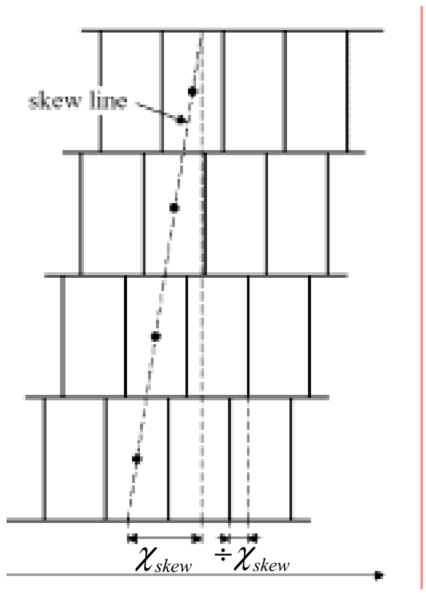

Fig.3.17 Step skew of PM motor by one slot pitch (Shown for 4 steps skew; N_{steps}=4)

The computed electromagnetic torque under rated-load condition for both single- and double-layer IPMSMs designed with a six-step skewed PM-rotor (the angular step skew $\div\chi_{step\_skew}=1.11^0$) is plotted in Fig.3.21, and compared with the torque obtained from the same FE simulation but without rotor skewing. The gain in torque smoothness by IPMSM rotor skewing is noticeable.

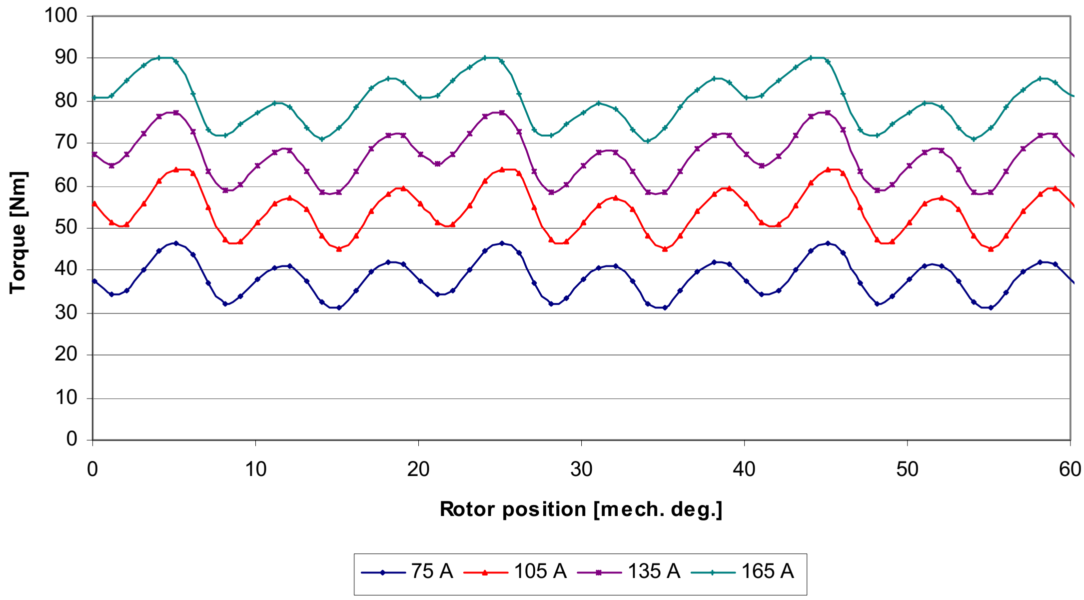

(a)

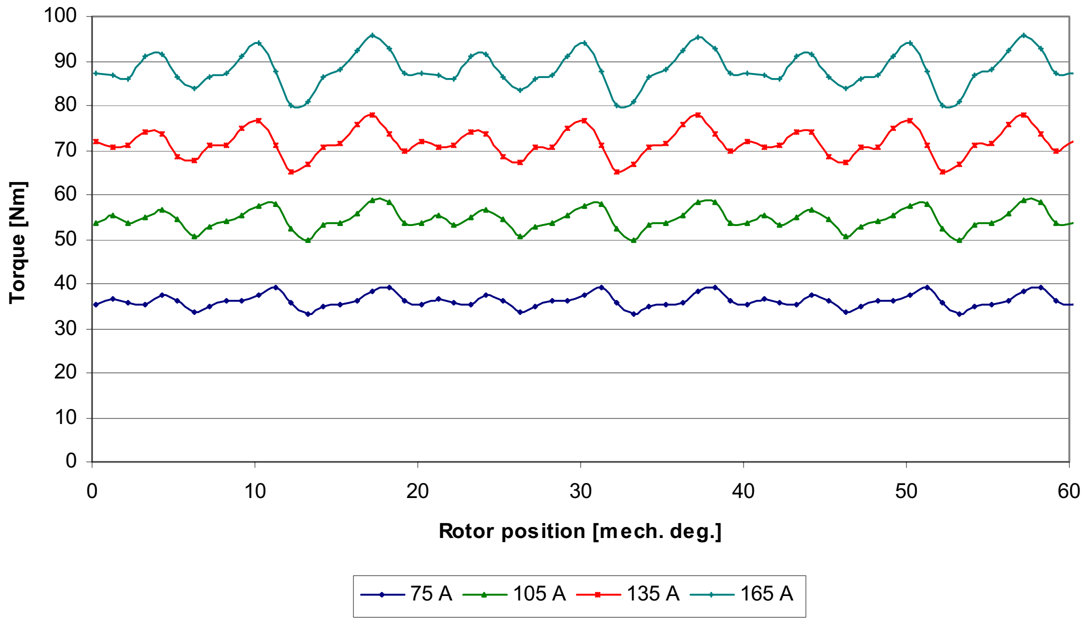

(b)

Fig.3.18. Computed electromagnetic torque of (*a*) single-layer IPMSM and (*b*) double-layer IPMSM for different armature-current values, where *ɔ = 36, ɔ = 49, ɔ = 57* and *ɔ = 62 el. deg.*(*ɔ=atan(*$-i_d/i_q$*)*)

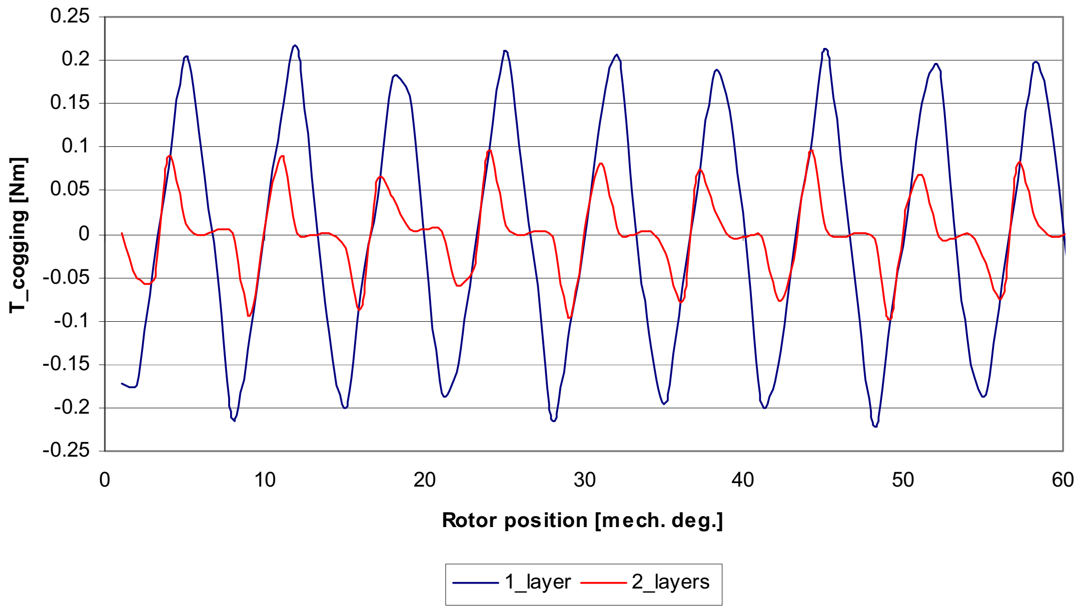

Fig.3.19. Computed cogging torque of (*a*) single-layer IPMSM and (*b*) double-layer IPMSM under rated-load condition.

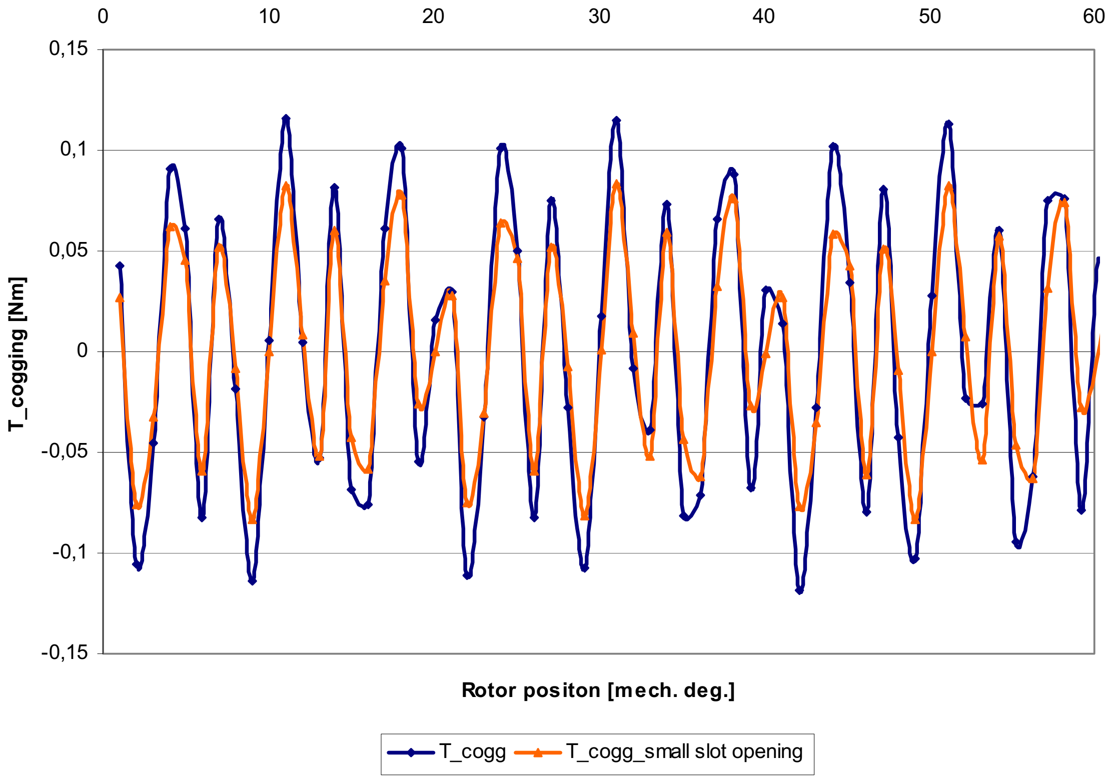

Fig.3.20. Computed cogging torque of single-layer IPMSM with normal and reduced stator slot-openings.

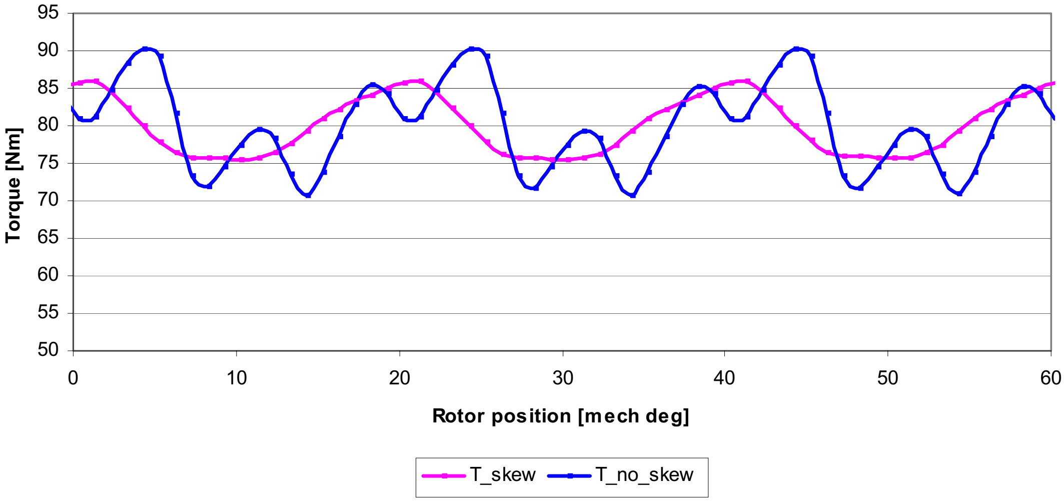

(a)

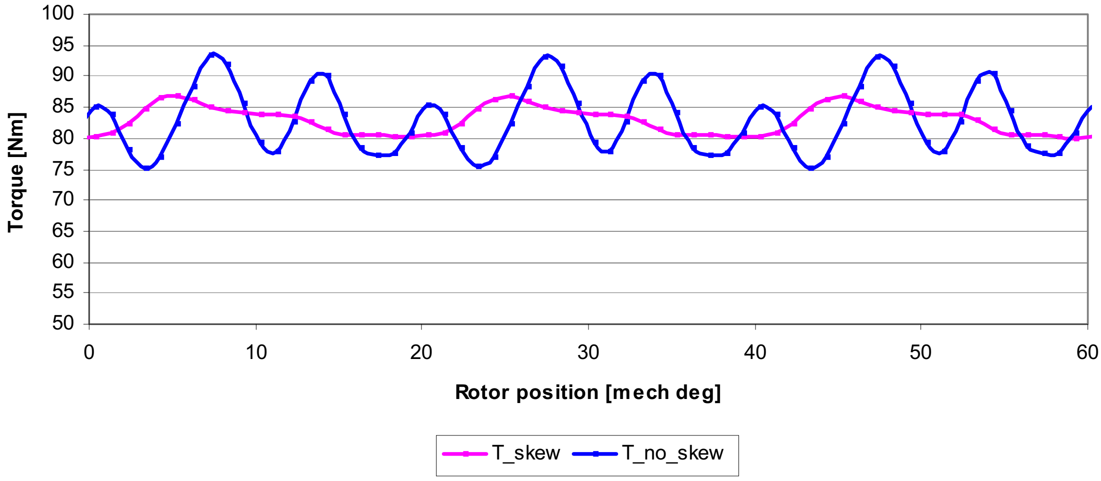

(b)

Fig.3.21. Computed electromagnetic torque for (*a*) single-layer IPMSM and (*b*) double-layer IPMSM with and without rotor skewing, under rated-load condition: $I=169A$ and $\text{ɔ}=atan(-i_d/i_q)=62\,el.\,deg.$

3.3. Conclusions

In the first part of this chapter, an equivalent magnetic circuit-based analysis of a double-layer IPMSM is developed allowing the estimation of the rotor-PM sizes as well as the rated values of PM-rotor and armature-stator fluxes, back-emfs and unsaturated dq inductances. Then, a finite-element field analysis of the flux distribution in both single- and double-layer IPMSMs, at no-load and rated-load conditions, was performed, accounting for magnetic saturation in stator and rotor iron parts.

In the second part of the chapter, the electromagnetic torque was analyzed using the 2D FE field solution in the motor cross-section, and integrating the Maxwell stress-tensor with the flux-density components obtained from an analytical solution of the airgap magnetic field equation. Using FE simulations, the electromagnetic torque of both single- and double-layer

IPMSMs under rated-load condition was calculated. Then, pulsating torque components were evaluated and methods to mitigate them for improving the electromagnetic torque quality, such as stator slot-opening reduction and rotor skewing have been studied.

Selected references

1. A. Fratta, A. Vagati and F. Villata, Design criteria of an IPM machine suitable for field- weakened operation. *Proc. Int. Conf. Electr. Mach.,* 1990, Vol.3, pp.1059–1065.

2. J. R. Hendershot Jr., T. J. E. Miller, *Design of Brushless Permanent-Magnet Motors*, Magna Physics Publishing and Clarendon Press, Oxford, 1994.

3. E.C. Lovelace, T.M. Jahns and J.H. Lang, A saturating lumped parameter model for an interior PM synchronous machine. *IEEE Trans. Ind. Applicat*., Vol. 38 (2002), No. 3, pp. 645-650.

4. N. Bianchi and S. Bolognani, Magnetic models of saturated interior permanent magnet motors based on finite element analysis. *Conf. Rec. 33rd IEEE-IAS Annu. Meet.,* Vol. 1, pp. 27–34,1998

5. G. Kang *et al.*, Improved parameter modeling of interior permanent magnet synchronous motor based on finite element analysis. *IEEE Trans. Magn.*, Vol. 36 (2000), No. 4, pp. 1867–1870.

6. B. Stumberger *et al*., Evaluation of saturation and cross-magnetization effects in interior permanent-magnet synchronous motor. *IEEE Trans. Ind. Applicat*., Vol. 39 (2003), No. 5, pp. 1264-1271.

7. L. Chedot and G. Friedrich, A cross-saturation model for interior permanent-magnet synchronous machine. Application to a starter-generator. *Conf. Rec. 39th IEEE-IAS Annu. Meet.*, Vol. 1, pp. 64-70, 2004.

8. *Flux2D – 9. Solving and post-processing.* Cedrat, France, Electrical Engineering, 2005.

9. R. H. Engelmann and W. H. Middendorf*, Handbook of electric motors*. Marcel Dekker, New York, 1995.

10. J.-Y. Lee *et al.,* Determination of parameters considering magnetic nonlinearity in an interior permanent-magnet synchronous motor. *IEEE Trans. Magn.,* Vol. 42 (2006), No. 4, pp.1303–1306.

11. Rukmi Dutta and M. F. Rahman, A comparative analysis of two test methods of measuring *d*- and *q*-axes inductances of interior permanent-magnet machine. *IEEE Trans. Magn.*, Vol. 42 (2006), No. 11, pp.3712–3718.

12 K.-S. Lee *et al*., Coupling finite elements and analytical solution in the airgap of electric machines. *IEEE Trans. Magn.* Vol. 27 (1991), No. 5, pp. 3955–3957.

13. D.M. Ionel *et al*., Assessment of torque components in brushless permanent-magnet machines through numerical analysis of the electromagnetic field. *IEEE Trans. Ind. Applicat*., Vol. 41 (2005), No. 11, pp. 1149-1158.

14. T. Jahns and W. Soong, Pulsating torque minimization techniques for permanent-magnet AC motor drives—A review. *IEEE Trans. Ind. Electron.*, Vol. 43 (1996), No. 2, pp. 321–330.

15. Leila Parsa, L. Hao and H. Toliyat, Optimization of average and cogging torque in 3-phase IPM motor drives. *Conf. Rec. 37th IEEE-IAS Annu. Meet.*, Vol. 1, pp. 417–424, 2002.

16. Y. S. Chen, Z.Q. Zhu and D. Howe, Calculation of *d*- and *q*-axis inductances of PM brushless AC machines accounting for skew. *IEEE Trans. Magn.* Vol. 41 (2005), No. 10, pp. 3940–3942.

17. A. Muntean, M.M. Radulescu, T. Balasoiu, A. Campeanu, M. Ignat, Design and Analysis of Interior Permanent Magnet Synchronous Motor (IPMSM) for Wide-Speed-range-Application, ' *Acta Electrotehnica* (Romania), Vol. 44 (2004), No. 3, pp. 47-50

Chapter 4

TORQUE CONTROL STRATEGIES OF INTERIOR PERMANENT-MAGNET SYNCHRONOUS MOTORS FOR ELECTRIC VEHICLE PROPULSION

The IPMSM electromagnetic torque may be expressed in the *dq* synchronous reference frame attached to the rotor by Eqs. (2.22) and (2.25), which are rewritten here as

$$\begin{aligned} T_e &= \frac{3}{2} p(\psi_d i_q - \psi_q i_d) \\ &= \frac{3}{2} p\left[\Psi_{PM} i_q + (L_d - L_q(i_q)) i_d i_q\right] \end{aligned} \tag{4.1}$$

It is obvious from Eq.(4.1) that regulation of currents i_d and i_q provides the possibility of *indirectly controlling the electromagnetic torque* developed by the IPMSM [1-6].

Another expression for the IPMSM electromagnetic torque can be obtained in terms of the stator flux-linkage space-vector amplitude $|\underline{\psi}_s|$ and its angle δ with respect to rotor-PM flux-linkage space-vector $\underline{\psi}_{PM}$ (which is aligned to *d*-axis) from Eqs.(2.22) and (2.24):

$$T_e = \frac{3p}{2} \frac{|\underline{\psi}_s| \psi_{PM}}{L_d} \sin\delta + \frac{3p}{4} |\underline{\psi}_s|^2 \left(\frac{1}{L_q(i_q)} - \frac{1}{L_d}\right) \sin 2\delta \, . \tag{4.2}$$

In the above equation (4.2), the torque angle δ is constant for IPMSM steady-state operation, hence stator flux-linkage and PM-rotor flux-linkage space-vectors rotate at synchronous speed; conversely, in transient operation, δ varies, and the two flux-linkage space-vectors rotate at different speeds. It can be identified in Eq.(4.2) the first IPMSM torque component, as the PM-alignment (or mutual) torque and the second one, as the reluctance torque.

Eq.(4.2) emphasizes that the IPMSM electromagnetic torque can be controlled by regulating (through inverter voltages) the amplitude of the stator flux-linkage vector and the torque angle δ, and this is the basis of *direct torque control* of IPMSM [7-15].

By differentiating Eq.(4.2) with respect to time, one obtains:

$$\frac{dT_e}{dt} = \frac{3p}{2} \left(\frac{|\underline{\psi}_s| \psi_{PM}}{L_d} \cos\delta + |\underline{\psi}_s|^2 \left(\frac{1}{L_q(i_q)} - \frac{1}{L_d}\right) \cos 2\delta \right) \frac{d\delta}{dt} . \tag{4.3}$$

As seen from Eq.(4.3), the IPMSM electromagnetic torque can be dynamically controlled by varying the rate of change of the torque angle δ, i.e. the angular speed of the stator flux-linkage space-vector with respect to the PM-rotor flux-linkage space-vector.

4.1. Indirect torque control via stator-current regulation

This section focuses on indirect torque control of current-regulated IPMSMs for EV propulsion applications, i.e. capable of operating over both constant-torque and constant-power flux-weakening regions.

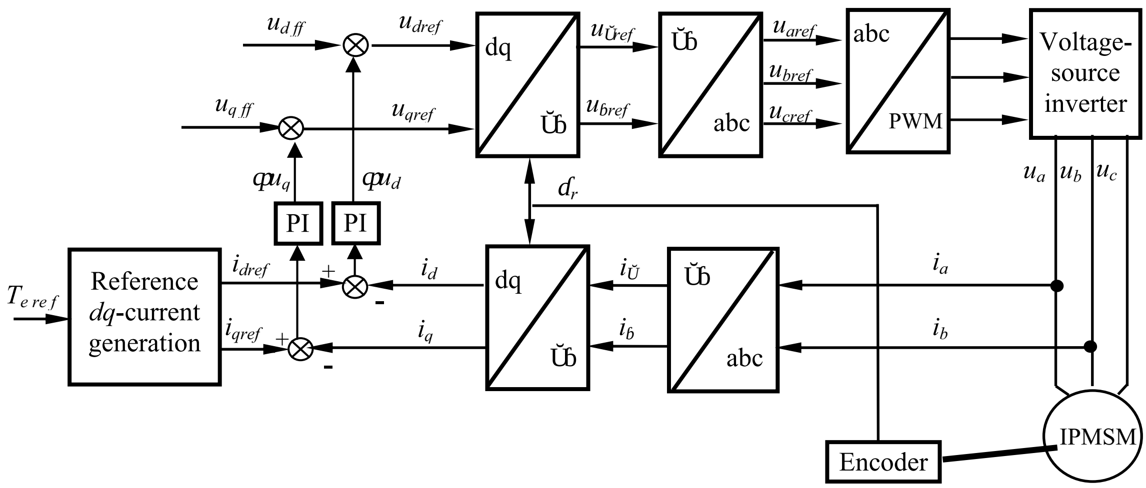

Fig.4.1 Block-diagram of the indirect torque control of IPMSM via stator-current regulation in the rotor reference frame.

As pointed out by Eq.(4.1), for controlling the electromagnetic torque of an IPMSM, it is necessary to regulate both the *d*- and *q*-axis stator-current components, the strict separation between torque- and flux-generating current components being not possible.

The block-diagram of the PWM-current-regulated torque control of IPMSM is shown in Fig.4.1. Stator-armature currents are primarily transformed to the rotor reference frame by using the two-step transformation of Eqs.(2.16) and (2.20). Current regulation is carried out through the compensation of the back-emf voltage component by the feed-forward calculation, supplemented by PI-controller correction to handle the transient case. Hence, the reference voltage vector generated by the *dq*-current regulation consists of two voltage vector terms: (i) one is the steady-state voltage vector identical to the back-emf vector, which achieves the feed-forward decoupling defined by

$$u_{d\,ff} = -\omega L_q i_q \tag{4.4}$$

$$u_{q\,ff} = \omega (L_d i_d + \psi_{PM}) \tag{4.5}$$

(ii) the other one is the dynamic voltage vector, which results from PI-controllers, and decides the transition of the stator-current vector.

The *dq* voltage references are then re-transformed into the IPMSM stator reference frame before having access to the supplying bridge-type inverter. A sine-wave triangular technique is used to generate the PWM commands signals for the IPMSM. Three-phase reference voltages (u_{aref}, u_{bref}, u_{cref}) of variable amplitude and frequency are compared with a common triangular carrier wave of fixed amplitude and frequency. Each comparator output forms the switching-state of the corresponding inverter leg. Since the PWM frequency, equal to the frequency of the carrier wave, is usually much higher than the frequency of the reference voltage, the reference voltage is nearly constant during one PWM period. This approximation is especially true considering the sampled data structure within a digital control system. Depending on the switching states, the positive or negative half DC-bus voltage is applied to each phase. At the modulation stage, the reference voltage is multiplied by the inverse half DC-bus voltage compensating the final inverter amplification of the switching logic into real power supply.

With such an indirect torque control strategy, the IPMSM can operate, below base speed, in the constant-torque region by the maximum torque-to-armature current ratio, and can also operate in the constant-power flux-weakening region within the stator current and voltage constraints, above the base speed. For both IPMSM operating modes, the 'reference *dq*-current generation' block in Fig.4.1 (in which reference currents i_{dref}, i_{qref} are obtained from the torque reference T_{ref}) is described in the following sections.

Reference *dq*-current generation in constant-torque region

In the speed range from standstill up to the base rotor speed ω_b, IPMSM is in constant-torque operating mode, hence the *dq* stator-armature current space-vector can be controlled to produce maximum torque-to-armature current ratio. From Eq.(4.1), this control trajectory yields the relationship between stator-current components i_d and i_q :

$$i_d = \frac{\psi_{PM}}{2\cdot(L_q(i_q) - L_d)} - \sqrt{\frac{\psi_{PM}^2}{4\cdot(L_q(i_q) - L_d)^2} + i_q^2}\,. \tag{4.6}$$

The elimination of i_d between Eqs.(4.1) and (4.6) leads to a fourth-order equation for i_q:

$$i_q^4 + \left(\frac{\frac{2T_e}{3p}\,\psi_{PM}}{(L_q(i_q) - L_d)^2} \right) i_q - \frac{\frac{4T_e^2}{9p^2}}{(L_q(i_q) - L_d)^2} = 0\,. \tag{4.7}$$

By considering, in Eq.(4.7), several values of the electromagnetic torque from 0 to T_{eM} (defined by Eq.(2.32)) as reference torque values $T_e = T_{eref}$, one obtains, after iterations due to $L_q(i_q)$ nonlinearity accounting for iron saturation, the solutions of Eq.(4.7), from which only the real positive ones are retained, and assigned as reference values $i_q = i_{qref}$ corresponding to T_{eref} preset values for IPMSM indirect torque control in constant-torque region. Finally, in order to prevent stator-armature overcurrents, the *d*-axis reference current can be simply adopted as

$$i_{dref} = \sqrt{I_M^2 - i_{qref}^2}\,. \tag{4.8}$$

with I_M defined by the equality limit in the stator-current constraint (2.28), which is dominant for constant-torque operating mode of IPMSM. The (i_{dref}, i_{qref}) pairs of reference *dq*-current values are thus calculated off-line, using Eqs.(4.7)-(4.8), for several reference torque values

$T_e = T_{eref}$ from 0 to T_{eM}, and stored in a look-up table to be used (by interpolation) as 'reference *dq*-current generation' in the indirect torque control scheme of IPMSM (Fig.4.1).

Reference *dq*-current generation in flux-weakening constant-power region

At rotor speeds higher than the base speed ω_b, IPMSM is running in flux-weakening constant-power operation mode, in which the motor torque capability is limited by both armature current and terminal voltage constraints of Eqs.(2.28) and (2.29), and is also strongly affected by the increasing iron losses.

In this region of IPMSM operation, the (i_{dref}, i_{qref}) pairs of reference *dq*-current values in Fig.4.1 are replaced by (i_{odref}, i_{oqref}), calculated off-line and stored in a look-up table, for torque reference values T_{eref}, from Eqs. (2.36)-(2.39), which are re-written here as

$$T_{eref} = \frac{3}{2} p \left[\Psi_{PM} i_{oqref} + (L_d - L_q(i_{oqref})) i_{odref} i_{oqref} \right] \tag{4.9}$$

$$i_{odref} = \frac{\Psi_{PM} L_d - \sqrt{(\Psi_{PM} L_d)^2 + (L_q^2(i_{oqref}) - L_d^2)\left(\Psi_{PM}^2 + L_q^2(i_{oqref}) I_M^2 - \left(\frac{U_{oM}}{\omega}\right)^2\right)}}{(L_q^2(i_{oqref}) - L_d^2)} \tag{4.10}$$

$$U_{oM} = U_M - (R + R_c) I_M, \tag{4.11}$$

$$\sqrt{i_{odref}^2 + i_{oqref}^2} = I_M \tag{4.12}$$

in view of their use (by interpolation) in the 'reference *dq*-current generation' block of Fig.4.1.

4.2. Hysteresis-based direct torque and stator-flux control

The idea of combining the advantages of direct torque and stator-flux control (DTFC) and IPMSM into a highly dynamic drive appeared in the literature two decades ago [7]. More recently, the DTFC has been proposed for wide-speed operation of IPMSMs in EV drives [8, 12-15]. In principle, the IPMSM DTFC involves the direct and independent control of the stator flux-linkage magnitude and the electromagnetic torque by selecting proper voltage switching vectors of the voltage-source inverter supplying the motor. This selection is made to restrict the errors between the references of stator flux-linkage magnitude and electromagnetic torque and their actual (estimated) values. The advantages of the IPMSM DTFC over conventional current-control schemes include the elimination of current controller, coordinate transformation and PWM signal generator, the lesser dependence on motor parameters as well as the fast torque response in steady-state and transient operating conditions.

Principle of hysteresis-based DTFC of IPMSM

As shown by Eq. (4.2), for a constant level of the stator flux-linkage, the IPMSM electromagnetic torque can be changed by modifying the torque angle δ, defined as the angle between the stator flux-linkage vector $\underline{\psi}_s$ and rotor-PM flux-linkage vector $\underline{\psi}_{PM}$ (Fig.4.2).

A three-phase two-level voltage-source inverter (VSI) is used to generate eight voltage vectors which are shown in Fig.4.2, six active vectors (V_1 – V_6) and two zero vectors (V_0 and V_7). The stator flux-linkage vector can be calculated as

$$\underline{\psi}_s = \int_0^t (\underline{u}_s - R\,\underline{i}_s)dt + \underline{\psi}_{s|t=0}, \tag{4.13}$$

where $\underline{u}_s$ defines the stator voltage space-vector, $\underline{i}_s$, the stator current space-vector, R, the stator resistance, and $\underline{\psi}_{s|t=0}$, the initial value of the stator flux-linkage space-vector. Since the initial value of the stator flux linkage $\underline{\psi}_{s|t=0}$ for IPMSM differs from zero, and depends on the rotor position, the initial rotor position has to be measured or estimated.

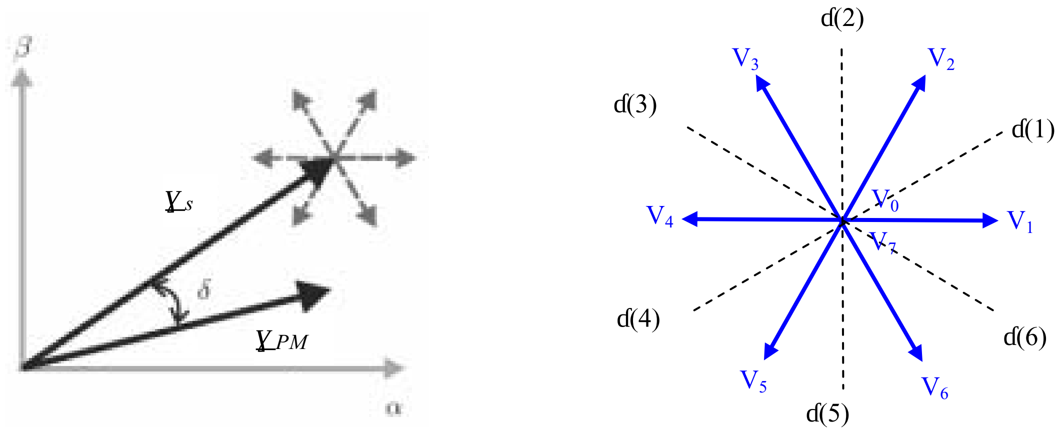

Fig.4.2. Control of stator-flux vector amplitude and torque angle δ in a stationary (α,β) reference frame with VSI voltage vectors.

When in Eq (4.13) the stator resistance is neglected, the variation of the stator flux-linkage vector for a switch-on time T_s of the voltage vector u_s, is expressed as

$$\Delta\underline{\psi}_s \approx \underline{u}_s T_s . \tag{4.14}$$

Each of the six possible active voltage vectors has components orthogonally- and tangentially-oriented to the stator flux-linkage vector. From Eq (4.14), it follows that the orthogonal component of a voltage vector changes the amplitude of the stator flux-linkage, while the tangential component changes the rotation speed of the stator-flux vector and, consequently, the torque angle. Hence, the stator flux-linkage magnitude $|\underline{\psi}_s|$ and the electromagnetic torque T_e can be simultaneously controlled via VSI. The instantaneous error between the reference and estimated values of stator flux-linkage amplitude and electromagnetic torque are minimized by applying the most appropriate voltage vector. Thus, a controller minimizing the error is needed, together with an estimation of the stator flux-linkage and torque. The configuration above represents the "classical" DTFC configuration.

A classical DTFC scheme has two hysteresis comparators, one for the stator flux-linkage amplitude, and another one for the torque. A typical IPMSM DTFC scheme is shown in Fig.4.3, the quantities T_{ref} and $|\underline{Y}_{sref}|$ defining the reference values. The instantaneous error for the stator flux linkage e_q has two possible values (1 and ī 1), whereas the instantaneous torque error e_T has three (ī 1, 0 and 1). Furthermore, the (Ŭb) plane is divided in six sectors (sextants), each of 60 electrical degrees. The errors e_Y and e_T, together with the sector number containing the stator flux vector serve as input for a switching table. The selection of one switching vector depends on the signs of these two errors without inspection of their magnitude values with respect to the sampling time and level of the applied stator voltage. The output of the switching table is one of the eight possible voltage vectors. Furthermore a first-order filter is proposed as quasi-integrator to solve the problem of initial flux estimation.

Simplified switching-table DTFC is implemented in [9] with only non-zero voltage vectors used to control the motor. This essentially reduces the three-valued comparator for the torque error to a normal hysteresis comparator.

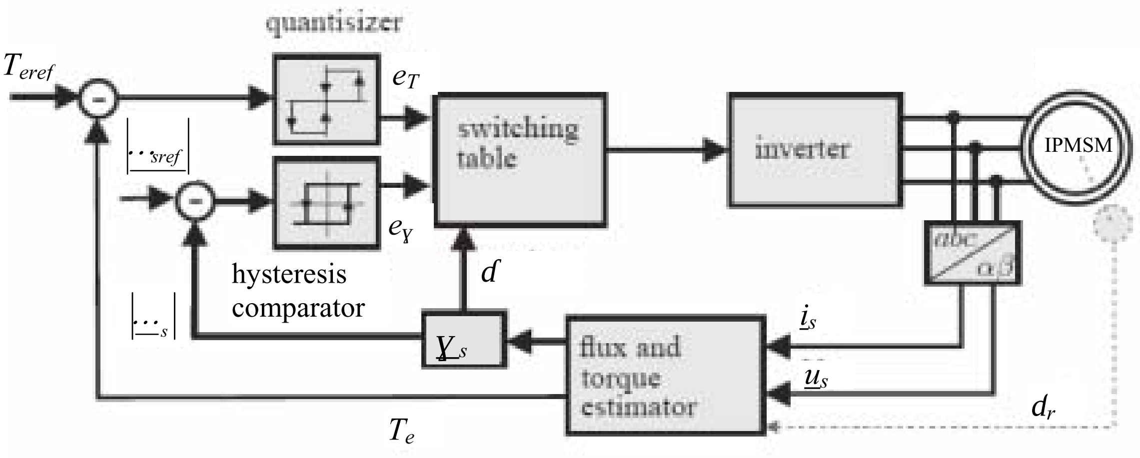

Fig.4.3. Block-diagram of the hysteresis-based DTFC of IPMSM.

The reference for the stator flux-linkage magnitude is obtained from the maximum torque-to-stator current ratio algorithm in the constant-torque region, and applying the flux-weakening condition for the constant-power region. Off-line calculations are needed to determine the look-up tables for the reference stator-flux magnitude.

Problems associated with the hysteresis-based DTFC of IPMSM

Effect of measurement offsets

Offsets in measurements of the DC-link voltage and currents are inevitable. These are inherent in the sensors and the signal conditioning circuits used. These offsets are DC signals and their magnitudes also depend on temperature. The integration process in (4.13) must be regularly reset to reduce the effect of the offset error. Compensation techniques of this offset have been reported [10].

To compensate the offset errors, generally a programmable cascaded low-pass filter (LPF) is proposed as an alternative to the integrator. The transfer characteristic of an LPF is :

$$\frac{X}{Y} = \frac{1}{1 + j\vartheta_f \varpi_s}, \tag{4.15}$$

where ϑ_f represents the filter time constant and ϖ_s is the frequency of the signal. The phase lag λ_f and the gain of the filter K_f can be written as

$$\lambda_f = \tan^{-1}(\vartheta_f \varpi_s) \tag{4.16}$$

$$K_f = \frac{1}{\sqrt{1 + (\vartheta_f \varpi_s)^2}} \tag{4.17}$$

If n number of filter are cascaded, the total phase lag λ_T and the gain K_T are calculated as

$$\lambda_T = \lambda_{f1} + \lambda_{f2} + \ldots + \lambda_{fn} = \tan^{-1}(\vartheta_{f1}\varpi_{s1}) + \tan^{-1}(\vartheta_{f2}\varpi_{s2}) + \ldots + \tan^{-1}(\vartheta_{fn}\varpi_{sn}) \tag{4.18}$$

$$K_T = K_{f1} K_{f2} \ldots K_{fn} \tag{4.19}$$

If all filters are identical, having the same time-constant ϑ_f and the same gain K_f, the expression for the total phase lag λ_T and the gain K_T can be written as

$$\lambda_T = n\lambda_f = n\tan^{-1}(\vartheta_f \varpi_s) \tag{4.20}$$

$$K_T = nK_f^{\,n} = \frac{1}{(\sqrt{1 + (\vartheta_f \varpi_s)^2})^n}. \tag{4.21}$$

If a programmable cascade LPF is used as an integrator for a sinusoidal signal two conditions must be satisfied:

$$\lambda_T = 90^0 \tag{4.22}$$

$$GK_T = \frac{1}{\varpi_s}, \tag{4.23}$$

where G is the gain needed for compensation. Substituting (4.18) and (4.19) into (4.20) and (4.21) yields

$$\vartheta_f = \frac{\tan\left(\frac{90^0}{n}\right)}{\varpi_s} \tag{4.24}$$

$$G = \frac{\left(\sqrt{1 + (\vartheta_f \varpi_s)^2}\right)^n}{\varpi_s}. \tag{4.25}$$

Eqs (4.24) and (4.25) give the parameters ϑ_f and G as functions of frequency, or the rotor speed, at a steady speed. If the signal has a DC offset, the filter can always perform the task of integration by programming τ and G. When the signal is DC, τ and G become infinite and the filter can not perform the integration. For software implementation, the transfer characteristic of the filter must be written in discrete form as

$$\frac{X}{Y} = \frac{1}{1 + \vartheta_f \dfrac{1 - z^{-1}}{T_s}} = \frac{T_s}{T_s + \vartheta_f (1 - z^{-1})}, \tag{4.26}$$

where T_s is the sampling time and τ is the filter time constant. The corresponding difference equation is:

$$y(kT_s) = \frac{1}{T_s + \vartheta_f}\left[T_s x(kT_s) + \vartheta_f y(kT_s - T_s)\right] \tag{4.27}$$

For the stage programmable cascade LPF, the block-diagram is presented in Fig.4.4. If n LPFs are connected as in Fig.4.7, n is equal to 3 and τ and G can be accordingly determined.

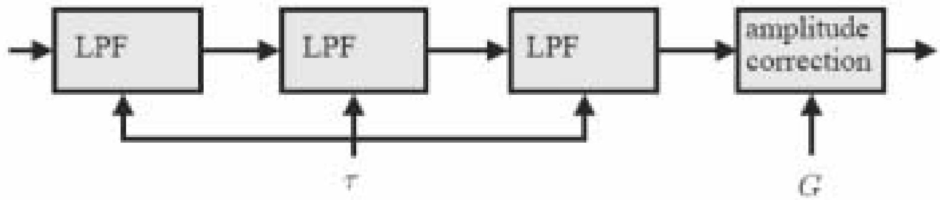

Fig.4.4. Block-diagram of a three-stage programmable LPF.

Effect of the stator-resistance variation

From Eq (4.13) it can be seen that the stator resistance is the only parameter used for stator flux-linkage estimation. The value of the stator resistance changes due to the change in temperature and during the operation of the machine because of the stator copper and other machine losses. The copper losses which are dominant are related to the stator current. The variation of the stator resistance is a thermal process, and therefore a function of time. The stator resistance may change by about 1.5–1.7 times of its nominal value. The drive system may become unstable if the stator resistance value used in the stator flux-linkage estimation differs from that of the actual machine resistance.

Performance of the DTFC drive can be enhanced if the stator resistance is continuously estimated and updated in the controller during operation of machine. If an error in stator resistance between the controller and the motor is present, there will be errors in the estimated flux linkage and torque. The estimated torque is larger than the actual torque when the actual stator resistance is larger than the resistance in the controller and vice versa. This will reduce the maximum output torque of the drive. The amplitude of the stator current varies with the stator resistance variation. Because the stator current is measured, it is possible to use the stator current to track the change in stator resistance. A PI stator-resistance estimator based on the relationship between change of resistance and change of current is proposed in [10]:

$$\Delta R = \left(k_p + \frac{k_i}{s}\right)\Delta I . \tag{4.28}$$

The error of the amplitude of the current vector and that of the reference current vector is used to compensate the change in stator resistance until the error in current becomes zero. The reference current vector can be derived from the reference torque and reference stator-flux. The amplitude of the stator current is calculated according to

$$I_{ref} = \sqrt{i_d^{\,2} + i_q^{\,2}} , \tag{4.29}$$

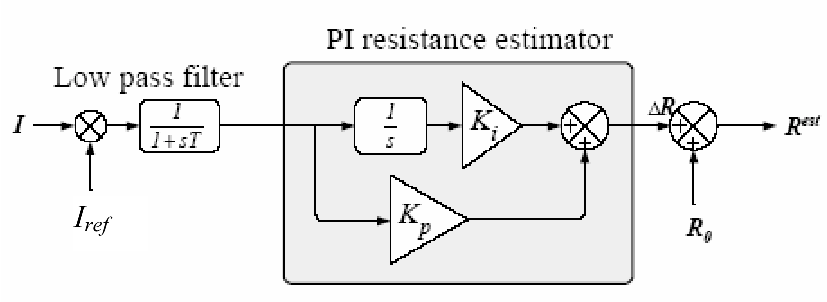

Fig.4.5. Block-diagram of a PI stator-resistance estimator.

where i_d and i_q represent the solution of the system:

$$\begin{cases} T_{eref} = \dfrac{3}{2} p(\psi_{PM} i_q + (L_d - L_q) i_d i_q \\ \psi_{sref} = \sqrt{(L_d i_d + \psi_{PM})^2 + (L_q i_q)^2} \end{cases} \tag{4.30}$$

with T_{eref} and ψ_{sref} denoting the torque reference and the stator-flux magnitude reference, respectively. It is evident that solution of Eq.(4.30) is independent of the stator resistance.

For real-time application, a look-up table of reference current at different reference stator flux-linkage and torque values can be formed to save the execution time. The variation of the stator resistance will not affect this look-up table. Therefore, it is possible to use it to compensate for any resistance variation. The equations are written in the rotor frame, but the amplitude of the current vector is independent of reference frame. Therefore, rotor position is not necessary for this PI resistance estimator.

Effect of the forward voltage drop of power switches

The voltage drop of the power switches may cause oscillation in the stator flux and torque of IPMSM [11]. Generally, it is assumed that no voltage drop on power switch and diode and no time delay occur. However, forward voltage drop is inevitable in every power electronic circuit. In order to examine the error in the voltage vector caused by neglecting the forward voltage drop, the switching mode of the inverter with different voltage vector and polarity of current is examined. In Fig.4.6 the actual voltage with positive and negative current is shown. Ideally, the output voltage is either zero or U_{dc}. When the upper IGBT is on, the lower IGBT must be off. The switching delay and dead time are neglected. As the upper IGBT is on, the current can flow either into the load through the upper IGBT, or from the load through the upper diode into the DC source. The output voltage will be $U_{dc} - U_{CE}$ and $-U_{df}$, instead of U_{dc} and 0, when the current is positive. It is seen that when the current is positive, the waveform is shifted down. Therefore, the actual voltage of the output terminal is lower than the assumed voltage. When the current is negative (flows from the load), the actual voltage will be shifted up, and will be bigger than the assumed voltage. From the ideal situation, the difference is caused by the forward voltage drop.

The forward voltage drop of a power switch (IGBT and diode) can be found with the saturation voltage characteristics and output characteristics in the datasheet of the power electronic device. Although the forward characteristic of the IGBT is nonlinear, it can be approximated as

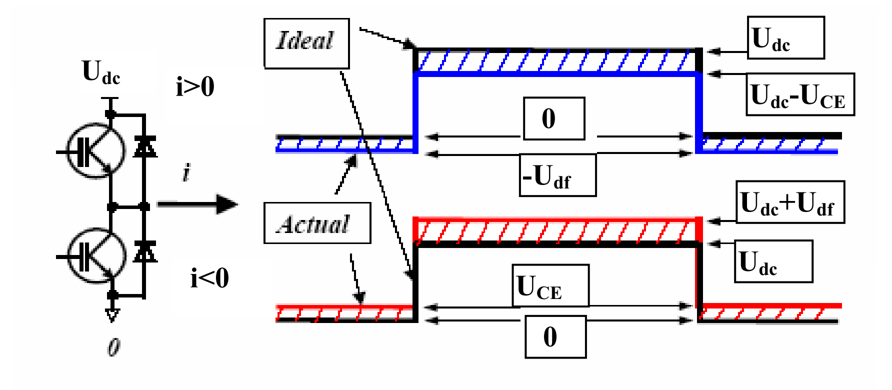

`

Fig.4.6. The output voltage at positive and negative current.

$$U_{CE} \approx U_{CE(0)} + r_C \cdot I_C , \tag{4.31}$$

where the resistance r_C can be assumed as an extra stator resistance, and can be evaluated by the stator resistance estimator.

With the assumptions that

- the sampling frequency is so high that the current is pure sinusoidal;
- the forward voltage-drop of diode and IGBT are the same, i.e.

$$U_{CE} = U_{df} = \Delta U \tag{4.32}$$

The effect of the voltage drop at different current polarities is shown in Fig.4.7. The stator voltage components in the fixed reference frame ($\alpha\beta$) can be obtained from the phase voltages as

$$\begin{aligned} u_\alpha &= \frac{2}{3}\left(U_A - \frac{1}{2}(U_B + U_C)\right) \\ u_\beta &= \frac{1}{\sqrt{3}}(U_B - U_C) \end{aligned} \tag{4.33}$$

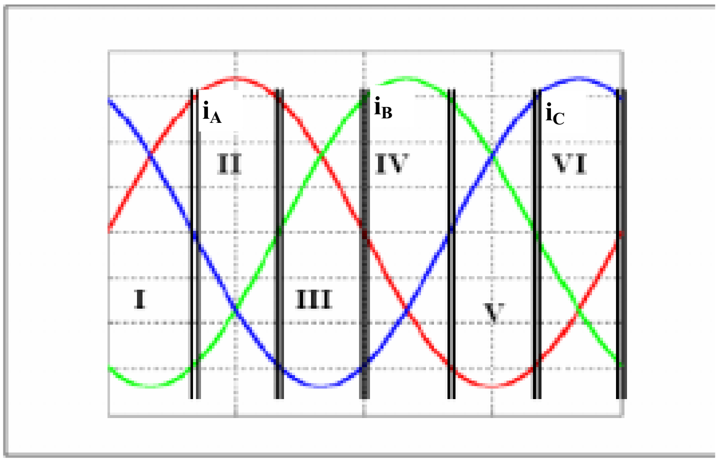

Fig.4.7. Six sectors with different current polarities.

Considering the effect of the forward voltage drop in the first sector, the *uŬ uƃ* voltage components are written as

$$u_{\zeta}{}^{I} \,|\, \frac{2}{3}\Big(U_A\, 4 \div U\, 4\, \frac{1}{2}/U_B\, 2 \div U\, 2\, U_C\, 4 \div U\Big)$$
$$u_{\eta}{}^{I} \,|\, \frac{1}{\sqrt{3}}\Psi\!U_B\, 2 \div U\, 4\, (U_C\, 4 \div U)\beta \qquad (4.34)$$

The error caused by the forward voltage drop can be seen by subtracting (4.33) from (4.34). The results in other sectors can be obtained in the same way, and the differences of the voltage components for all six sectors are presented in Table 4.1.

Table 4.1. The effect of the forward voltage drop on *uŬ uƃ*

	I	II	III	IV	V	VI
Current polarity	A+B-C+	A+B-C-	A+B+C-	A-B+C-	A-B+C+	A+B-C+
ϕuŬ(1 2 / 3)	-ϕU	-2ϕU	-ϕU	ϕU	2ϕU	ϕU
ϕuƃ(1 1/ $\sqrt{3}$)	2ϕU	0	-2ϕU	-2ϕU	0	2ϕU

If the changes in Ŭand ƃ axis are in the same direction, the amplitude of the flux Eq.(4.9) will also be changed. If the two changes are not in same direction, bigger error in the flux angle estimation will occur.

In [12] a compensation scheme based on look-up table is proposed. The main idea is obtaining the forward voltage drop in real-time and correcting the integration of back-emf, in accordance with the polarities of the three-phase currents. This method does not need any extra hardware.

Hysteresis-based DTFC of IPMSM for EV propulsion

The block-diagram of the DTFC for IPMSM is presented in Fig.4.8. Torque and stator flux-linkage amplitude are controlled using two hysteresis comparators, which operate independently of each other. The outputs of these controllers provide appropriate voltage vectors of the inverter through an optimal switching table.

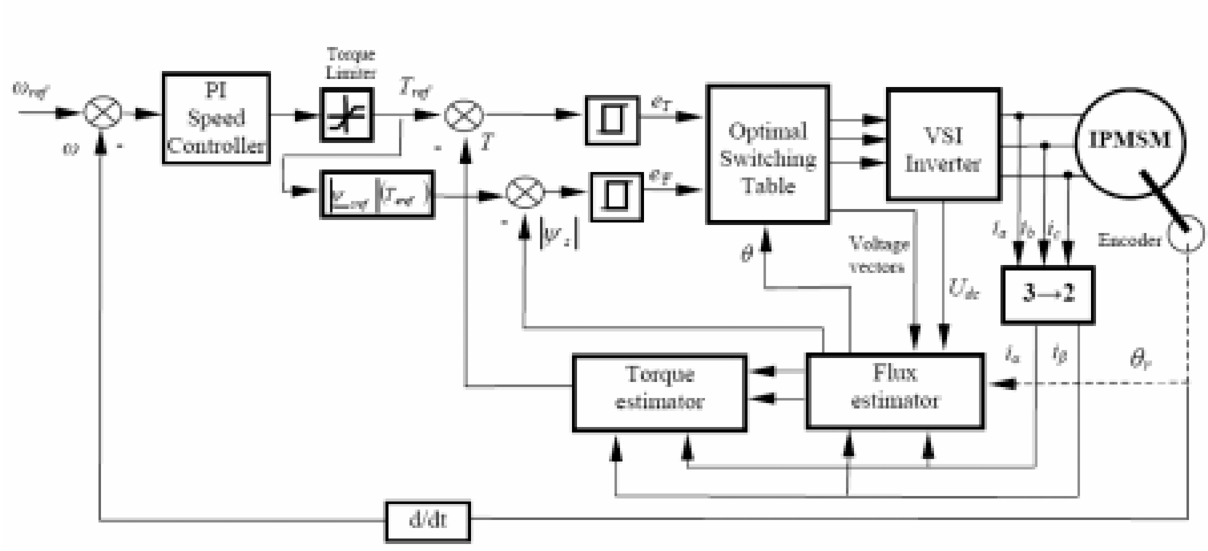

Fig.4.8. Block-diagram of the hysteresis-based DTFC of IPMSM for EV propulsion.

The simplest way to estimate the stator flux-linkage $\underline{\psi}_s$ is from the measured stator voltage and current. The advantage of using this method consists of the less parameter dependence, and except the stator resistance, no others parameters are necessary. The coordinate transformations are not necessary and for the initial position of the stator flux linkage vector, a simple encoder is needed.

From Eq.(4.13), the stator flux-linkage components ψ_α, ψ_β in the stationary reference frame ($\alpha\beta$) can be expressed as

$$\psi_\alpha = \int_0^t (u_\alpha - R \cdot i_\alpha)dt + \psi_{\alpha|t=0} \tag{4.35}$$

$$\psi_\beta = \int_0^t (u_\beta - R \cdot i_\beta)dt + \psi_{\beta|t=0} \tag{4.36}$$

where u_α, u_β are $\alpha\beta$ components of the stator voltage in the stationary reference frame $(\alpha\beta)$, and i_α, i_β, define $\alpha\beta$ components of the stator current. When these stator flux-linkage components are known, the electromagnetic torque T_e can be estimated as

$$T_e = \frac{3}{2} p \cdot (\psi_\alpha i_\beta - \psi_\beta i_\alpha) \tag{4.37}$$

The stator voltage space-vector $\underline{u}_s$, expressed in *$(\alpha\beta)$* reference frame, can be obtained by using the switching states of the VSI and the DC-link voltage U_{dc} :

$$\underline{u}_s(S_a,S_b,S_c) = \frac{2}{3}U_{dc}(S_a + S_b e^{j\cdot 2\pi/3} + S_c e^{j\cdot 4\pi/3}), \tag{4.38}$$

where S_a, S_b, S_c represent commutation functions of inverter legs. The $\alpha\beta$ components of the stator voltage in the stationary reference frame are calculated in Table 4.2 with $U_d = \frac{2}{3}U_{dc}$.

Table 4.2 $\alpha\beta$ components of the stator voltage in the stationary reference frame

	V_1	V_2	V_3	V_4	V_5	V_6	V_7	V_8
u_α	U_d	$0.5\ U_d$	$-0.5\ U_d$	$-\ U_d$	$-0.5\ U_d$	$0.5\ U_d$	0	0
u_β	0	$0.866\ U_d$	$0.866\ U_d$	0	$-\ 0.866 U_d$	$-0.866\ U_d$	0	0

The voltage vector plane is divided into six sectors (sextants) so that each voltage vector divides each region into two equal parts (Fig.4.2). In each sector, four of the six non-zero voltage vectors may be used. Also zero-vectors are allowed. All the possibilities can be tabulated in a switching table.

The torque hysteresis comparator is a three-valued comparator, meaning that its output e_T can take (-1, 0, 1) values, according to the following cases:

- $e_T = -1$ the actual value of the torque is above the reference and out of the hysteresis limit; the torque must be reduced;
- $e_T = 1$ the actual value of the torque is below the reference and out of the hysteresis limit; the torque must be increased;
- $e_T = 0$ the actual value is inside the hysteresis limit.

The flux hysteresis comparator is a two-valued comparator, meaning that its output can take the following values:

- $e_\psi = -1$ the actual value of the flux linkage is above the reference and out of the hysteresis limit; the flux must be reduced;
- $e_\psi = 1$ the actual value of the flux linkage is bellow the reference and out of the hysteresis limit; the flux must be increased.

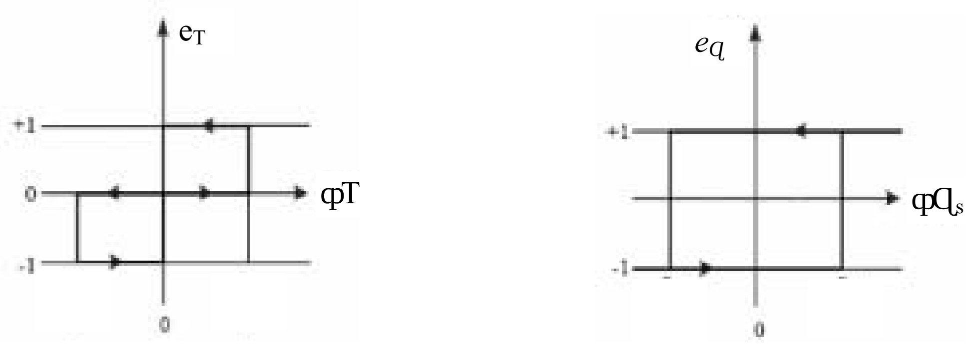

a) **b)**

Fig.4.9. Hysteresis comparators: a) for torque, b) for stator-flux linkage magnitude.

The stator flux-linkage vector is maintained in the hysteresis band by applying the proper voltage vector as presented in Fig.4.10.

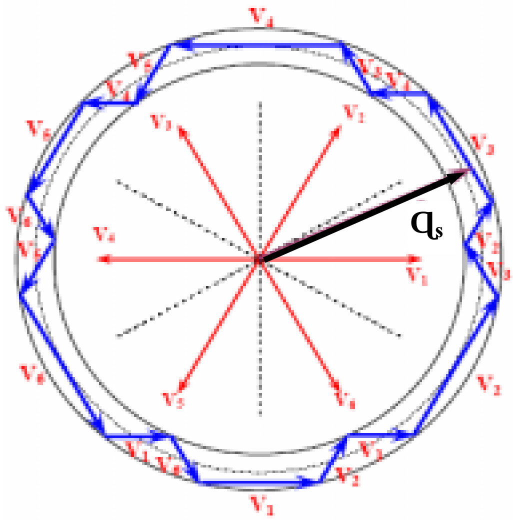

Fig.4.10. Stator flux-linkage vector trajectory by applying the proper voltage vector.

As mentioned before, some authors [9] have proposed a reduced switching table without zero-voltage vectors. They argue that the application of a zero-vector would make the change of torque subject to the rotor mechanical time-constant, which may be rather long compared to the electrical time-constants of the system. This results in a slow change of torque. This reasoning does not make sense, since in the original switching table zero-vectors are used when the torque is inside the hysteresis band, i.e. when the torque is desired to be kept constant. Therefore, the zero-voltage vectors must be precisely used in the switching table, as presented in Table 4.3. Besides, inverter switching losses and torque ripple are notably reduced when using switching table with zero-voltage space-vectors. However, if the torque ripple has to be kept as small as possible, higher commutation frequency must be applied [8].

When the stator voltage $\underline{u}_s$ is small compared to the resistive voltage drop $R\underline{i}_s$, the integration of Eq.(4.13) is not accurate, and thus the estimation of stator flux-linkage will be erroneous. As the electromagnetic torque is calculated from the stator flux-linkage components, it will be also affected. An open-loop integrator will cause initial values and drift problems, especially at low frequencies.

Table 4.3 Switching table for hysteresis-based DTFC of IPMSM

e_Y	e_T	d					
		d(1)	d(2)	d(3)	d(4)	d(5)	d(6)
$e_Y = 1$	$e_T = 1$	V_2(1 1 0)	V_3(0 1 0)	V_4(0 1 1)	V_5(0 0 1)	V_6(1 0 1)	V_1(1 0 0)
	$e_T = 0$	V_0(0 0 0)	V_0(1 1 1)	V_0(0 0 0)	V_0(1 1 1)	V_0(0 0 0)	V_0(1 1 1)
	$e_T = -1$	V_6(1 0 1)	V_1(1 0 0)	V_2(1 1 0)	V_3(0 1 0)	V_4(0 1 1)	V_5(0 0 1)
$e_Y = -1$	$e_T = 1$	V_3(0 1 0)	V_4(0 1 1)	V_5(0 0 1)	V_6(1 0 1)	V_1(1 0 0)	V_2(1 1 0)
	$e_T = 0$	V_0(0 0 0)	V_0(1 1 1)	V_0(0 0 0)	V_0(1 1 1)	V_0(0 0 0)	V_0(1 1 1)
	$e_T = -1$	V_5(0 0 1)	V_6(1 0 1)	V_1(1 0 0)	V_2(1 1 0)	V_3(0 1 0)	V_4(0 1 1)

The estimation of the stator flux linkage vector $\underline{Y}_s$ can be made using the *dq* current model of the IPMSM:

$$|\underline{\psi}_s| = \sqrt{\psi_d^2 + \psi_q^2} \tag{4.39}$$

$$\psi_d = L_d \cdot i_d + \psi_{PM} \tag{4.40}$$

$$\psi_q = L_q(i_q) \cdot i_q \, . \tag{4.41}$$

Reference stator flux-linkage vector generation

Eq.(4.2) reveals that the control of the electromagnetic torque corresponds to the control of the stator flux-linkage vector amplitude and its angle with respect to rotor flux-linkage vector.

There are upper limits of variation for both control quantities, $|\underline{\psi}_s|$ and δ, to achieve stable IPMSM DTFC. Firstly, since according to Eq.(4.2), $T_e = 0$ for $\delta=0$, the condition for positive slope $dT_e/d\delta$ around $\delta = 0$ leads to

$$|\underline{\psi}_s| < \psi_{s\,\lim} = \frac{\psi_{PM}}{1 - L_d / L_q(i_q)} . \tag{4.42}$$

The variation of the electromagnetic torque T_e with respect to δ for different values of the stator flux linkage ψ_s is presented in Fig.4.11. For high values of the reference stator flux-linkage, the derivative of the torque with respect to δ at zero cross is negative and thus the DTFC can not be applied.

Secondly, by differentiating Eq.(4.2) with respect to δ and equating it to zero, the maximum allowable angle δ_{lim} can be found as

$$\delta \leq \delta_{\lim} = \cos^{-1}\left[\frac{\psi_{s\,\lim}/|\underline{\psi}_s| - \sqrt{\left(\psi_{s\,\lim}/|\underline{\psi}_s|\right)^2 + 8}}{4}\right] \tag{4.43}$$

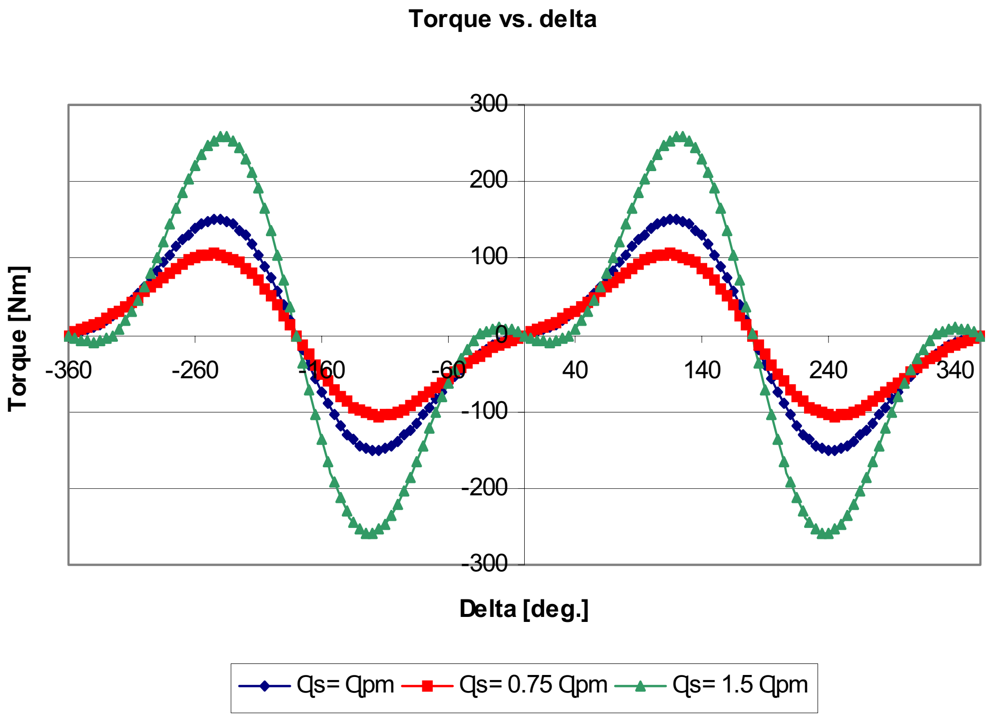

Fig.4.11. Electromagnetic torque vs. torque angle δ, for different stator flux-linkage magnitudes.

In the hysteresis-based DTFC scheme of IPMSM considered in Fig.4.8, the reference electromagnetic torque T_{eref} is obtained as the output of the rotor-speed controller from the outer loop, and is limited at a certain value, which guarantees the stator current not to exceed its maximum admissible value. Based on the DTFC principle, a method to generate the reference stator flux-linkage vector from the reference electromagnetic torque is developed here by maximizing the IPMSM electromagnetic torque over wide-speed operation range in the presence of stator current and voltage constraints.

In the speed range I, from standstill up to the base rotor speed ω_b, the required function $|\underline{\Psi}_{srefI}|(T_{erefI})$ for the reference value of the stator flux-linkage magnitude can be obtained by ensuring the IPMSM constant-torque operation in which the maximum torque-to-stator current ratio is achieved. By considering, in Eq.(4.7), several values of the electromagnetic torque from 0 to T_{eM} (defined by Eq.(2.32)) as reference torque values $T_e = T_{erefI}$, solving Eqs.(4.7) and (4.8) for the stator currents i_{dI} , i_{qI}, and substituting them in Eqs.(4.29)-(4.30), one obtains the function $|\underline{\Psi}_{srefI}|(T_{erefI})$ requested in the hysteresis-based DTC scheme of IPMSM in the constant-torque region.

The IPMSM speed operation range II, above the base rotor speed ω_b, is the flux-weakening constant-power region. The corresponding reference torque T_{erefII} has the expression of Eq.(4.9) with the stator-current components (i_{odref}, i_{oqref}) given by Eqs.(4.10)-(4.12). Eliminating the variables i_{odref} and i_{oqref} between Eqs.(4.9)-(4.12) and

$$\left|\underline{\Psi}_{srefII}\right| = \sqrt{(L_d i_{odref} + \Psi_{PM})^2 + (L_q(i_{oqref}) i_{oqref})^2} \tag{4.44}$$

one obtains the required function $|\Psi_{srefII}|(T_{erefII})$ for the hysteresis-based DTFC scheme of IPMSM in the flux-weakening constant-power region.

Simulation results

Using MATLAB-Simulink software, the proposed hysteresis-based DTFC scheme is simulated for a double-layer IPMSM having the main parameters given in Table 4.4.

Table 4.4 Main parameters of the simulated double-layer IPMSM

Parameter	Symbol	Value	Measure unit
Pole-pair number	p	3	-
Stator phase resistance	R_s	26	mΩ
PM flux linkage magnitude	Ψ_{PM}	0.0782	Vs
q-axis stator inductance (unsaturated)	L_q	1205	μH
d-axis stator inductance	L_d	223	μH
Stator-current limit	I_M	118	A
Stator-voltage limit	U_M	320	V
Base rotor speed	ω_b	2000	rpm

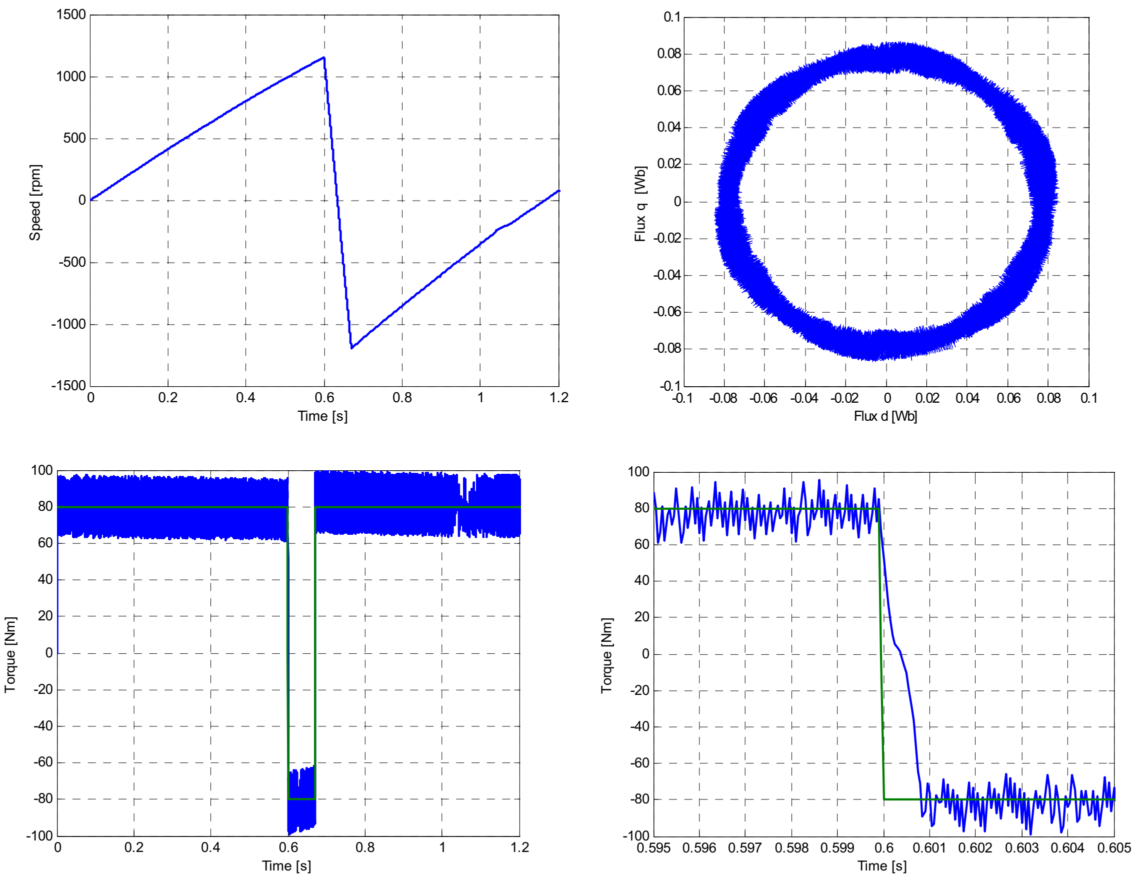

Fig.4.12. Simulations results for hysteresis-based DTFC of double-layer IPMSM subject to T_{eref} step changes from 80 Nm to -80 Nm at t=0.6 s and from - 80 Nm to 80 Nm at t=0.66 s, under open speed-loop, load torque T_L=70 Nm and f=20 kHz.

The hysteresis-based DTFC scheme of Fig.4.8 is first *simulated for open speed-loop*. The stator-flux magnitude estimation is carried out using the current model of Eqs.(4.39)-(4.41). A step in the reference electromagnetic torque is applied with the PM-flux linkage at its nominal value, i.e. the torque reference is initially T_{eref} = 80 Nm and at time instant t=0.6 s, it is abruptly reversed to T_{eref} = - 80 Nm; the reference torque is changed again to its initial positive value at t=0.66 s. The load torque is preset at T_L = 70Nm. For the first simulation the frequency is f=20 kHz, and for the second one, the frequency was changed to f=48 kHz. The simulation results are presented in Figs.4.12 and 4.13. The actual electromagnetic torque is controlled within the hysteresis band, and follows quickly its reference. The dynamic response time is less then 1 ms. The torque change is nonlinear around zero, in accordance with the analysis of Fig.4.11.

In its turn, the stator flux-linkage vector is well controlled, its trajectory being circular in the plane (Ψ_d, Ψ_q). The comparison between Figs.4.12 and 4.13 reveals that the torque ripple and the bandwidth of the stator flux-linkage magnitude become smaller when working at higher DTFC frequency.

Another torque step response simulation is performed, i.e. the reference torque is initially T_{eref} = 110 Nm and at time instant t=0.6 s, it is abruptly reversed to T_{eref} = - 110 Nm; the reference torque is changed again to its initial positive value at t=0.66 s. The load torque is preset at T_L = 70Nm and the DTFC working frequency is f=48 kHz. It can be seen in Fig.4.14 that the torque tracks well the reference, but the response time has slightly increased.

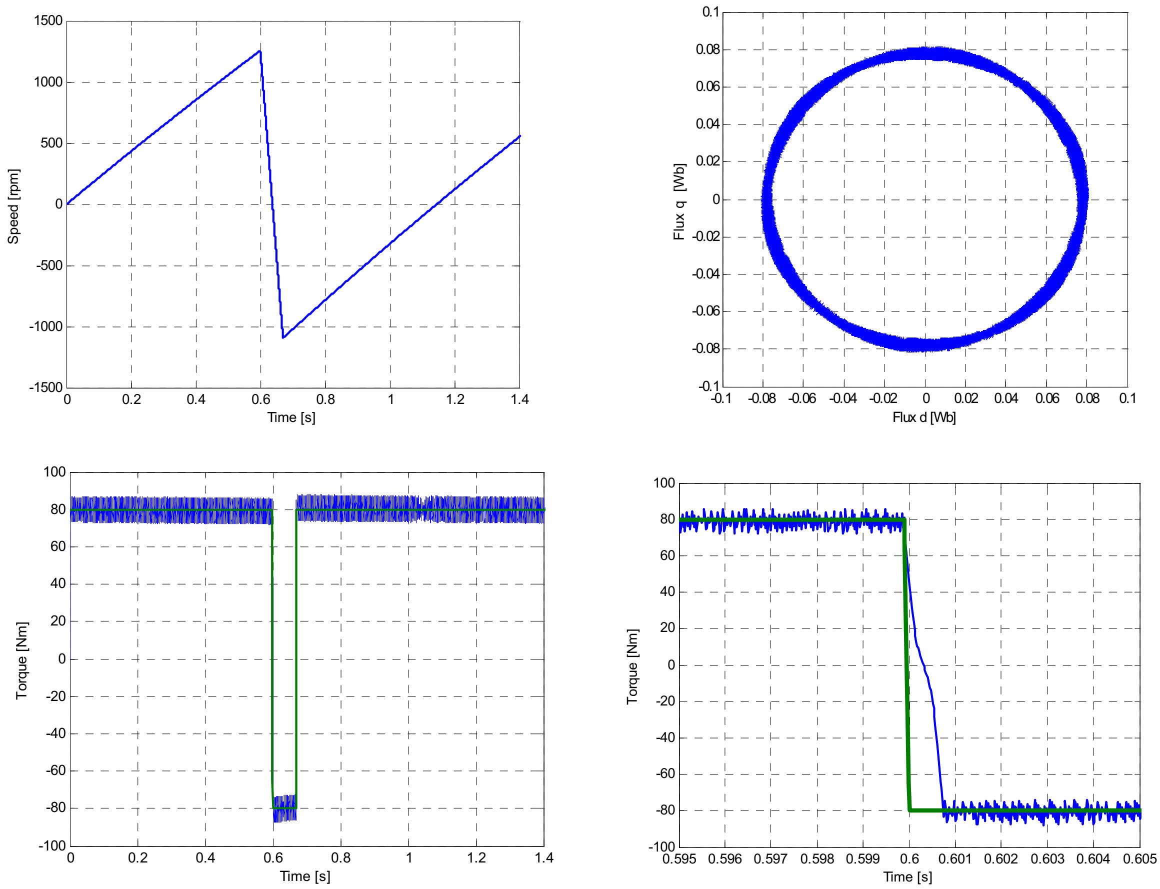

Fig.4.13. Simulation results for hysteresis-based DTFC of double-layer IPMSM subject to T_{eref} step changes from 80 Nm to -80 Nm at t=0.6 s and from - 80 Nm to 80 Nm at t=0.66 s, under open speed-loop, load torque T_L=70 Nm and f=48 kHz.

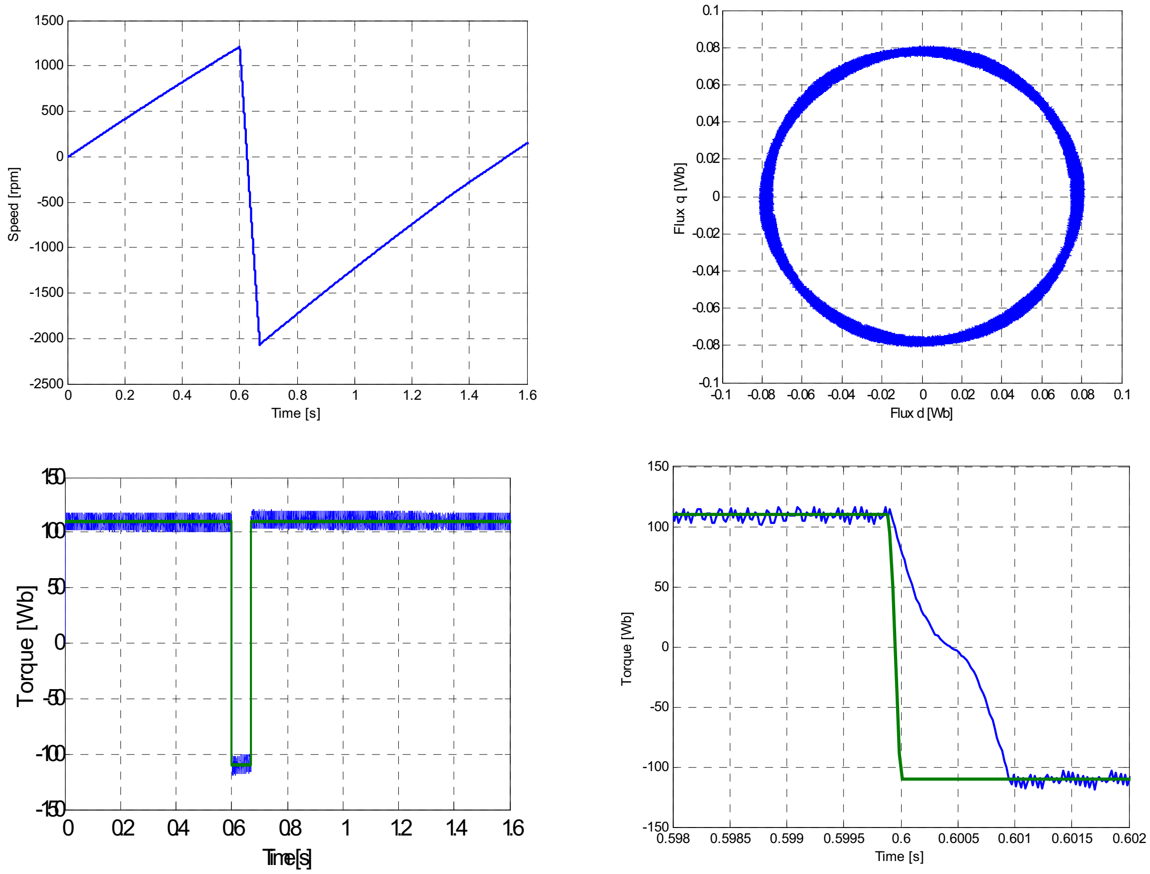

Fig.4.14. Simulation results for hysteresis-based DTFC of double-layer IPMSM subject to T_{eref} step changes from 110 Nm to -110 Nm at t=0.6 s and from - 110 Nm to 110 Nm at t=0.66 s, under open speed-loop, load torque T_L=70 Nm and f=48 kHz.

Closed-loop speed simulations are also carried out to test the IPMSM hysteresis-based DTFC behaviour in the constant-torque and flux-weakening constant-power regions. The reference speed stands for the nominal speed, and when it is reached, the stator current and voltage limits are obtained. The flux-weakening operation mode of IPMSM starts when the speed approaches the reference speed.

For the first simulation (Fig.4.15), the reference speed is set at 2000 rpm. The torque and stator flux-linkage vector magnitude follow closely their references, and a smooth transition between the constant-torque and flux-weakening constant-power operation modes can be observed. The stator flux-linkage vector trajectory in the plane is circular, the bigger radius corresponds to the stator flux-linkage in the constant-torque region, while the smaller radius corresponds to the stator flux-linkage in the flux-weakening operation range. The load torque is preset as T_L=50 Nm.

For the second simulation (Fig.4.16), the reference speed is set at 4000 rpm. It can be seen again that the torque and stator-flux linkage track their references in both constant-torque and flux-weakening constant-power regions.

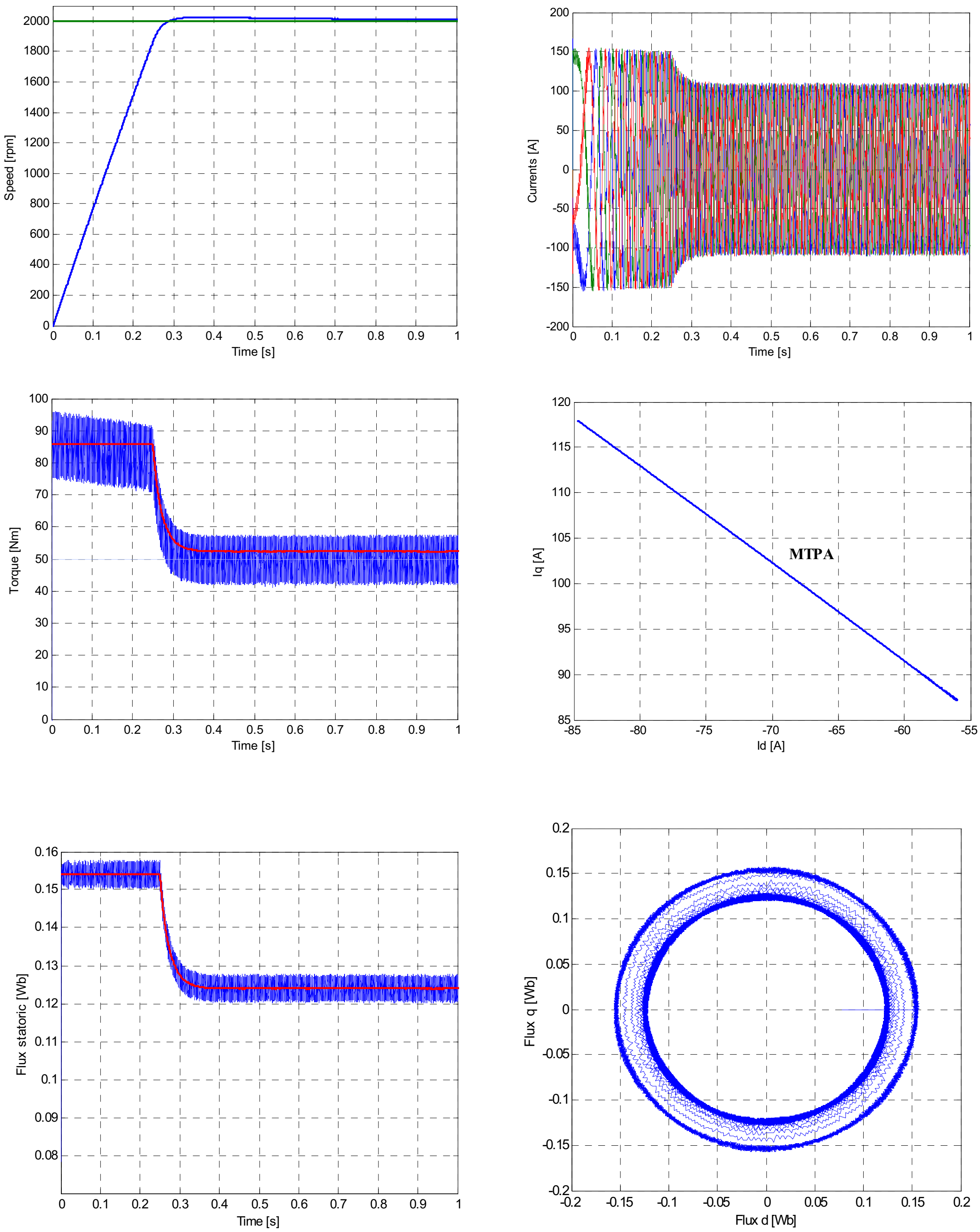

Fig.4.15. Simulation results for hysteresis-based DTFC of double-layer IPMSM under closed-loop speed with n_{ref}=2000 rpm, load torque T_L=50 Nm and f=48 kHz.

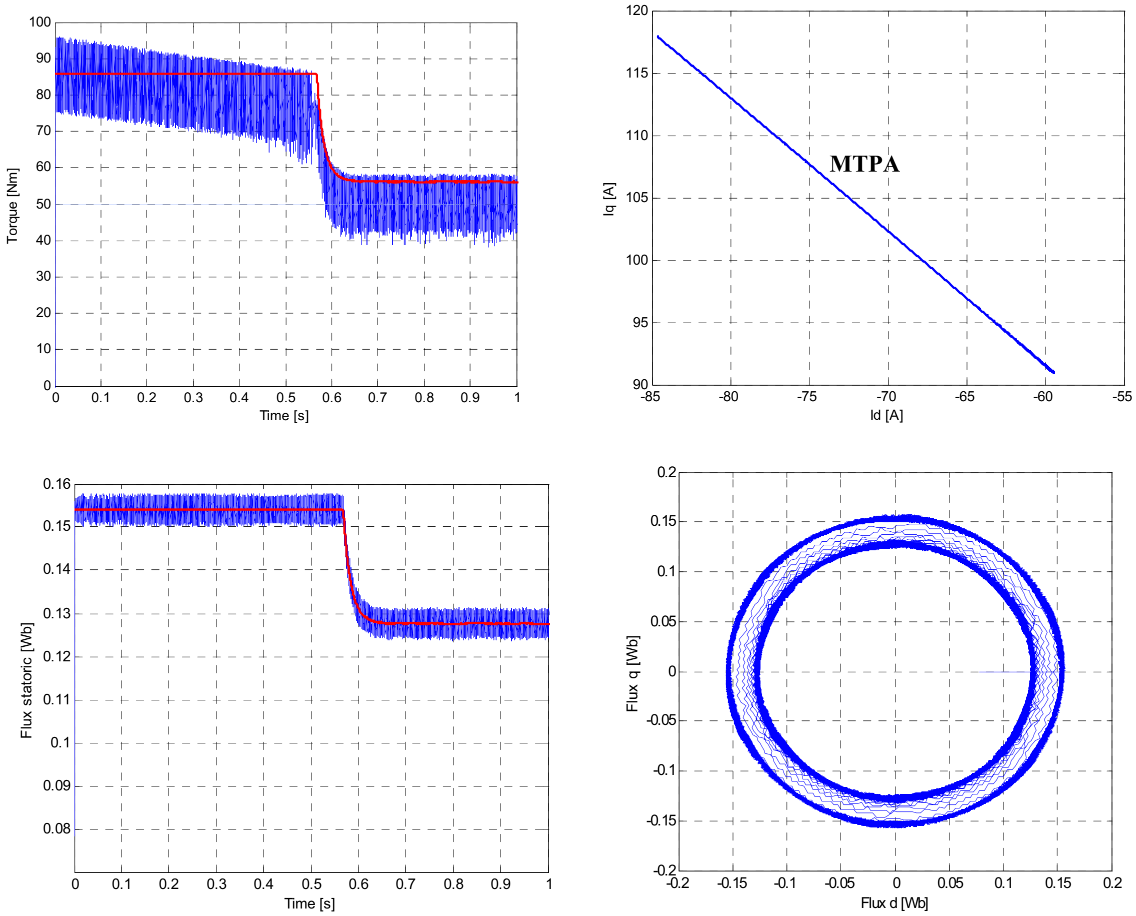

Fig.4.16. Simulation results for hysteresis-based DTFC of double-layer IPMSM under closed-loop speed with n_{ref}=4000 rpm, load torque T_L=50 Nm and f=48 kHz.

4.3. Conclusions

In the first part of this chapter, the indirect torque control of IPMSM via stator-current regulation in the rotor reference frame is presented.

The second part of the chapter deals with the hysteresis-based DTFC of IPMSM. The major problems associated with DTFC schemes for IPMSM are discussed. The offsets in the sensor outputs of the DC-link voltage and stator current can be overcome using a low-pass filter. The stator resistance variation is tracked using a PI-estimator based on the stator current variation. The forward voltage drop on the inverter power switches can be compensated using a properly designed look-up table.

The hysteresis-based DTFC scheme of IPMSM for EV propulsion is detailed and a novel approach for generating the reference stator flux-linkage vector magnitude is proposed to insure IPMSM extended torque-speed envelope with maximum torque-to-stator current ratio operation in the constant-torque region below the base speed as well as constant-power flux-weakening operation with highest available torque in the region above the base speed.

Extensive simulation results to show the effectiveness of the proposed hysteresis-based DTFC scheme of IPMSM over wide-speed operation range are provided.

Selected references

1. B.K. Bose and P.M. Szczesny, A microcomputer-based control and simulation of an advanced IPM synchronous machine drive system for electric vehicle propulsion. *IEEE Trans. Ind. Electron.*, vol. 35 (1988), No. 4, pp. 547–559.

2. S. Morimoto, M. Sanada, and Y. Takeda, Wide-speed operation of interior permanent-magnet synchronous motors with high-performance current regulator. *IEEE Trans. Ind. Applicat.*, Vol. 30 (1994), No.5, pp. 920–926.

3. M.F. Rahman *et al.*, An investigation of direct and indirect torque controllers for PM synchronous motor drives. *Conf. Rec. IEEE-IAS Annu. Meet.*, 1997, pp. 519-523.

4. S. Bosga and H. Zelaya de la Parra, Field-weakening control of an interior permanent-magnet motor for application in electric vehicles. *Proc. Europ. Conf. Power Electron. Applic. – EPE '99*, Lausanne, Switzerland, 1999, CD-ROM, 9 pp.

5. L. Chen *et al.*, Improved control techniques for IPM motor drives on vehicle application. *Conf. Rec. IEEE-IAS Annu. Meet.*, 2002, CD-ROM, 6 pp.

6. M. Meyer and J. Böcker, Optimum control for interior permanent-magnet synchronous motors in constant-torque and flux-weakening range. *Proc. 12th Int. Conf. Power Electron. Motion Contr. Conf. – EPE-PEMC 2006*, Portoroz, Slovenia, 2006 , pp. 282-286.

7. I. Boldea and S.A. Nasar, Torque vector control (VTC) a class of fast and robust torque, speed and position digital controllers for electric drives. *Electr. Mach. Power Syst.*, Vol.15 (1988), pp. 135-148

8. M.F. Rahman, L. Zhong and K.W. Lim, A direct torque-controlled interior permanent-magnet synchronous motor drive incorporating field weakening. *IEEE Trans. Ind. Applicat.*, vol. 34 (1998), No. 6, pp. 1246–1253.

9. L. Zhong *et al.*, Analysis of direct torque control in permanent-magnet synchronous motor drives, *IEEE Trans. Power Electron.*, Vol. 12 (1997), No. 3, pp. 528–536.

10. M.F. Rahman *et al.*, Problems associated with the direct torque control of an interior permanent-magnet synchronous motor drive and their remedies. *IEEE Trans. Ind. Electron.*, vol. 51 (2004), No. 4, pp. 799–809.

11. L. Tang and M. F. Rahman, Compensation of the effects of the forward voltage drop of power switches on direct torque controlled PM synchronous machine drive. *Conf. Rec. IEEE-IAS Annu. Meet.*, 2003, CD-ROM, 6 pp.

12. N. Hoshi *et al.*, Starting torque response of direct torque controlled interior permanent-magnet synchronous motors. *Proc. Europ. Conf. Power Electron. Applic. – EPE 2003*, Toulouse, France, 2003, CD-ROM, 8 pp.

13. J. Habibi and S. Vaez-Zadeh, Efficiency-optimizing direct torque control of permanent magnet synchronous machines. *Proc. IEEE 36th Annu. Power Electron. Spec.Conf. – PESC '05*, Recife, Brazil, 2005, pp. 759-764.

14. Xu Jiaqun, Ouyang Minggao and Tang Renyuan, Study on direct torque control of permanent-magnet synchronous motor in electric vehicle drive. *Proc. Conf. Autom. Motion Contr. - AMC'06*, Istanbul, Turkey, 2006, pp.774-777.

15. Adina Muntean, M.M. Radulescu and A. Miraoui, Wide-speed operation of direct torque-controlled interior permanent-magnet synchronous motors. In: *Recent developments of electrical drives* (Eds. S. Wiak, M. Dems, K. Komeza), Springer, The Netherlands, 2006, Ch. 2, pp. 177-186.

Chapter 5

EXPERIMENTAL STUDY ON THE TORQUE CONTROL OF INTERIOR PERMANENT-MAGNET SYNCHRONOUS MOTORS FOR ELECTRIC VEHICLE PROPULSION APPLICATIONS

In this chapter, the experimental study on the direct (DTFC) and indirect (via stator-current regulation) torque control of a double-layer IPMSM prototype for EV propulsion applications is carried out.

5.1. Experimental set-up

The laboratory experimental set-up has been designed and implemented with the technical support provided by BRUSA Elektronik AG, Sennwald, Switzerland. Its block-diagram, presented in Fig.5.1, comprises

- Double-layer interior permanent-magnet synchronous motor (IPMSM) under experimental study
- Three-phase cage induction motor (IM) used as a mechanical load
- Mechanical coupling between IPMSM and IM
- Voltage-source inverter for IPMSM supplying
- Voltage-source inverter for IM (load) supplying
- Voltage source
- Position sensor for IPMSM and IM (load)
- CAN interface and PC
- Power analyzer.

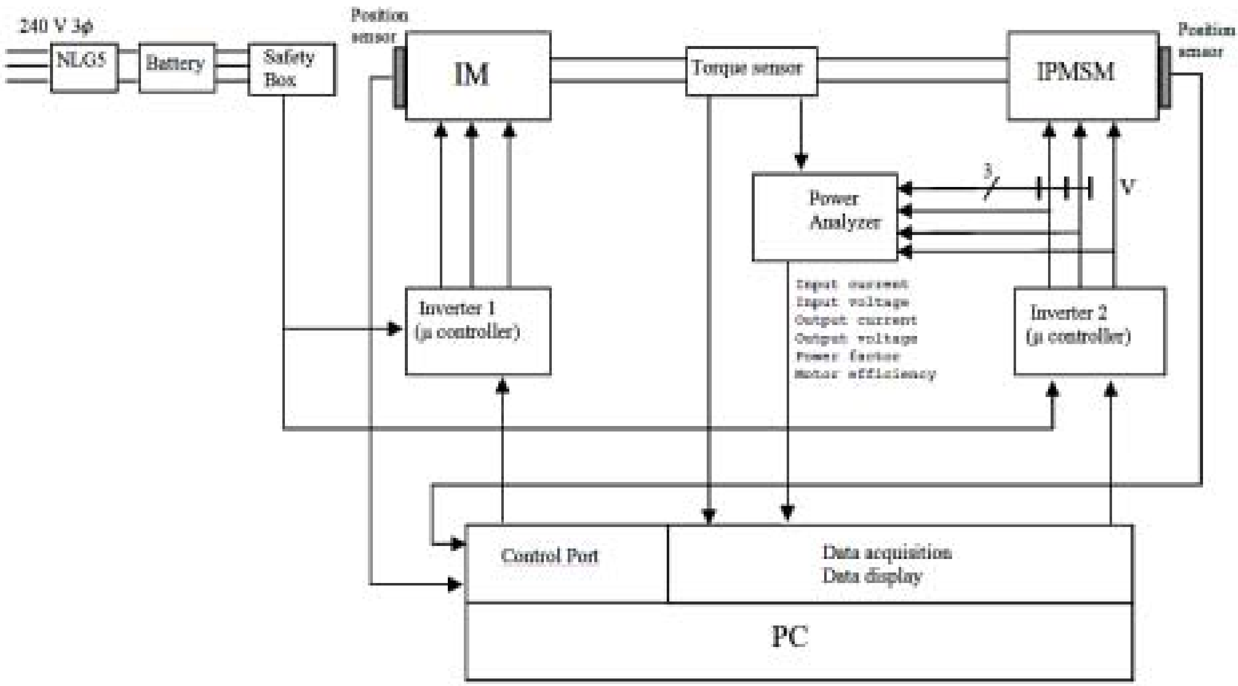

Fig.5.1. Block-diagram of the laboratory experimental set-up for the torque control study of a double-layer IPMSM prototype for EV propulsion applications.

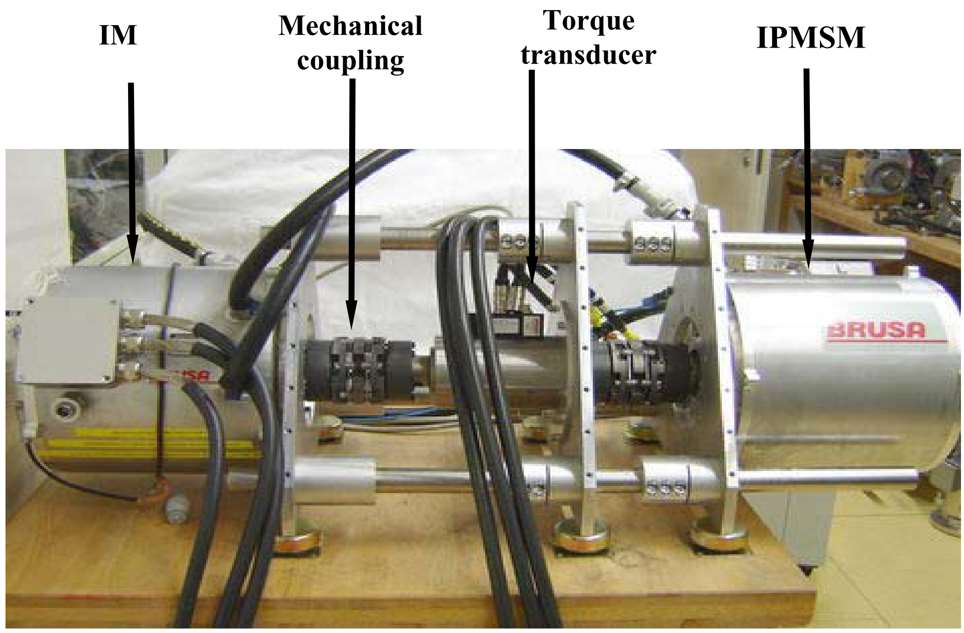

Fig.5.2. Drive bench part of the experimental set-up.

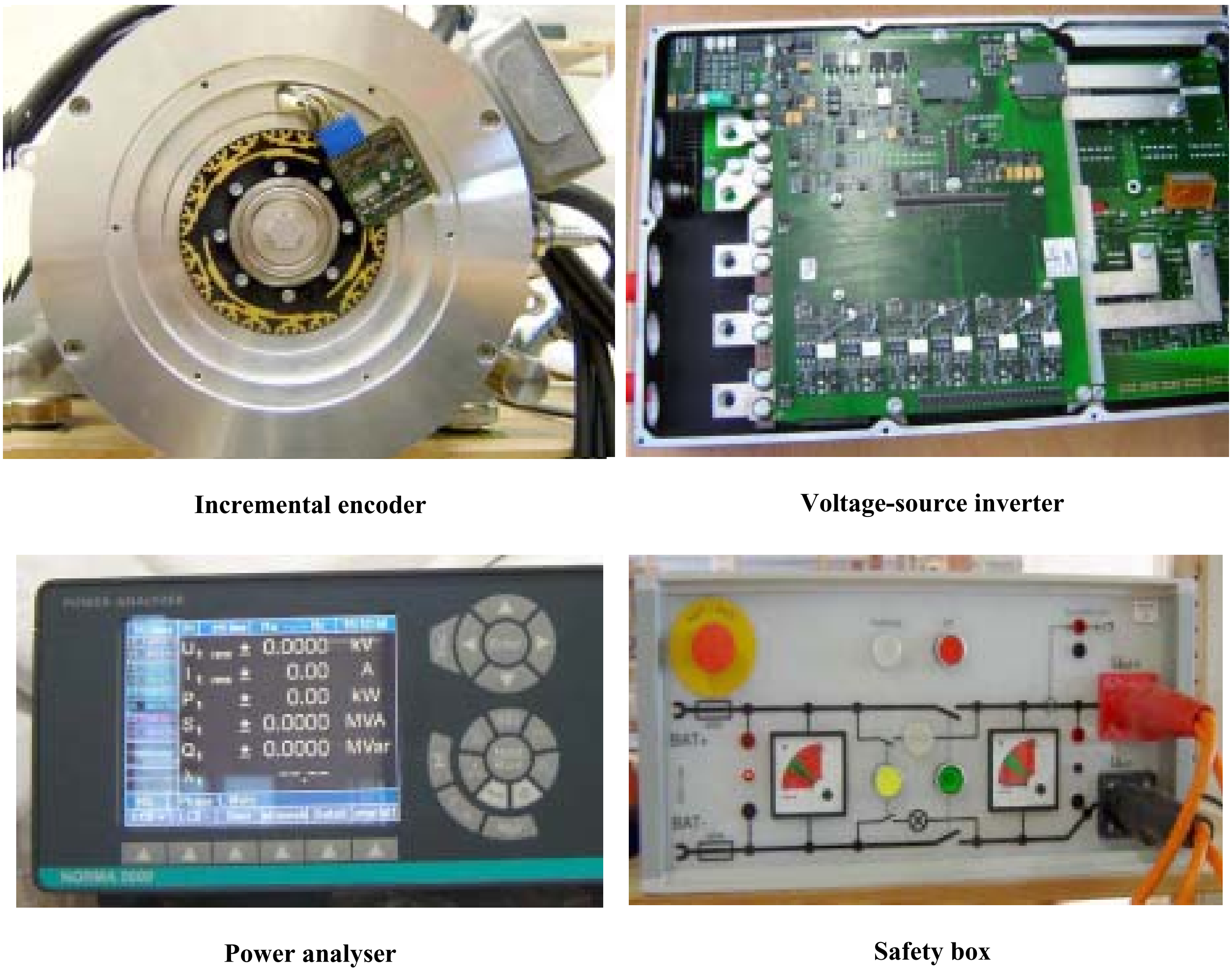

Fig.5.3. Other equipment parts of the experimental set-up.

The drive bench part of the experimental set-up, consisting of the double-layer IPMSM under study, the IM (load), the mechanical coupling between them and the torque transducer, is displayed in Fig. 5.2.
The main parameters of the double-layer IPMSM prototype, which was built based on the design outlined in Chapter 3, are given in Table 5.1. For the IM used as a mechanical load in the drive bench, the specifications are listed in Table 5.2.

Table 5.1. Main parameters of the double-layer IPMSM prototype under experimental study

Parameter	Symbol	Value	Measure unit
Pole-pair number	p	3	-
Stator-phase resistance	R_s	26	mq
PM flux-linkage magnitude	q_{PM}	0.0782	Vs
q-axis stator inductance (unsaturated)	L_q	1205	µH
d-axis stator inductance	L_d	223	µH
Stator current limit	I_{slim}	118	A
Stator voltage limit	U_{slim}	320	V
Base rotor speed	$ɣ_b$	2000	rpm

Table 5. 2. Specifications of the IM used as a mechanical load

Parameter	Symbol	Value	Measure unit
Pole-pair number	p	3	-
Stator-phase resistance	R_s	26	mq
Rated stator-phase current	I	115	A
Voltage	U_{ph}	85.66	V
Frequency	f	100	Hz
Rated power	P	13.6	kW
Base rotor speed	n_b	2000	rpm

Fig. 5.3 illustrates other equipment parts of the experimental set-up. Technical data of the voltage-source bridge-type inverter (VSI) are given in Table 5.3.

Table 5. 3. Technical data sheet of the VSI

Power	**106 kW**
Input DC Voltage (including HV supply voltage)	
Typical Input DC undervoltage shutdown	100V
Minimum Input DC voltage for operation	120V
Minimum Input DC voltage for full current capability	200V
Maximum Input DCvoltage for operation	480V
Typical Input DC overvoltage shutdown	500V
Maximum Input DC surviving voltage	520V
Three Phase AC Output	
Continuous RMS current	225A
Repetitive max. RMS current 30sec 100%, 90sec 50%	300A
Peak RMS current derating vs. Tcoolant>72°C.	-10A/°C
Cont. Power (VDC=75%VDCmax, IAC=IACcont, cos phi=0,9) (note 1)	**80 kW**
Max. Power (VDC=75%VDCmax, IAC=IACmax, cos phi=0,9) (note 1)	**106 kW**
PWM Frequency (symmetrical modulation)	24 kHz
Efficiency (VDC=75%VDCmax, PAC=PACcont, cos phi=0,9) (note 1)	0.97
Mechanical and Environment	
Height	88 mm
Width	240 mm
Length (without connections and cable clamps)	360 mm
Weight (including cooling water)	9.5 kg
Coolant pressure drop @ 6l/min, Tcoolant = 25°C (note 2)	65 hPa
Power dissipation to coolant (IAC = IACcont)	2.4 kW
Operational ambient temperature range	-40...+85°C
protection grade	IP65

An incremental encoder is used for measuring rotor position and speed of IPMSM (Fig.5.3). The control software is processed in a Hitachi microcontroller. The maximum frequency of the microcontroller is 48 KHz, thus the shortest possible sampling time used in experiments is

$$T_s = \frac{1}{f_c} = \frac{1}{48kHz} = 20.83 \ \mu s. \quad (5.1)$$

A PC is connected to the microcontroller, so that the control software is downloaded from the PC into the microcontroller.

5.2. Experiments on the indirect torque control of IPMSM via stator-current regulation

The indirect torque control of IPMSM via stator-current regulation in the rotor reference frame with the block-diagram shown in Fig. 4.1 is implemented. The corresponding software is uploaded in the microcontroller of the VSI supplying the double-layer IPMSM under study. As IPMSM mechanical load, the cage IM is vector-controlled with speed closed-loop by the software installed in the microcontroller attached to its supplying VSI.

The reference *dq* stator currents are obtained from Eqs.(4.6)-(4.8) for constant-torque operation region, and from Eqs.(4.9)-(4.12) in flux-weakening constant-power region.

The information regarding the speed of the IPMSM is received in a time interval equal with $32 \cdot T_s$. During experiments the value of the DC-link voltage of the inverter is set at U_{dc}=320 V.

Steady-state performance of the IPMSM under indirect torque control

For steady-state performance analysis of the double-layer IPMSM prototype under PWM-current-regulated torque control, the references for torque and speed are set at 30 Nm and 1000 rpm, respectively. Experimentally-obtained IPMSM torque and stator-phase current characteristics are given in Figs.5.4 and 5.5.

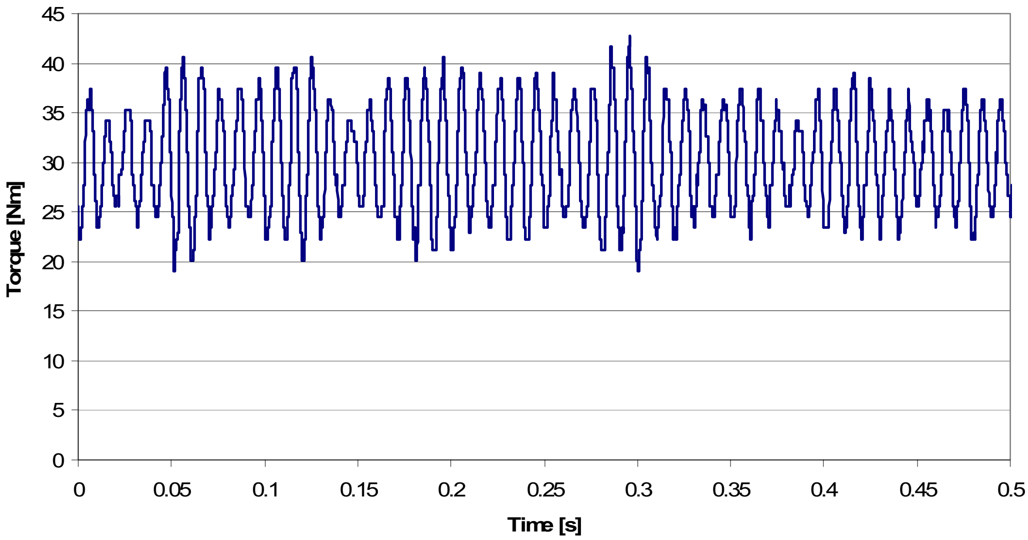

Fig.5.4. Steady-state torque characteristic of IPMSM under indirect torque control, for T_{eref}=30 Nm at 1000 rpm.

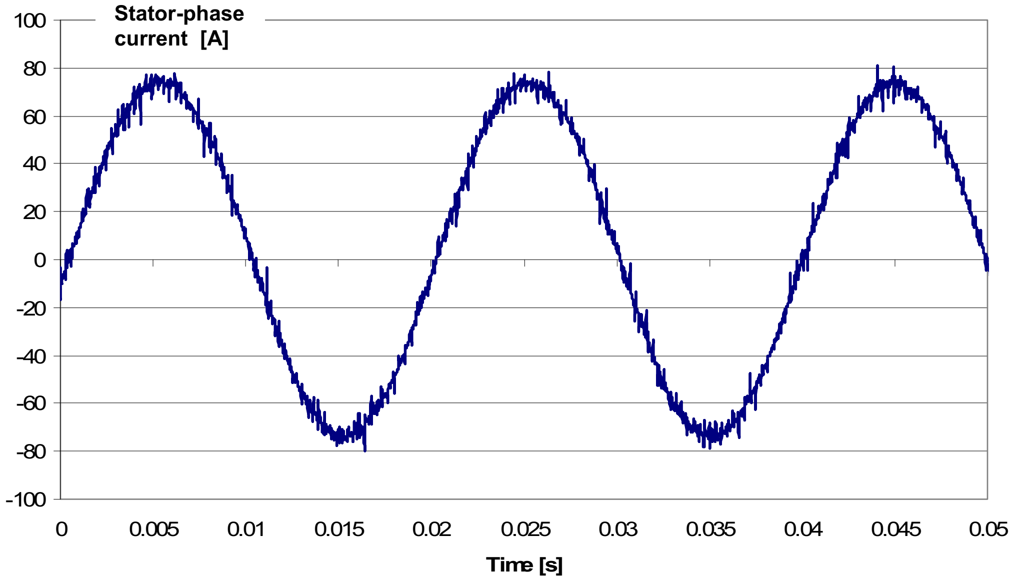

Fig.5.5. Steady-state phase-current characteristic of IPMSM under indirect torque control, for T_{eref}=30 Nm at 1000 rpm.

It can be seen that the IPMSM actual torque tracks its reference but with notable torque ripple, while the measured stator-phase current is quite sinusoidal.

Fig. 5.6 shows experimental results for the overall efficiency of the indirect torque-controlled IPMSM for different torque reference values in the constant-torque region from standstill up to the base speed. It can be observed that the IPMSM efficiency increases for higher torque and speed.

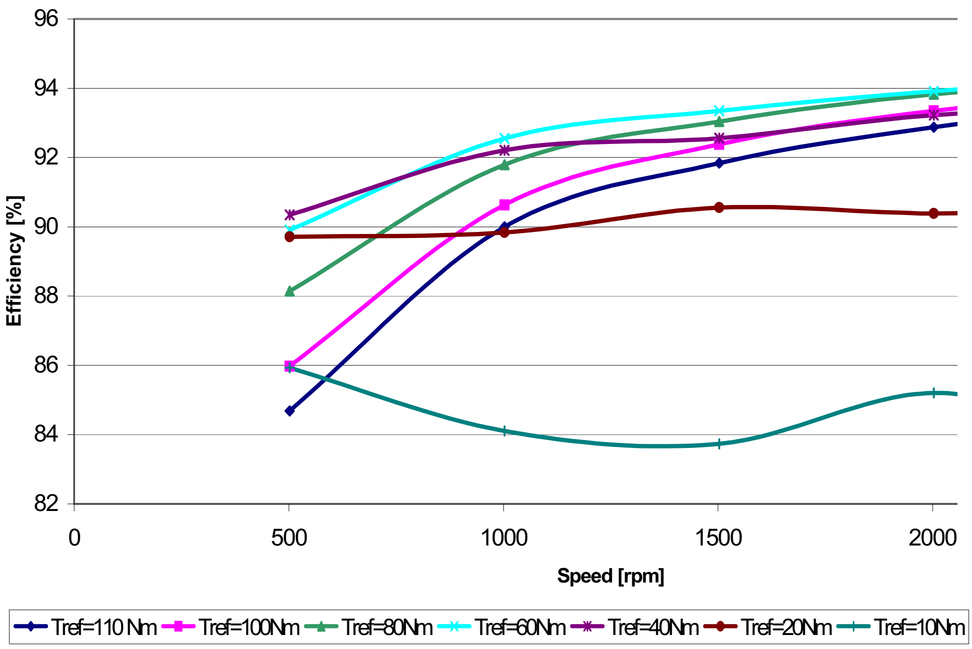

Fig.5.6. Steady-state efficiency of IPMSM under indirect torque control, for different reference torques and speeds, in constant-torque operating region.

Dynamic performance of the IPMSM under indirect torque control

The torque-step dynamic response of the IPMSM under indirect torque control is investigated. The speed was set at 1000 rpm, while the IM (mechanical load) is speed-controlled. In the first dynamic test, the IPMSM is driven from generator to motor by a reference torque step-change from -60 to 60 Nm, the experimental results being reported in Figs. 5.7 and 5.8.

The second dynamic test is performed by applying a reference torque step-change from 20 to 60 Nm to the IPMSM at the same speed of 1000 rpm. The experimental results are presented in Figs. 5.9 and 5.10.

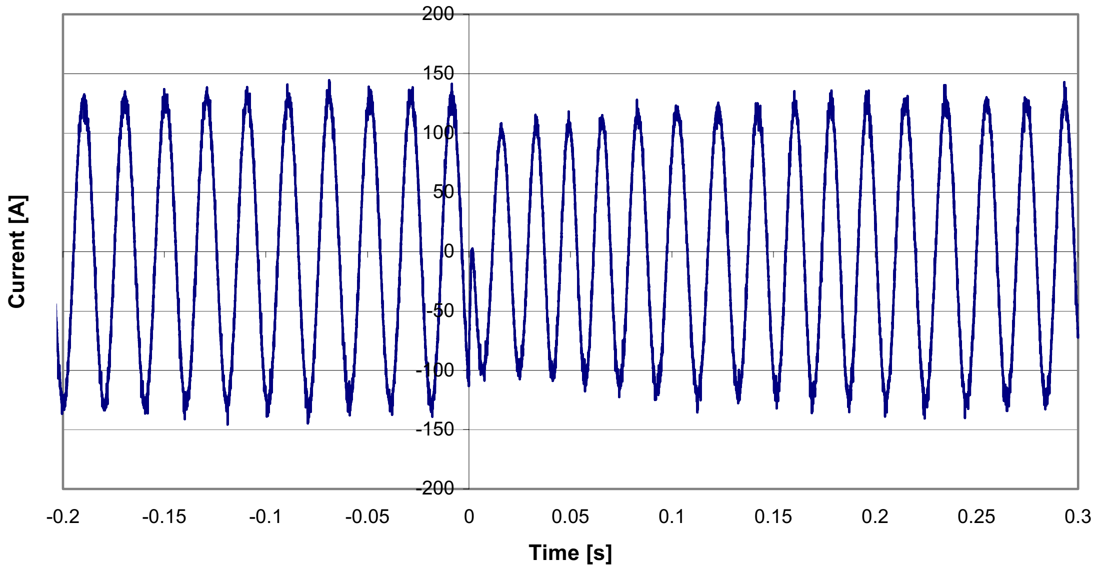

Fig.5.7. Stator-current dynamic response of the IPMSM under indirect torque control for a reference torque step-change from -60 to 60 Nm at 1000 rpm.

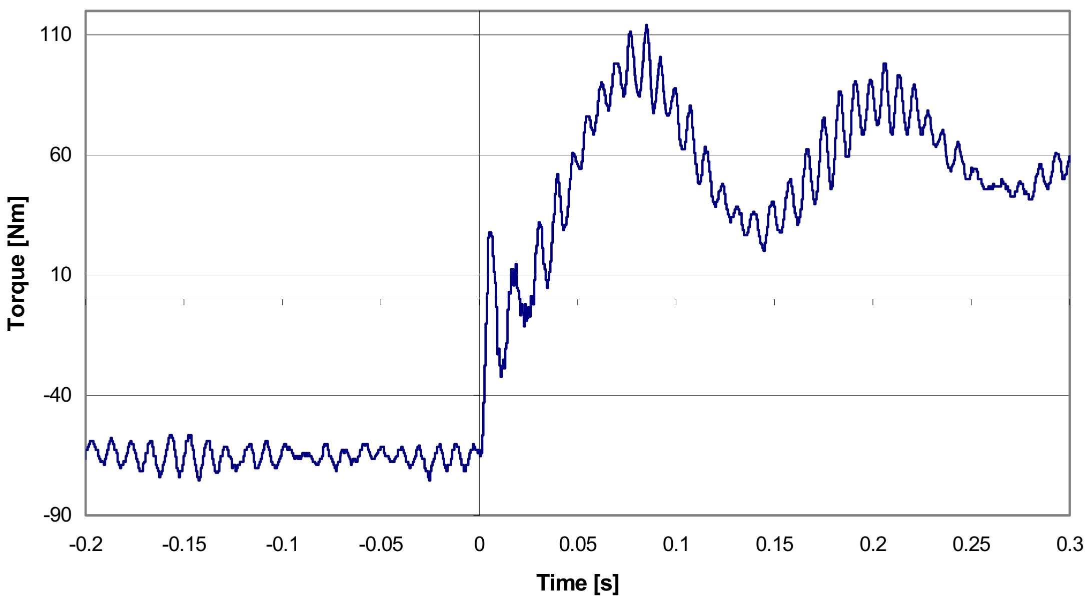

Fig.5.8. Dynamic torque response of the IPMSM under indirect torque control for a reference torque step-change from -60 to 60 Nm at 1000 rpm.

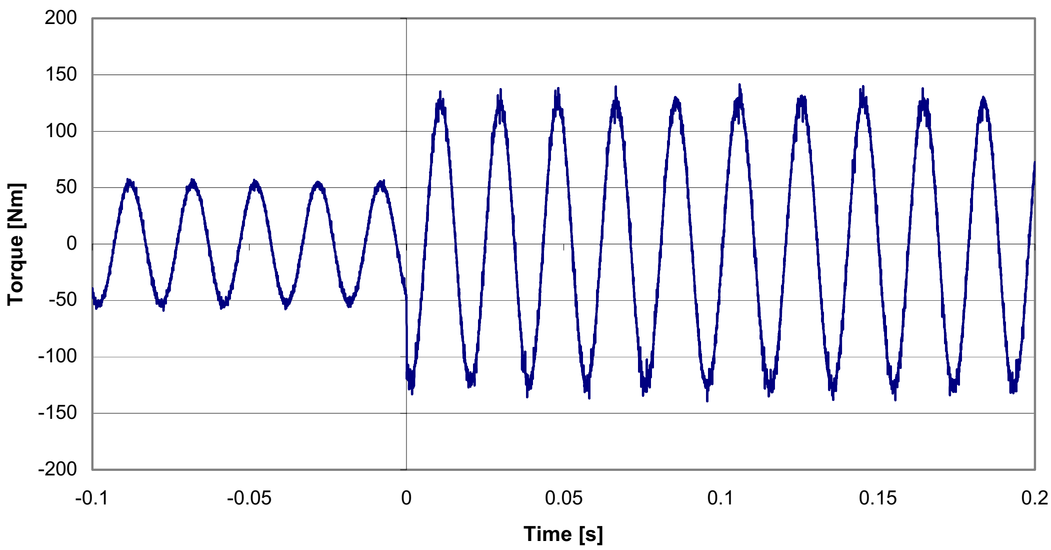

Fig.5.9. Stator-current dynamic response of the IPMSM under indirect torque control for a reference torque step-change from 20 to 60 Nm at 1000 rpm.

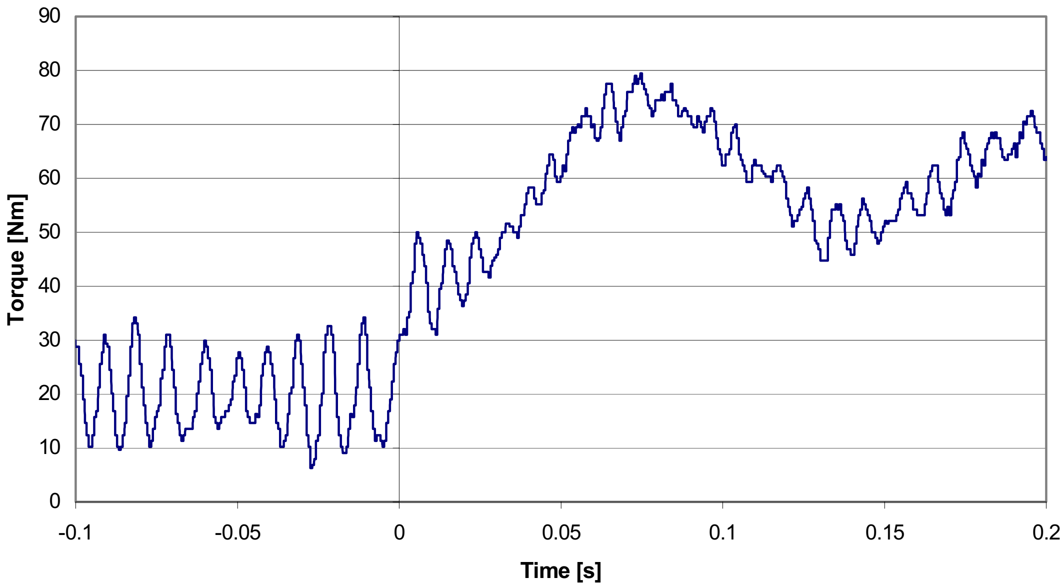

Fig.5.10. Dynamic torque response of the IPMSM under indirect torque control for a reference torque step-change from 20 to 60 Nm at 1000 rpm.

It can be seen from both dynamic tests, that the IPMSM stator current, as directly controlled quantity, yields a faster dynamic response than the electromagnetic torque. Hence, the torque reference value is reached only after 50 ms, and torque oscillations around the reference value may be observed even after 300 ms.

It is to be noted that for the IPMSM under indirect torque control, the torque reference is hardly changed from the PC in dynamic tests. Actually, it lasts one sampling-time period between the instant when the stator current starts to change and the moment when the new torque reference is detected for dynamic torque response.

5.3. Experiments on hysteresis-based direct torque and stator-flux control of IPMSM

The experiments are carried out with the IM (mechanical load) vector-controlled by speed closed-loop and the double-layer IPMSM prototype under direct torque and stator-flux control (DTFC). The software implemented in the microcontroller of the VSI feeding the IPMSM corresponds to the hysteresis-based DTFC scheme proposed in section 4.2 with the stator-flux estimation using the *dq* current model of Eqs.(4.39)-(4.41).

Steady-state performance of the IPMSM under DTFC in constant-torque operation range

DTFC of the IPMSM is performed in the constant-torque region, from standstill to the base speed, for maximum torque-to-stator current ratio operation. The function $|\underline{\Psi}_{srefI}|(T_{erefI})$ requested in the proposed hysteresis-based DTC scheme of IPMSM in the constant-torque operation range is calculated off-line using Eqs.(4.29) and (4.30) and stored in a look-up table.

For steady-state performance analysis of the double-layer IPMSM prototype under DTFC, the references for torque and speed are set at 30 Nm and 1000 rpm, respectively. Experimentally-obtained IPMSM torque, stator-phase current and stator-flux characteristics are given in Figs.5.11, 5.12 and 5.13, respectively.
As seen from these figures, the IPMSM actual electromagnetic torque follows well its reference, but torque ripple is significant. The stator-phase current is sinusoidal, although harmonics are visible in its shape to a greater extent as in the case of IPMSM with PWM current-regulated torque control. Moreover, to produce the same torque at the same speed, the stator current of IPMSM with DTFC is higher than that of indirect torque-controlled IPMSM. The circular locus of Fig.5.13 proves that the stator flux-linkage magnitude (of 0.08 Wb rated value) is well controlled within the hysteresis band.

The measured back-emf in one stator phase of the IPMSM under DTFC, at low speed, is shown in Fig.5.14; its quasi-sinusoidal shape is revealed.

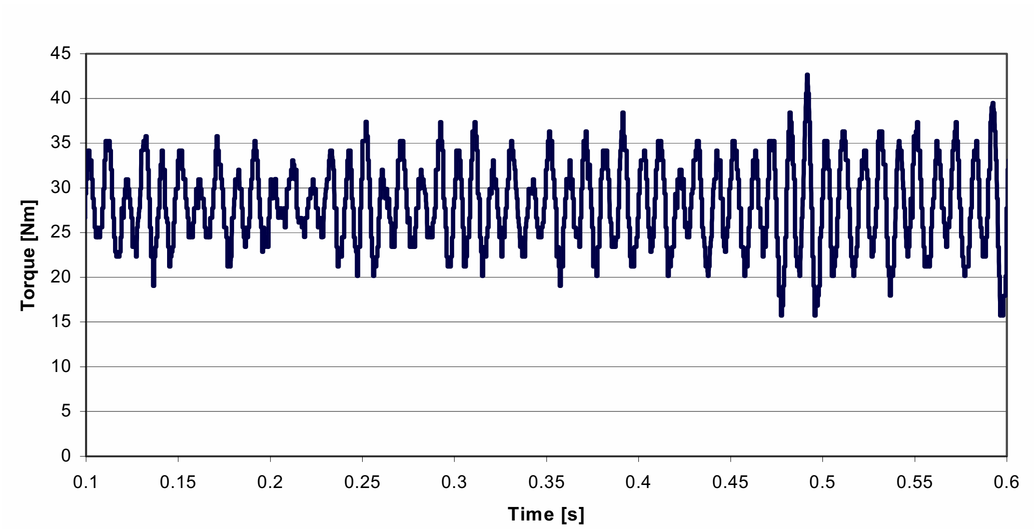

Fig.5.11. Steady-state torque characteristic of IPMSM under DTFC, for T_{eref}=30 Nm at 1000 rpm.

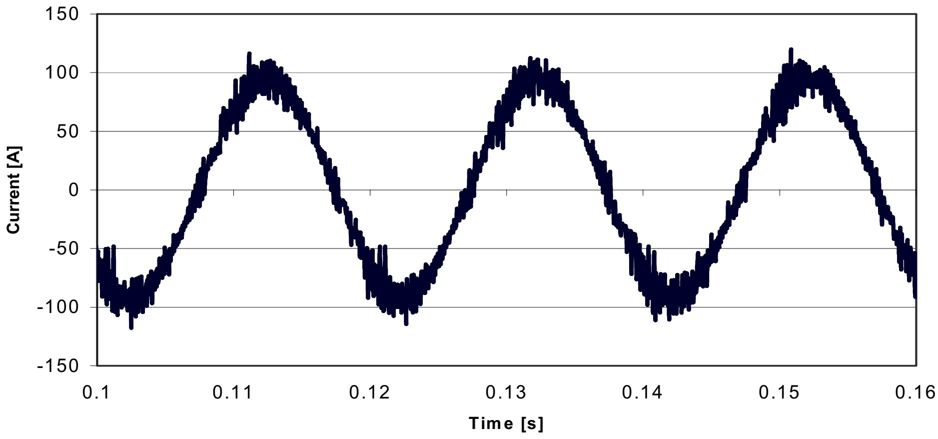

Fig.5.12. Steady-state phase-current characteristic of IPMSM under DTFC for T_{eref}=30 Nm at 1000 rpm.

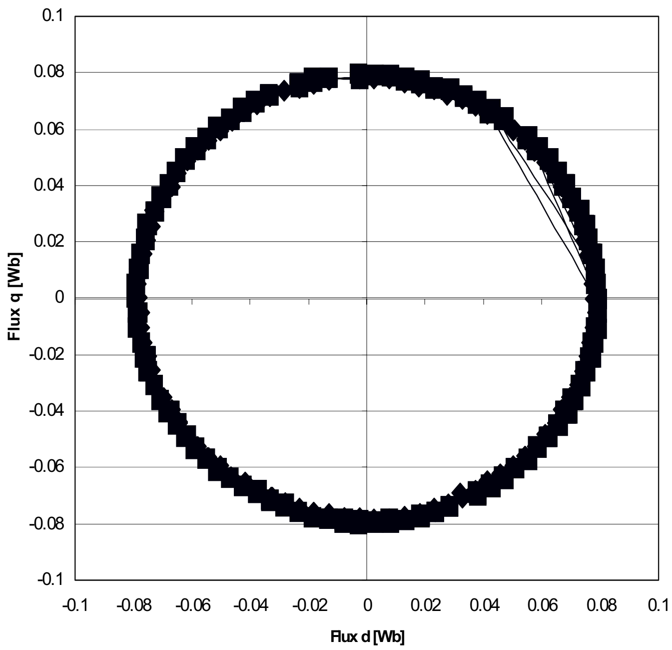

Fig.5.13. Steady-state locus of the stator flux-linkage vector of IPMSM under DTFC for T_{eref}=30 Nm at 1000 rpm.

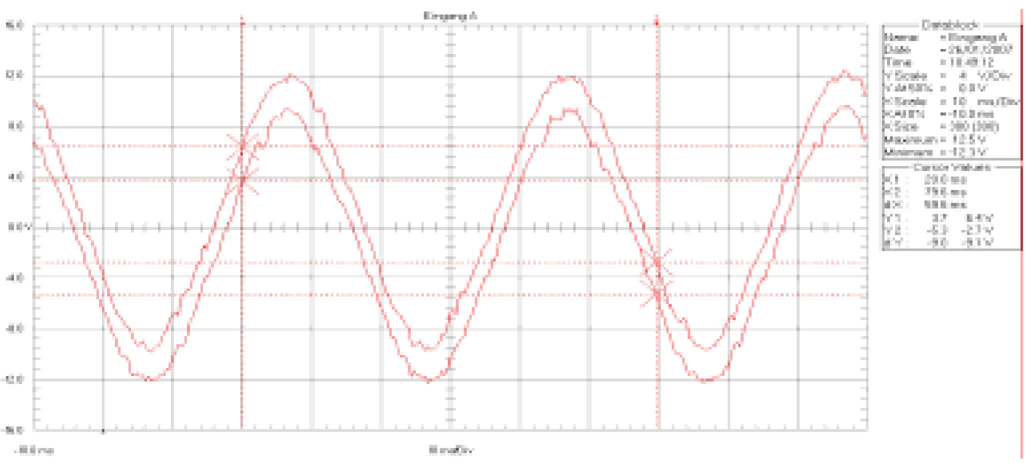

Fig.5.14. Measured stator-phase back-emf of IPMSM under DTFC at 500 rpm.

The output power vs. speed characteristic of the IPMSM under DTFC in constant-torque operation range is experimentally obtained for a reference torque of 100 Nm, and depicted in Fig.5.15.

The experimental result for the overall efficiency of IPMSM under DTFC in the constant-torque region is represented in Fig.5.16 for speeds up to the base speed and for different torque reference values. It is to be noted that, in this case, the efficiency is slightly lower as that of IPMSM under indirect torque control in constant-torque region of operation.

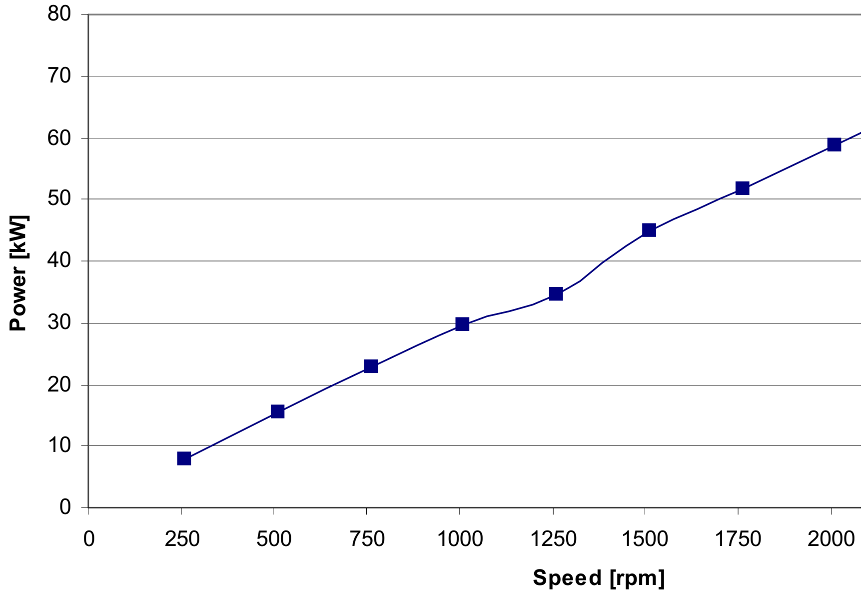

Fig.5.15. Steady-state output power of IPMSM under DTFC for T_{ref}=100 Nm and different speeds of the constant-torque range.

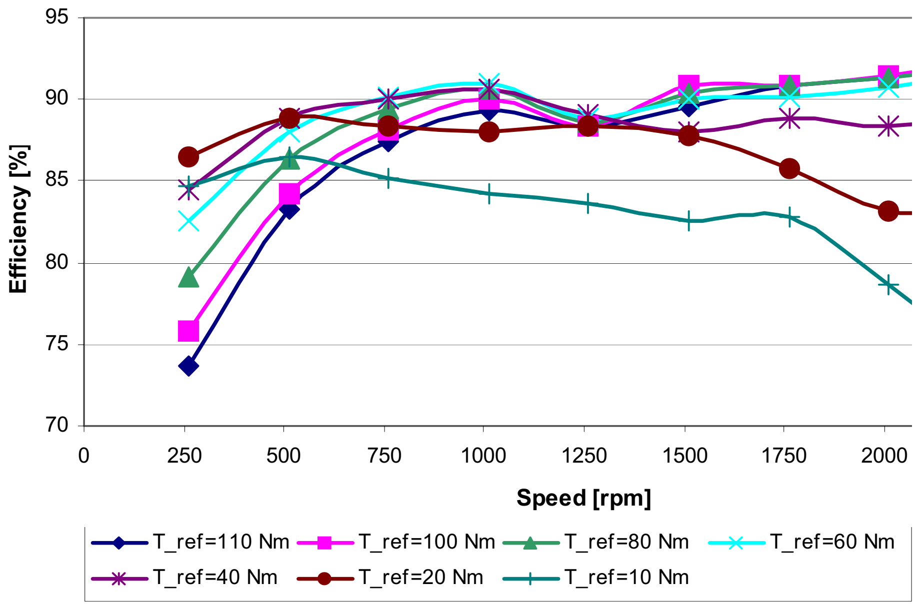

Fig.5.16. Steady-state efficiency of IPMSM under DTFC for different reference torques and speeds, in constant-torque operating region.

Dynamic performance of the IPMSM under DTFC in constant-torque operation range

The torque-step dynamic response of the IPMSM under DTFC is experimentally studied. The speed was set at 1000 rpm, while the IM (mechanical load) is speed-controlled. In the first dynamic test, the IPMSM is driven from generator to motor by a reference torque step-change from -60 to 60 Nm; the experimental results are presented in Figs. 5.17 and 5.18.

The second dynamic test is performed for a reference torque step-change from 20 to 60 Nm at the same speed of 1000 rpm. The experimental results are reported in Figs. 5.19 and 5.20.

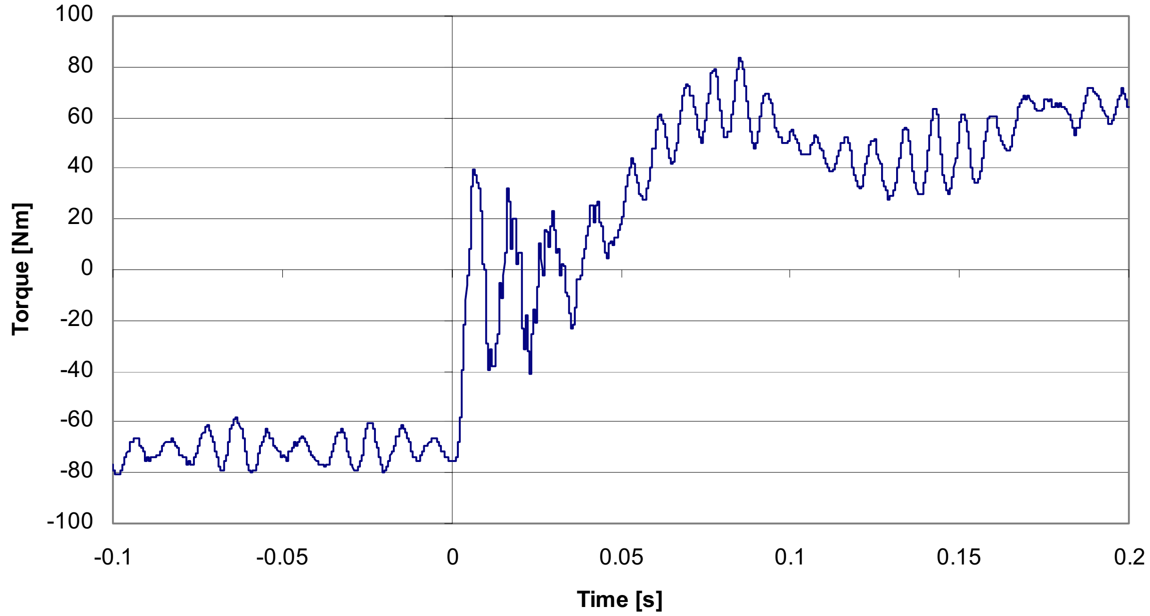

Fig.5.17. Dynamic torque response of the IPMSM under DTFC for a reference torque step-change from -60 to 60 Nm at 1000 rpm.

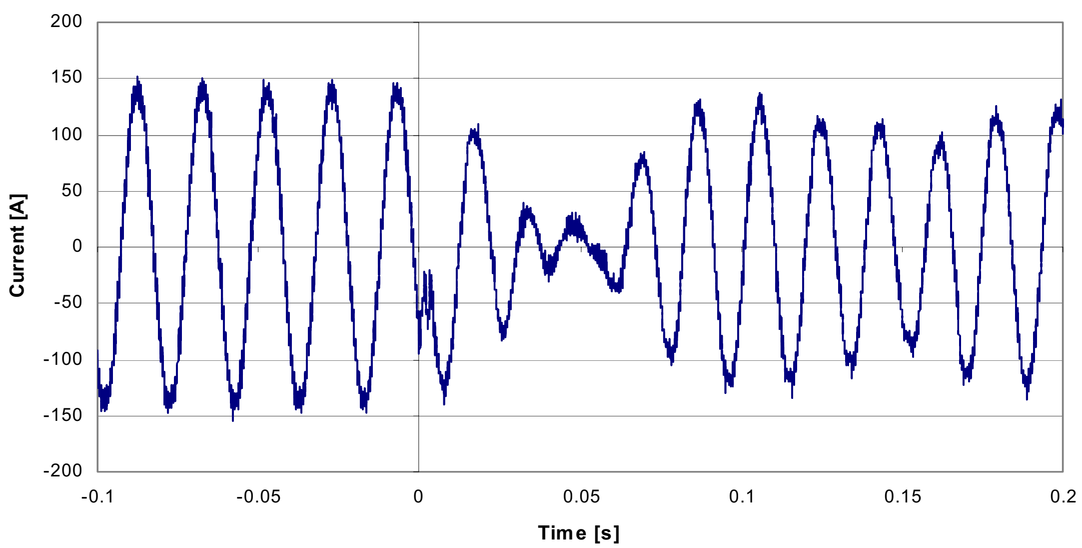

Fig.5.18. Stator-current dynamic response of the IPMSM under DTFC for a reference torque step-change from -60 to 60 Nm at 1000 rpm.

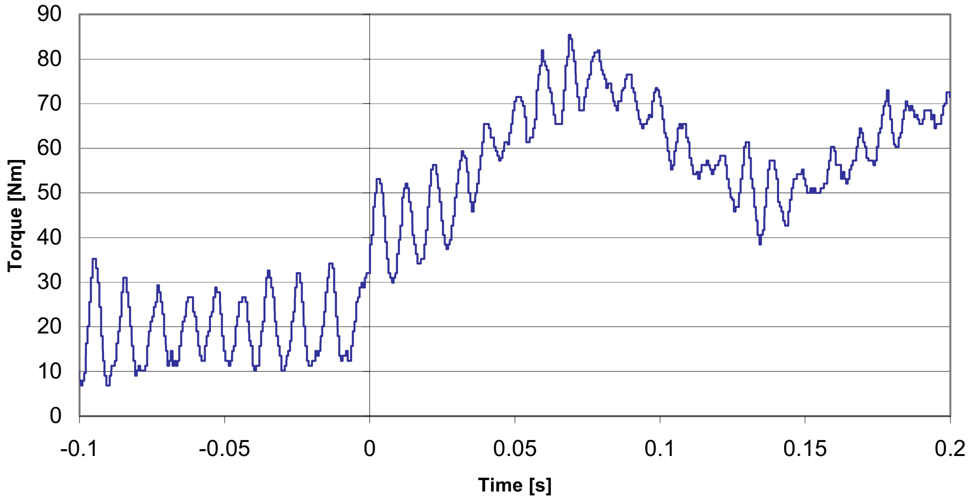

Fig.5.19. Dynamic torque response of the IPMSM under DTFC for a reference torque step-change from 20 to 60 Nm at 1000 rpm.

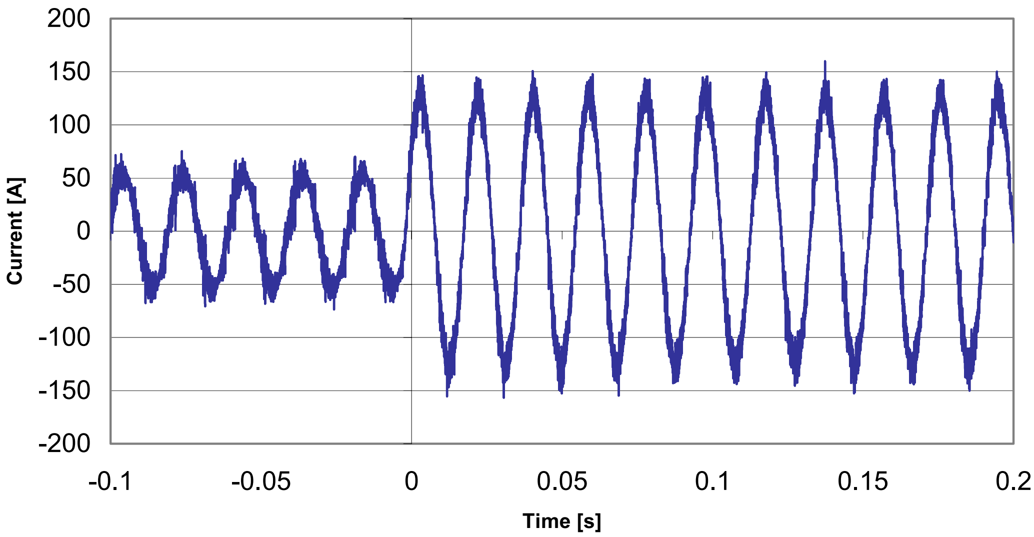

Fig.5.20. Stator-current dynamic response of the IPMSM under DTFC for a reference torque step-change from 20 to 60 Nm at 1000 rpm.

It can be seen from both dynamic tests, that the IPMSM torque response starts only after1 ms; hence, the torque reference is reached after 60 ms for the reference step-change from –60 to 60 Nm, and after 32 ms for the reference step-change from 20 to 60 Nm, respectively. Besides, there are significant torque oscillations before stabilization at the reference torque.

Steady-state performance of the IPMSM under DTFC in flux-weakening constant-power operation range

DTFC of the IPMSM is performed in the flux-weakening constant-power region with maximized torque at every speed above the base speed under both stator-current and voltage constraints. The required function $|\underline{\Psi}_{srefII}|(T_{erefII})$ in the proposed hysteresis-based DTC scheme of IPMSM for constant-power operation is calculated off-line using Eqs.(4.9)-(4.12) and (4.44) and stored in a look-up table.

For steady-state performance analysis of the double-layer IPMSM prototype under DTFC, the references for torque and speed are set at 30 Nm and 3000 rpm, respectively. Experimentally-obtained IPMSM torque, stator-phase current and stator-flux characteristics are given in Figs.5.21, 5.22 and 5.23, respectively.

As seen from these figures, the IPMSM actual electromagnetic torque tracks well its reference, while torque ripple has smaller amplitude as compared with IPMSM under DTFC in constant-torque region.

The stator-phase current is sinusoidal, although harmonics are altering its shape.

The nearly circular locus of Fig.5.23 points out that the stator flux-linkage magnitude is well controlled within the hysteresis band, although this one is larger than for IPMSM under DTFC in constant-torque region.

The measured back-emf in a stator phase of the IPMSM under DTFC in constant-power region, emphasizes a sinusoidal shape, as shown in Fig.5.24.

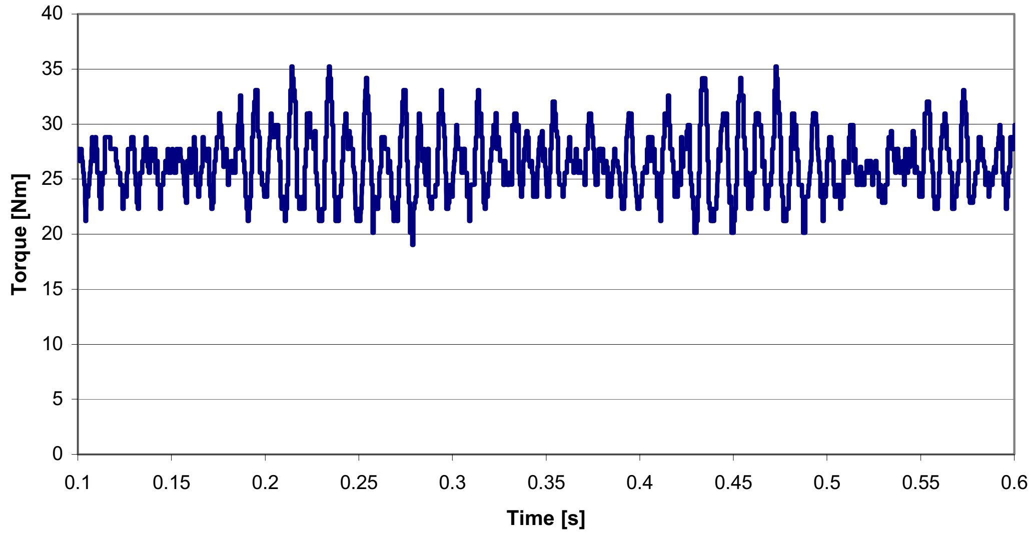

Fig.5.21. Steady-state torque characteristic of IPMSM under DTFC for T_{eref}=30 Nm at 3000 rpm.

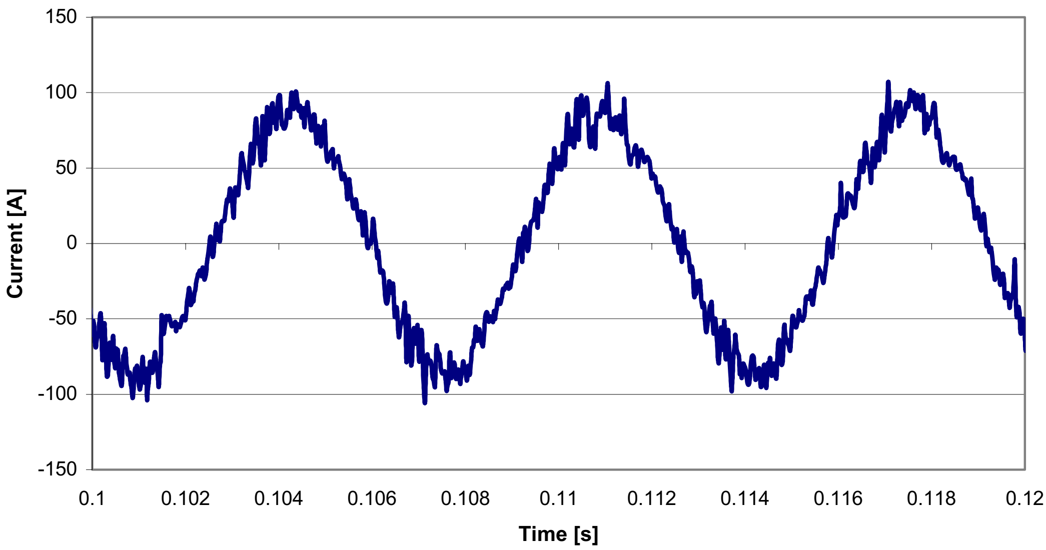

Fig.5.22. Steady-state phase-current characteristic of IPMSM under DTFC for T_{eref}=30 Nm at 3000 rpm.

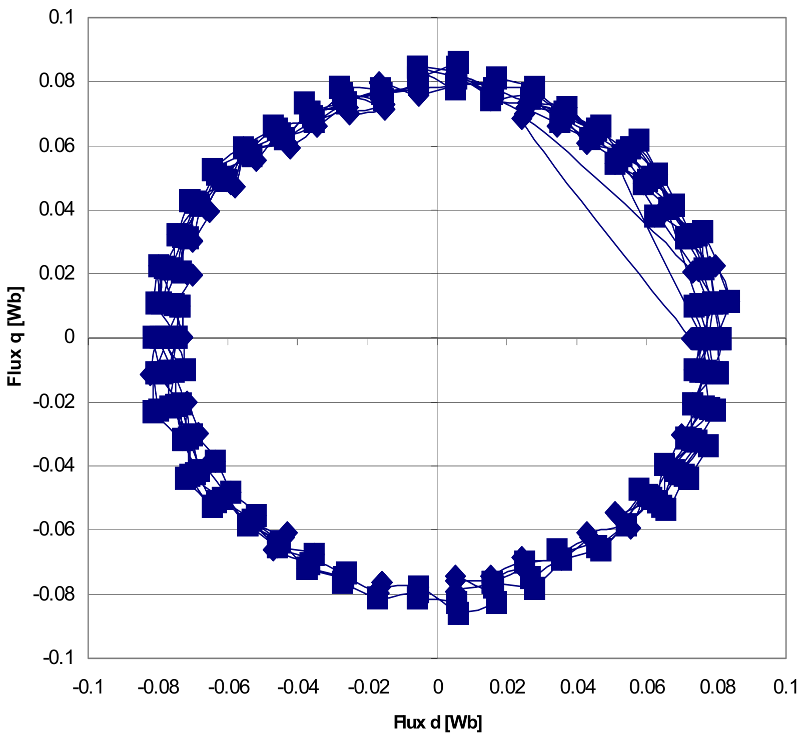

Fig.5.23. Steady-state locus of the stator flux-linkage vector of IPMSM under DTFC for T_{eref}=30 Nm at 3000 rpm.

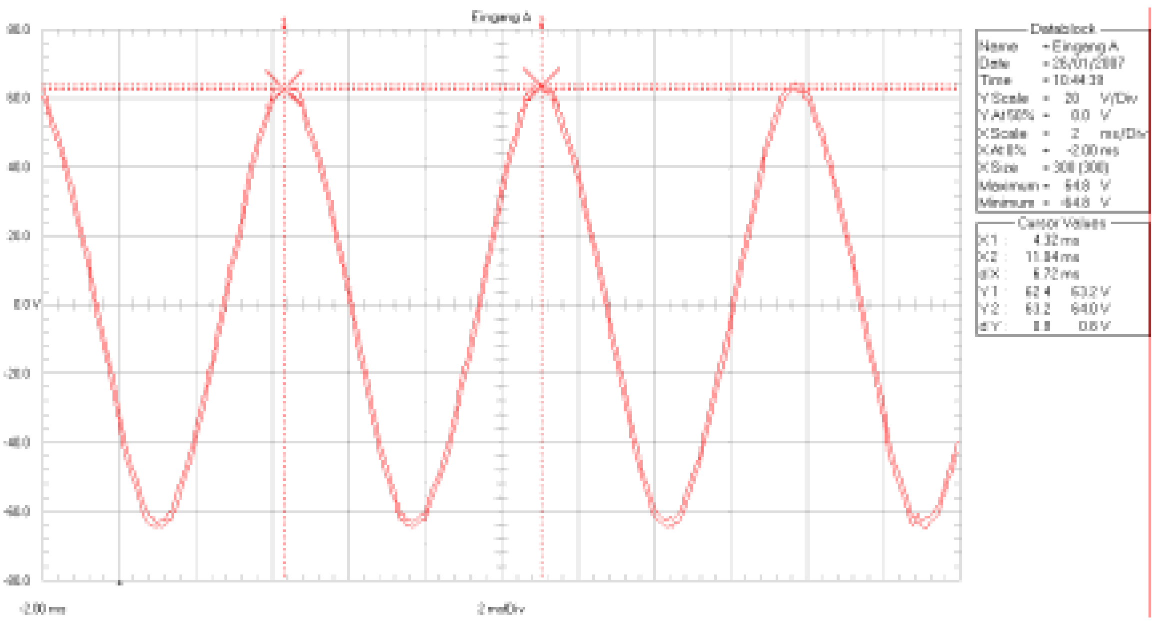

Fig.5.24. Measured stator-phase back-emf of IPMSM under DTFC at 3000 rpm.

The experimental efficiency of IPMSM under DTFC in the flux-weakening constant-power operation range is represented in Fig.5.25 for speeds above the base speed and for different torque reference values. It may be observed that the overall efficiency is superior to that of IPMSM under DTFC in constant-torque region.

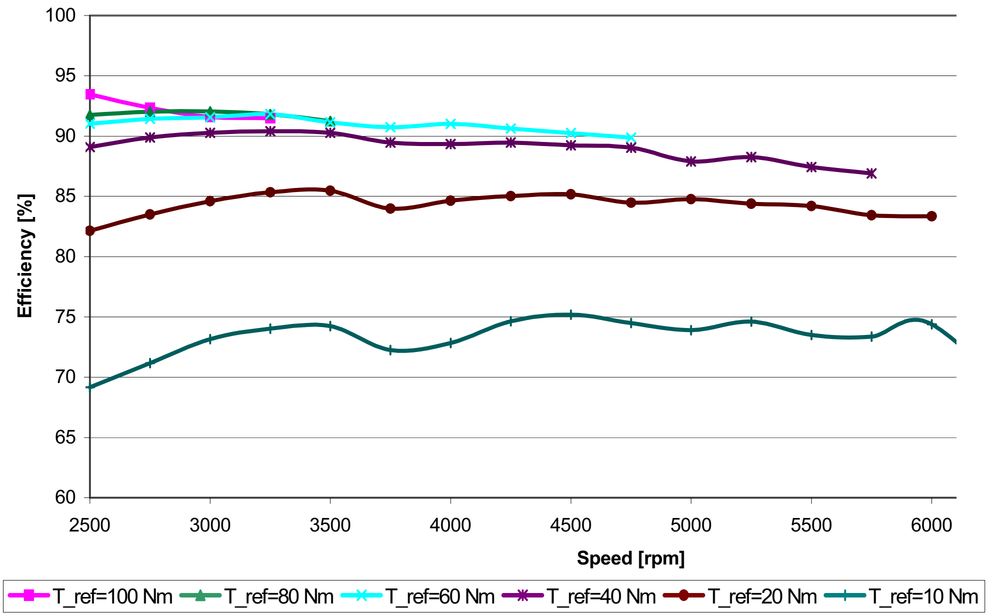

Fig.5.25. Steady-state efficiency of IPMSM under DTFC
for different reference torques and speeds, in constant-power region of operation.

Dynamic performance of the IPMSM under DTFC in flux-weakening constant-power operation range

The torque-step dynamic response of the IPMSM under DTFC in flux-weakening constant-power operation range is investigated. In the first dynamic test, a reference torque step-change from -40 to 40 Nm is applied to the IPMSM at 2500 rpm; the experimental results are reported in Figs. 5.26 and 5.27.

It can be seen, that the IPMSM torque response is very quick, the torque reference is reached in 4 ms, but there are significant torque oscillations before stabilization at the reference torque.

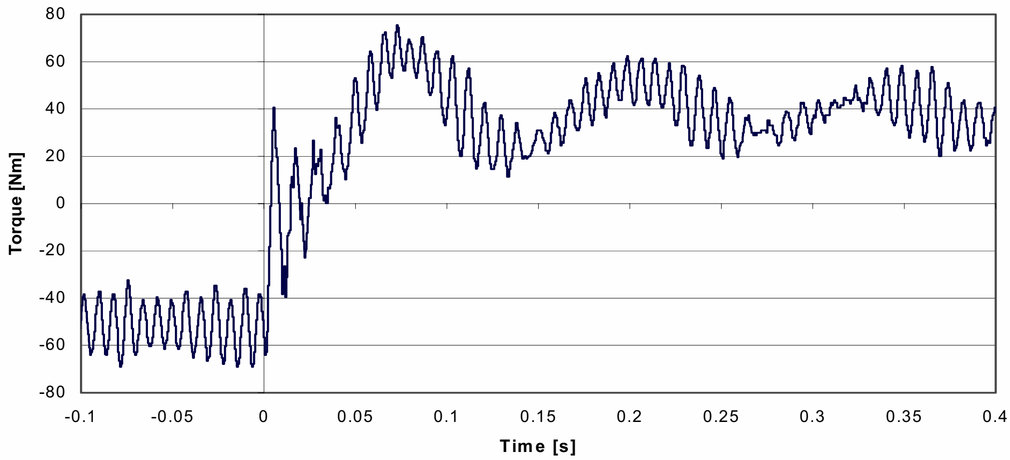

Fig.5.26. Dynamic torque response of the IPMSM under DTFC in flux-weakening constant-power operating region for a reference torque step-change from -40 to 40 Nm at 2500 rpm.

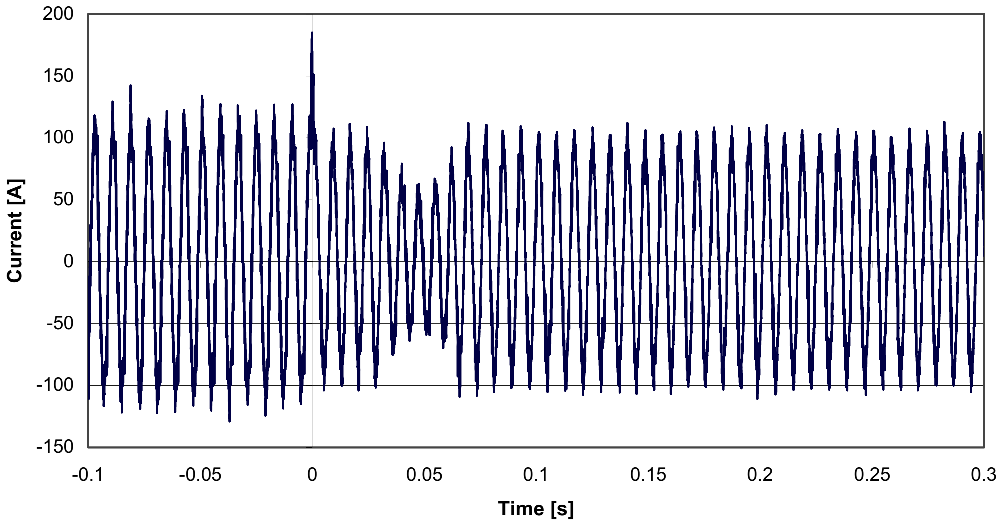

Fig.5.27. Stator-current dynamic response of the IPMSM under DTFC in flux-weakening constant-power operating region for a reference torque step-change from -40 to 40 Nm at 2500 rpm.

The second dynamic test of the IPMSM under DTFC is performed for a reference torque step-change from 20 to 40 Nm at the same speed of 2500 rpm. The experimental results are presented in Figs. 5.28 and 5.29.

In this case, the torque reference is reached after 32 ms, and considerable torque oscillations occur before stabilization at the reference torque.

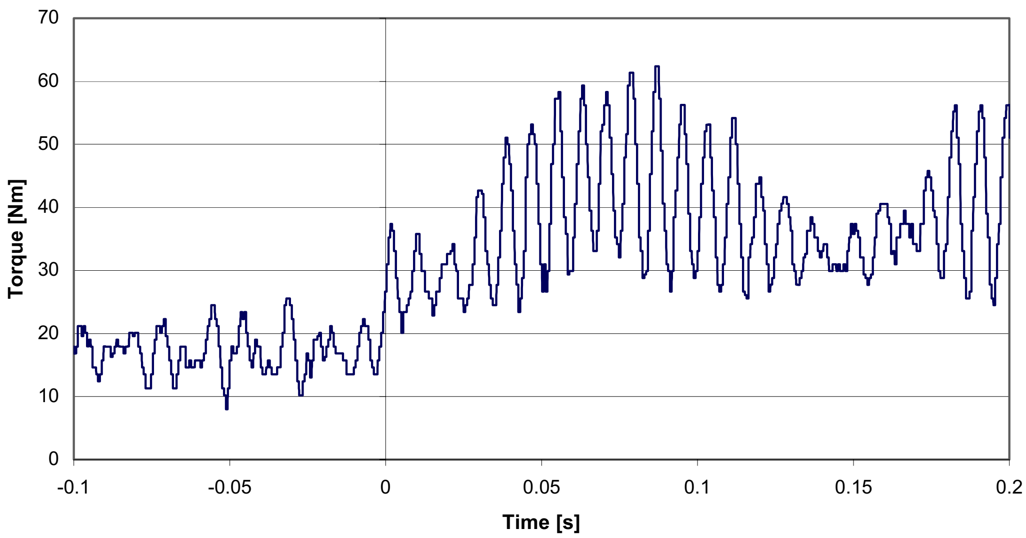

Fig.5.28. Dynamic torque response of the IPMSM under DTFC in flux-weakening constant-power operating region for a reference torque step-change from 20 to 40 Nm at 2500 rpm.

5.3. Conclusions

In the first part of this chapter, the experimental study on the indirect (via stator-current regulation) torque control of a double-layer IPMSM prototype in the constant-torque operation range is carried out.

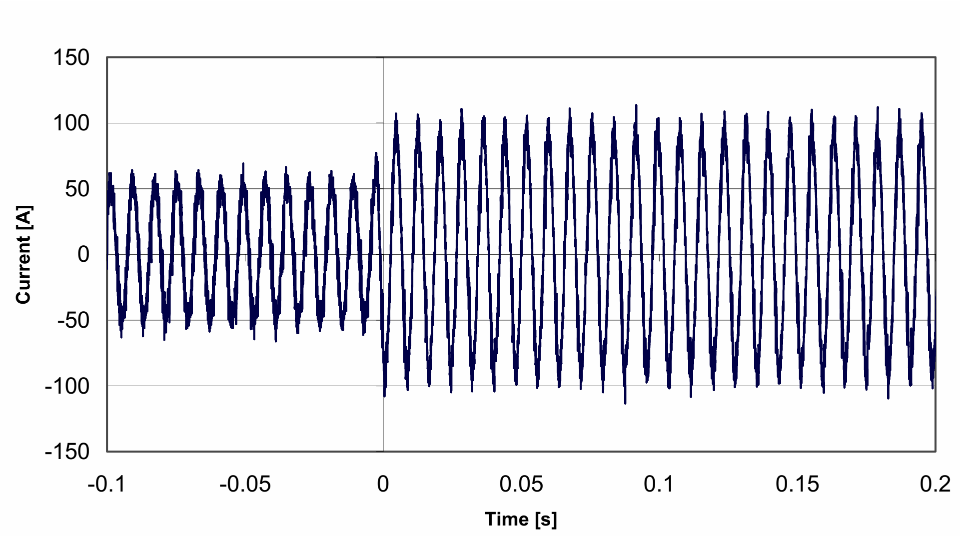

Fig.5.29. Stator-current dynamic response of the IPMSM under DTFC in flux-weakening constant-power operating region for a reference torque step-change from 20 to 40 Nm at 2500 rpm.

Experimental results show good steady-state efficiency and dynamic torque response of the IPMSM under implemented PWM current-regulated torque control scheme.

The second part of the chapter deals with experiments on IPMSM under DTFC. The same tests as for indirect torque control have been also performed for DTFC. Similar steady-state and dynamic performances are obtained for both IPMSM torque control strategies in constant-torque operation range.

Experiments for steady-state characteristics and dynamic torque response of the IPMSM under DTFC in flux-weakening constant-power region above the base speed are also provided and discussed.

Selected references

1. M.F. Rahman, L. Zhong, and K. W. Lim, A direct torque-controlled interior permanent-magnet synchronous motor drive incorporating field weakening. *IEEE Trans. Ind. Applicat.*, Vol. 34 (1998), No. 6, pp. 1246–1253.

2. J. Luukko, *Direct torque control of permanent-magnet synchronous machines - analysis and implementation*. Ph.D. Thesis, Lappeenranta University of Technology, Finland, 2000, ch.6.

3. J.-W. Park *et al.*, Improvement of control characteristics of interior permanent-magnet synchronous motor for electric vehicle. *IEEE Trans. Ind. Applicat.*, Vol. 37 (2001), No. 6, pp. 1754-1760.

4. Adina Muntean, M.M. Radulescu and A. Miraoui, Direct-torque controlled interior permanent-magnet synchronous motor for wide-speed-range applications. *Proc. 16th Int. Conf. Electr. Mach. – ICEM 2004*, Cracow, Poland, 2004, CD-ROM.

Chapter 6

GENERAL CONCLUSIONS

6.1. Major contributions of the thesis

The aim of this thesis is to analyse and control the developed torque of an IPMSM for LEV propulsion applications.

The main original contributions of the author within the research presented in this thesis are the following:

- synthesis of principal features of an EV propulsion system and with emphasis on specific IPMSM subclass designs for LEV propulsion applications;

- derivation of nonlinear dynamic models of the IPMSM as (i) a three-phase-variable circuit model accounting for parameter variations due to iron saturation, and as (ii) two-phase equivalent *dq* models for both constant-torque (with maximum torque-to-armature current ratio) and constant-power (with maximum-torque flux-weakening) operation modes, accounting for iron saturation and losses;

- equivalent magnetic circuit-based analysis of a double-layer IPMSM allowing the estimation of the rotor-PM sizes as well as the rated values of PM-rotor and armature-stator fluxes, back-emfs and unsaturated *dq* inductances;

- evaluation of average and pulsating components of the IPMSM electromagnetic torque by using the 2D FE field solution in the motor cross-section and integrating the Maxwell stress-tensor;

- practical methods, such as stator slot-opening reduction and PM-rotor skewing, applied to mitigate pulsating torque components for improving the electromagnetic torque quality;

- improved strategy for the indirect torque control of IPMSM via stator-current regulation in the rotor reference frame for both constant-torque and constant-power flux-weakening operation modes in EV propulsion applications;

- hysteresis-based DTFC strategy with a novel approach for the generation of the reference stator flux-linkage magnitude as a function of the reference electromagnetic torque, insuring extended torque-speed envelope of IPMSM with maximum-torque-per stator-current operation range below the base speed as well as constant-power flux-weakening with maximized torque above the base speed;

- design and construction of a double-layer IPMSM prototype suitable to EV propulsion applications with a dedicated implementation in a laboratory experimental set-up;

- extensive analysis of the dynamic torque response and overall efficiency of double-layer IPMSM prototype under indirect torque control and hysteresis-based DTFC proposed strategies for EV propulsion applications.

6.2. Suggestions for future research

As future recommendations of this research work, it is suggested

- to optimize the PM-layer and flux-barrier geometry and arrangement in the rotor structure of the IPMSM for improving the steady-state and dynamic torque performances in the constant-torque and flux-weakening regions of operation;

- to use an adaptive observer for more accurate stator-flux estimation in the proposed hysteresis DTFC of IPMSM based on the motor current model;

- to incorporate in the proposed IPMSM DTFC approach an optimization procedure to yield maximum efficiency over a wide speed range of the EV-drive motor operation;

- to extend the number of voltage vectors and sectors in the switching-table hysteresis-based DTFC of IPMSM in order to reduce the ripple in torque and stator flux-linkage magnitude;

- to use space-vector modulation instead of hysteresis controllers and switching table in the IPMSM DTFC scheme to further eliminate torque and stator-flux ripple and obtain fixed commutation frequency;

- to avoid the shaft-mounted encoder and its drawbacks of additional cost, reliability and susceptibility to noise and vibrations by using a sensorless technique of estimating the rotor position and speed of the IPMSM under DTFC.

List of symbols

Roman Letters

abc	three phase reference frame
A	the vehicle front area
A_{cav}	cavity area
A_{bik}	area of the k^{th} internal bridge
A_{bek}	area of the k^{th} external bridge
A_{fb}	area flux barriers
A_{gk}	area of the k^{th} air-gap element
A_{hqk}	area of the k^{th} rotor yoke
A_z	the magnetic vector potential
B_{av}	the average flux density
B_m	magnet inductance for a given working point
B_r	radial flux density component
B_d	tangential flux density component
$B_{\breve{u}max}$	maximum air-gap flux density
C	cost of the active materials
C_D	the aerodynamic resistance coefficient
dq	rotor reference frame
D_{si}	stator inner diameter
D_{so}	stator outer diameter
D_{ri}	rotor inner diameter
D_{ro}	rotor outer diameter
f	generic variable representing voltage, current, flux-linkage
f_r	the rolling resistance coefficient
g	air-gap width
$g`$	air-gap width corrected for stator slot openings (Carter factor)
G	the 'electrical gear ratio'
h_{bek}	width of the the k^{th} external bridge
h_{cavk}	height of k^{th} cavity element
h_{mk}	height of k^{th} magnet element
h_{qk}	height of the k^{th} q-flux path
h_{ss}	stator slot height
h_{st}	stator tooth height
h_{stg}	stator teeth height at the air-gap

h_{sy} stator yoke height

H_m magnetic field of PM for a given working point

i_{abc} current matrix

i_a, i_b, i_c instantaneous values of the stator-phase currents

i_ζ ζ-component of the current in the Ŭб stationary reference frame

i_η η-component of the current in the Ŭб stationary reference frame

i_d d component of the stator current in the dq rotor reference frame

i_q q component of the stator current in the dq rotor reference frame

i_{dref}, i_{qref} reference value of the stator current in dq rotor reference frame

i_{od}, i_{oq} magnetizing currents in dq rotor reference frame

i_{cd}, i_{cq} iron-loss equivalent currents in dq rotor reference frame

i_{ch} characteristic current

I_M maximum stator current

I_{ph} phase current

J motor inertia

J_z armature-winding current density

J_s the ampere per meter of airgap circumference

k_C Carter factor

k_f form factor

k_{we} winding factor

k_{sk} stacking factor

k_{ps} the ratio of stator slot width to stator slot pitch

l_f the (mean) flux-path length over one pole

L axial length of the motor

L_{abc} inductance matrix

L_{Co} length of the copper wire

L_d, L_q inductance of d-, and q- axis

L_{dt}, L_{qt} transitory saturated inductance of d-, respectively q-axis.

L_{ii} self inductance of the phase ($i=a, b, c$)

L_{ij} phase to phase mutual inductance ($i,j=a, b,c$)

m number of phases

M_v vehicle mass

mmf magneto motive force

n_{ml} number of magnet layers

n_d number of d-axis

n_{rd} number of rotor divisions per pole

N_{ss} number of stator slots

N_{steps} number of magnet block along the stack length.

N_{tph} number of turns per phase

N_{ts} number of turns per slot

p pole pair number

pf internal power factor

P_t traction power of EV

q number of slots per pole and phase

R resistance of the stator phase

R_c equivalent iron-loss resistance

R_{cavk} k^{th} cavity reluctance element

R_{gk} k^{th} air-gap section element reluctance

R_{mk} k^{th} magnet reluctance element

R_{ri} radius inner rotor

R_{ro} radius outer rotor

R_{si} radius inner stator

R_{so} radius outer stator

s number of skew steps

t_a acceleration time of the EV

T_{cog} cogging torque

T_e electromagnetic torque

T_{fr} friction torque

T_l load torque

u_{abc} voltage matrix

u_a, u_b, u_c instantaneous values of the stator-phase voltage

u_{aref}, u_{bref}, u_{cref} values of reference stator-phase voltages

$u_{Ŭ}$ Ŭ-component of the voltage in the Ŭб stationary reference frame

$u_{б}$ б-component of the voltage in the Ŭб stationary reference frame

u_d *d* component voltage in the *dq* rotor reference frame

u_q *q* component of the voltage in the *dq* rotor reference frame

U_{dc} d.c. link voltage

U_M maximum available voltage from the inverter

з reluctivity

$з_0$ reluctivity of air

V vehicle speed

V_b vehicle speed corresponding to the base speed of the electric motor

V_f final speed of acceleration period

V_r rotor volume

dV/dt	the vehicle acceleration
w_{bik}	width of the the k^{th} internal bridge
w_{Co}	mass of stator-armature winding
w_{mk}	width of k^{th} magnet
w_{mot}	weight of active materials in the motor
w_{ry}	weight of the rotor yoke
w_{so}	width of the stator slot opening
w_{st}	width of the stator teeth
w_{stg}	width of the stator teeth at the air-gap
w_{st}	weight of the stator teeths
w_{sy}	weight of the stator yoke

Greek Letters

Ŭб	stationary reference frame
ɔ	current angle
$ɔ_s$	electrical angle between two slots
ŭ	torque angle
ď	electrical angle
$ď_r$	mechanical rotor angle
N_{gs}	mmf in the air-gap produced only by the stator
σ_0	permeability of free space
σ_r	relative permeability
•	saliency ratio
Ɉ $_a$	the air mass density
$ψ_{Co}$	specific mass of the copper
$ψ_{Fe}$	specific mass of the lamination
$ψ_m$	specific mass of the permanent magnet
Ǘ	stator slot pitch
ɣ $_a$, ɣ $_b$, ɣ $_c$	instantaneous values of the stator flux-linkage
$q_{abc}{}^{i}$	current flux-linkage matrix
$q_{abc}{}^{m}$	PM flux-linkage matrix
ɣ $_{Ŭ}$	Ŭ-component of the stator flux linkage in the Ŭб stationary reference frame
ɣ $_{б}$	б-component of the stator flux linkage in the Ŭб stationary reference frame
‥ $_{PM}$	permanent magnet's flux linkage

‥$_d$ *d*- axis flux linkage

‥$_q$ *q*-axis flux linkage

λ_{bek} flux source of k^{th} external bridge

λ_{bik} flux source of k^{th} internal bridge

λ_{gm} air-gap flux produced by the magnet

λ_{gsk} air-gap flux of the k^{th} element

λ_{mk} flux source of k^{th} magnet

λ_{qsk} flux produced by the stator-armature in k^{th} segment

λ_{qrk} flux flowing through k^{th} rotor-yoke section

ϒ electrical angular speed

ϒ $_b$ electrical angular base speed

Acronyms

BLDC Brushless DC motor

DTFC Direct Torque and Stator-Flux Control

EV Electric Vehicle

FE Finite Element

IM Induction Motor

IPMSM Interior Permanent Magnet Synchronous Motor

EPS Electric Propulsion System

PM Permanent Magnet

PMSM Permanent Magnet Synchronous Motor

SPM Surface Permanent Magnet

SRM Switch Reluctance Motor